



数値解析および実験による流体力学的推力偏向機構に関する研究

メタデータ	言語: eng 出版者: 公開日: 2012-07-10 キーワード (Ja): キーワード (En): Fluidic Thrust Vectoring, CFD, secondary jet, Experimental studies 作成者: 李, 麗 メールアドレス: 所属:
URL	https://doi.org/10.15118/00005091

Numerical and Experimental Studies of Fluidic Thrust Vectoring Mechanisms

Doctoral Dissertation

December, 2011

Muroran Institute of Technology
Aerospace Engineering Division

Li Li

Contents

Contents	II
List of Tables.....	V
List of Figures	VI
Nomenclature.....	VIII
Abbreviations.....	X
Abstract.....	XI
Chapter 1 Introduction	1
1.1 Motivations and Objectives	1
1.2 Background and Development of TV Technologies	1
1.2.1 MTV Overview	2
1.2.2 Introduction to FTV	4
1.2.2.1 FTV Overview	4
1.2.2.2 Types of FTV	4
1.2.2.3 Comparison of FTV Methods	9
1.3 Thesis Outline	10
Reference	11
Chapter 2 Fundamental Theory of Numerical Studies.....	15
2.1 The Governing Equations	15
2.2 The Finite Volume Method and the Riemann Problem.....	16
2.3 Godunov's Method.....	17
2.4 Riemann Solvers	17
2.4.1 The Original HLL-Riemann Solver	18
2.4.2 The HLLC-Riemann Solver.....	19
2.4.3 Wave Speed Estimates	19
2.5 Weighted Average Flux	20
2.6 Splitting Schemes for Two-dimensional Systems.....	21
2.7 Parallel Computing Method.....	22
2.7.1 Parallelization Method of Two-Dimensional Code.....	22
Reference	24
Chapter 3 Preliminary Studies	25
3.1 Experimental Setup.....	25
3.1.1 Experimental Facilities	25
3.1.2 Instrumentations.....	27
3.1.3 Flow Visualization	28

3.1.4 FTV Parameters for Experiments.....	29
3.2 Numerical Simulations.....	29
3.2.1 Numerical Scheme	29
3.2.2 Initial and Boundary Conditions	30
3.2.3 Numerical Grids.....	30
3.2.4 Parameters in Computation	31
3.3 Results and Discussion	31
3.3.1 Nozzle Performance without Secondary Jet	31
3.3.2 Nozzle Performance with Secondary Jet.....	33
3.3.2.1 Flows Configurations around the Secondary Jet Exit	33
3.3.2.2 Static Pressures on Upper and Lower Nozzle Walls	38
3.3.2.3 Thrust Pitching Moment	40
3.4 Summary	42
References.....	43
Chapter 4 Studies with Improved Nozzle	44
4.1 Experimental Setup.....	44
4.1.1 New Nozzle and Test Equipment	44
4.1.2 Structure of Nozzle	45
4.1.3 Instrumentations.....	46
4.1.4 Flow Visualization	46
4.2 Numerical Simulations.....	47
4.3 Results and Discussion	47
4.3.1 Effect of Different Values of NPR	47
4.3.2 Effect of Different Values of SPR	49
4.3.3 Effect of Different Values of L_j	53
4.3.4 Effect of Different Values of β	55
4.4 Summary	56
References.....	57
Chapter 5 Evaluations of FTV Performance.....	58
5.1 The Method for Evaluating FTV Performance	58
5.1.1 Thrust Pitching Angle and Thrust Pitching Moment.....	58
5.1.2 Evaluation of Thrust Pitching Angle at the Different Location	58
5.1.3 Different Pivot Points Chosen to Evaluate the Thrust Pitching Moment.....	59
5.2 Effects of the FTV Parameters on FTV Performance	60
5.2.1 Effect of NPR.....	60
5.2.2 Effect of SPR	63

5.2.3 Effect of L_j	64
5.2.4 Effect of β	66
5.3 Summary.....	68
References.....	69
Chapter 6 Conclusions.....	70
6.1 Summary.....	70
6.2 Future Work	72
Acknowledgments	73
Appendices.....	74
A.1 Supersonic Flow and Shock Theory.....	74
A.1.1 One-Dimensional Gasdynamics	74
A.1.1.1 The Basic Equations.....	74
A.1.1.2 Isentropic Conditions	74
A.1.1.3 Stagnation Conditions	75
A.1.1.4 Critical Conditions	75
A.1.2 Flow in Converging-Diverging Nozzle.....	76
A.1.2.1 Flow in Nozzle of Vary Area.....	76
A.1.2.2 Nozzle Flow	77
A.2 Schlieren Methods.....	79
A.3 Instrument	81
References.....	82

List of Tables

Table 5.1 Thrust pitching angle at different mesh number.	59
Table 5.2 Thrust pitching moment at different SPR and L_j	63
Table 5.3 Thrust pitching angle at different SPR and L_j	64

List of Figures

Figure 1.1 Sea Harrier FA.2 ZA195 front (cold) vector thrust nozzle.....	2
Figure 1.2 The GE Axisymmetric Vectoring Exhaust Nozzle, used on the F-16 MATV.	3
Figure 1.3 Schematic of a co-flow fluidic thrust vectoring nozzle.	5
Figure 1.4 Schematic of a counter flow fluidic thrust vectoring nozzle.	6
Figure 1.5 Schematic of a throat shifting nozzle.....	7
Figure 1.6 Schematic of a throat shifting nozzle with recessed cavity.....	7
Figure 1.7 Schematic of a shock vectoring nozzle.....	8
Figure 1.8 Schematic of a combined vectoring nozzle.	9
Figure 2.1 Illustration of the initial data for the Riemann problem.	17
Figure 2.2 HLL Riemann solver.	18
Figure 2.3 HLLC Riemann solver.	19
Figure 2.4 Evaluation of the WAF flux for the linear advection equation.....	21
Figure 2.5 Discretisation of two-dimensional Cartesian domain into finite volumes.....	22
Figure 2.6 Computational domain distribution.	23
Figure 3.1 Schematic diagram of experimental setup.	25
Figure 3.2 Photograph of the Schlieren system and the pressure transducers.	26
Figure 3.3 Dimensions of two-dimension nozzle and vacuum cavity.	26
Figure 3.4 Dimensions of nozzle with secondary jet for $L_j = 10$ mm.....	27
Figure 3.5 Photograph of static pressure measurement.	28
Figure 3.6 Schematic of the Schlieren system.	28
Figure 3.7 Data collection interface.....	29
Figure 3.8 Flow domain and the boundary conditions.....	30
Figure 3.9 Numerical grids of the flow field.....	31
Figure 3.10 Schlieren pictures for different NPRs:.....	32
Figure 3.11 Static pressure at nozzle centerline without secondary jet.....	33
Figure 3.12 Interaction of secondary jet with primary flow at (a) $SPR = 1$ or (b) $SPR = 2$	34
Figure 3.13 Static pressure distribution in diverging nozzle section with $NPR = 8$	35
Figure 3.14 Mach number distribution in diverging nozzle section with $NPR = 8$	36
Figure 3.15 Schlieren images for $L_j = 5$ mm with $NPR = 8$ and (a) $SPR = 1$ or (b) $SPR = 2$	37
Figure 3.16 Schlieren images for $L_j = 10$ mm with $NPR = 8$ and (a) $SPR = 1$ or (b) $SPR = 2$	37
Figure 3.17 Mach number distribution and streamlines with $NPR = 8$ and $SPR = 1$	38
Figure 3.18 Wall pressure for $L_j = 5$ mm with $NPR = 8$ and (a) $SPR = 1$ or (b) $SPR = 2$	39
Figure 3.19 Wall pressure for $L_j = 10$ mm with $NPR = 8$ and (a) $SPR = 1$ or (b) $SPR = 2$	40

Figure 3.20 Thrust pitching moment.....	41
Figure 4.1 Sketch of experimental setup.....	44
Figure 4.2 Dimensions of nozzle without secondary jet injection at Mach number of 2.....	45
Figure 4.3 Dimensions of nozzle with secondary jet for $L_j = 10$ mm.....	45
Figure 4.4 Photograph of static pressure measurement.	46
Figure 4.5 Schematic of the Schlieren system.	46
Figure 4.6 Grids near the nozzle wall.	47
Figure 4.7 Schlieren images of different NPR and (a) NPR = 3 or (b) NPR = 9.....	48
Figure 4.8 Mach number distribution in the nozzle diverging part with NPR = 9.....	48
Figure 4.9 Velocity vector distribution near the secondary jet injection with NPR = 9	49
Figure 4.10 Density distribution in the nozzle diverging part with NPR=9	50
Figure 4.11 Schlieren images for $L_j = 10$ mm with NPR = 9 and (a) SPR = 1 or (b) SPR = 2 (c) SPR = 3.	51
Figure 4.12 Wall pressure for $L_j = 10$ mm with NPR = 9 and (a) SPR = 1 or (b) SPR = 2 or (c) SPR = 3.	53
Figure 4.13 Mach number distribution with NPR = 9 and SPR=1	54
Figure 4.14 Illustration of secondary angular injection.	55
Figure 4.15 Velocity distribution with NPR = 9 and SPR = 1	55
Figure 5.1 Thrust pitching moment with different values of NPR (pivot point is at throat).....	59
Figure 5.2 Thrust pitching moment with different NPR and (a) $L_j = 5$ mm or (b) $L_j = 10$ mm.	61
Figure 5.3 Thrust pitching angle with different NPR and (a) $L_j = 5$ mm or (b) $L_j = 10$ mm.....	62
Figure 5.4 Relation between pitching moment and pitching angle.....	63
Figure 5.5 Thrust pitching moment at different L_j with NPR = 9.	64
Figure 5.6 Thrust pitching angle at different L_j with NPR = 9.....	65
Figure 5.7 Relation between pitching moment and pitching angle.....	65
Figure 5.8 Thrust pitching moment at different β with NPR = 9.....	66
Figure 5.9 Thrust pitch angle at different β with NPR = 9.	67
Figure 5.10 Relation between pitching moment and pitching angle.....	67
Figure A.1 The flow through a tube segment.....	74
Figure A.2 Flow in nozzle of vary area.....	76
Figure A.3 Pressure distribution in the nozzle with different back pressure.....	77
Figure A.4 Schlieren system.	79

Nomenclature

U	Conserved variables
F	Fluxes in the x direction
G	Fluxes in the y direction
F^a	Inviscid fluxes in the x direction
G^a	Inviscid fluxes in the y direction
F^d	Viscosity and heat conduction fluxes term in the x direction
G^d	Viscosity and heat conduction fluxes term in the y direction
E	Total energy per unit volume
τ	Stress tensor
μ	Coefficient of viscosity
k	Thermal conductivity
T_0	Absolute temperature for the perfect gas
T_{ref}	Reference temperature
μ_{ref}	Reference viscosity
S	Sutherland temperature
Δt	Time step size
Δx	Computing cell length
c	Courant number
$f_{i-1/2}$	Upwind intercell numerical flux
$f_{i+1/2}$	Downwind intercell numerical flux
L_j	Distance between the secondary jet injection slot and the nozzle exit
β	Secondary angular injection
δ_p	Thrust pitching angle
F_A	x components of momentum
F_N	y components of momentum
M_p	Thrust pitching moment
l	Length from the working point to the pivot point
R	Ideal gas constant
γ	Heat capacity ratio
A	Nozzle section area
h_0	Stagnation enthalpy
u^*	Flow speed at sonic
a^*	Sound speed at sonic

p_0	Inlet pressure
p_{back}	Back pressure downstream the nozzle exit
p_c	First critical pressure, the choked nozzle but without shock
p_h	Second critical pressure , the normal shock at the nozzle exit
p_j	Third critical pressure, the nozzle isentropic design without shock
A^*	Nozzle throat area
M_1	Mach number upstream the shock wave at the exit
Δh	Displacement length of the source image
h_1	Uncovered length of the source image
f_2	Focal length of the second lens
ε	Angular displacement
L	Width of test section
β	Refractivity of the fluid
ρ_s	Reference density taken at standard conditions
$\left(\frac{d\rho}{dy}\right)_1$	Density gradient

Abbreviations

1D	One-Dimensional
2D	Two-Dimensional
CFD	Computational Fluid Dynamics
FTV	Fluidic Thrust Vectoring
HLL	Harten, Lax, and van Leer
HLLC	Harten, Lax, and van Leer Contact
IVP	Initial Value Problem
MPI	Message Passing Interface
MTV	Mechanical Thrust Vectoring
NPR	Nozzle Pressure Ratio
PDE	Partial Differential Equation
PVM	Parallel Virtual Machine
SPR	Secondary Pressure Ratio
SVC	Shock Vector Control
TS	Throat Shifting
TV	Thrust Vectoring
WAF	Weighted Average Flux

Abstract

The Fluidic thrust vectoring (FTV) is emerging as a significant technology for high-performance air vehicles. The technology can improve aircraft maneuverability by manipulating the nozzle flow to deflect from its axial direction. The objectives of this study are to investigate the effect of a secondary jet on the primary flow in a converging-diverging nozzle, to discuss the effect of FTV parameters, and to evaluate the FTV performance.

Numerical and experimental studies of FTV were carried out first with a preliminary nozzle, and then a series of investigations were carried out with an improved nozzle model. The experiments are performed with a nozzle pressure ratio (NPR) of 3–10, a secondary pressure ratio (SPR) of 1, 2 or 3, and two different secondary jet locations. Numerical simulations of the nozzle flow are done with solving the Navier-Stokes equations, and the input parameters are set to match the experimental conditions. Computations are performed with and without the secondary jet injection for different combinations of NPR, SPR, secondary jet location, and secondary angular injection.

In the preliminary experiments, the slot for the secondary jet injection was so large that the flow deflection by an oblique shock is concealed by complex wave interactions. As a result, it was found difficult to evaluate the FTV performance quantitatively. The improved experimental model with a relatively small secondary jet slot was constructed to study the details of the FTV mechanism and its performance.

The effects of FTV parameters, such as NPR, SPR, secondary jet location and inclination are discussed. The results show that the FTV parameters have direct effects on the FTV performance.

The thrust pitching moment and the thrust pitching angle are determined to evaluate the FTV performance. A method using force-moment balance and a common procedure for utilizing the ratio of the radial to the axial momentums of exhaust gas is discussed in detail.

The numerical results clearly indicate that the sign of the thrust pitching moment with the preliminary nozzle is opposite to that with the new nozzle. The pitching moment of the improved nozzle is positive as expected for oblique shock wave FTV.

The relation between the thrust pitching moment and the thrust pitching angle shows the positive inter-relation between them. Therefore, FTV performance can directly be evaluated with the thrust pitching moment.

Chapter 1 Introduction

1.1 Motivations and Objectives

The high-performance aircraft requires innovative technological advancements in the design of their power units [1]. Thrust vectoring (TV) is emerging as a key technology for current and future aircrafts. TV nozzles are effective under all flight conditions, and they can satisfy the design constraints of low cost, low noise, light weight, short take-off distance, and improve stealth characteristics [2].

Two known methods of TV are mechanical thrust vectoring (MTV) and fluidic thrust vectoring (FTV). MTV uses mechanical parts to deflect the exhaust gas direction. It not only adds weight and complexity to the aircraft power systems but also increases cost and maintenance requirements [3]. These factors have prompted researchers to investigate novel methods to achieve the same TV capabilities without incorporating moving parts. FTV is an alternative method that involves a directional alteration of the main exhaust gas flow by a secondary jet. Potentially, FTV nozzles provide effective flow deflection as well as eliminate the problems associated with additional mechanical parts.

The FTV technology has not yet been applied practically, which indicates that it is necessary to conduct further researches and developments on its effects and diversify its applications [4].

The objectives of the current study are to investigate the FTV effects and interaction of a secondary jet with the primary jet flow in a converging-diverging nozzle. The evaluation methods of the FTV performance with respect to the FTV parameters have also been investigated.

1.2 Background and Development of TV Technologies

The TV technology can improve aircrafts maneuverability by manipulating of the nozzle flow to deflect from its longitudinal axis. Further, this technology offers a host of advantages to modern air vehicles. TV nozzles can control aircrafts at post-stall high angles of attack, where conventional aerodynamic flights lose their power and effectiveness [5]. Since TV nozzles may efficiently produce pitch and/or yaw forces and moments with relatively less drag, vectoring nozzles could augment or possibly replace aerodynamic controls [6]. Flights using TV nozzles instead of traditional nozzles can reduce or eliminate the need for horizontal and vertical tails [7]. The advantages of achieving separation on the rear tail are reduced aircraft weight and better stealth than other conventional aircrafts. Moreover, the cost of the maintenance of the tail is also reduced. An aircraft integrated with TV nozzles can achieve desired results such as cruise, climb, and descent using less thrust. Because of the resulting lower thrust requirements, the aircraft can reduce fuel consumption and achieve longer

range flight. The TV technology can augment conventional actuators of aircraft for take-off and short take-off and landing capabilities [8]. Aircrafts with TV nozzles and turbofan engines can deflect the thrust up to as much as 90° , facilitating vertical take-off and landing. With small take-off and landing zones, aircrafts can operate in more compact environments such as on aircraft carriers and in damaged airfields [9]. TV is becoming popular in modern aircraft as it is becoming more useful and efficient.

There are two ways to achieve TV: MTV and FTV.

1.2.1 MTV Overview

MTV nozzles require operated hardware to direct the exhaust flow off the nozzle's longitudinal axis. Aircraft with a variable area nozzle can achieve optimal performance throughout the flight envelope. Figure 1.1 shows the front vector thrust nozzle used on the Sea Harrier FA.2 ZA 195, and the GE axisymmetric vectoring exhaust nozzle used on the F-16 MATV is shown in Fig. 1.2. Recent flights of the F-15 SMTD, F-18 HARV, and F-22 Raptor fighters successfully demonstrate the validity of the nozzles [10-15].



Figure 1.1 Sea Harrier FA.2 ZA195 front (cold) vector thrust nozzle.

http://en.wikipedia.org/wiki/Thrust_vectoring

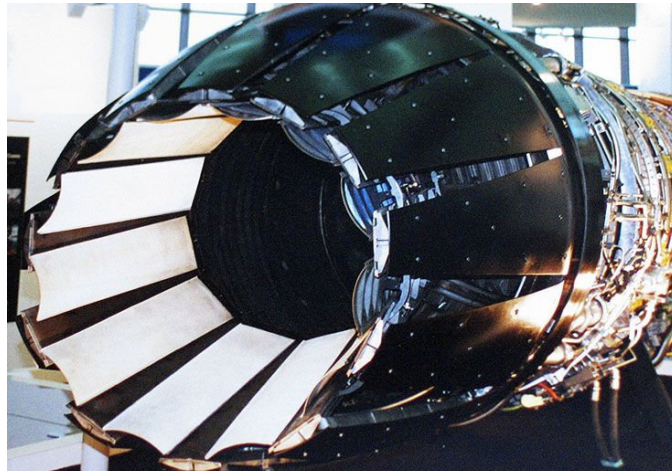


Figure 1.2 The GE Axisymmetric Vectoring Exhaust Nozzle, used on the F-16 MATV.

http://en.wikipedia.org/wiki/Thrust_vectoring

There are two typical approaches to achieve change in the thrust direction [16-18]. One approach involves the incorporation of jet vanes, paddles, moving hinged flaps, or spoilers into the jet exhaust region to alter the thrust direction physically. All these parts deflect the main flow at a certain angle to obtain the desired side thrust. Mechanical paddles have been used in the Nulka active missile decoy system [19]. The other approach involves the deflection of the divergent flaps of the nozzle or the inclusion of articulation in the nozzle to change the TV mechanically [20]. The Euro fighter Typhoon of EJ200 engine employs such a nozzle. The nozzle in F-15 ACTIVE airplane can help the design to reach 20° of off-axis turning, $80^\circ/s$ of vectoring rates, and 4000 lbf of vectoring forces [21]. The aircraft installed with mechanical multi-axis nozzles can be independent of the angle-of-attack, and the sideslip angle owing to the independent deflection of the divergent nozzle flaps [22, 23].

Although MTV technologies have been employed in modern aircrafts, there are some significant disadvantages. In order to avoid exceeding the force limits, the vector angles are controlled by the nozzle controller based on the flight condition and throttle setting. In order to achieve noteworthy thrust angle deflection, mechanical actuators and other hardware have to be incorporated, which add to the weight, complexity, and radar signature. The installation of the TV nozzles increased the weight by 2200 lb in the F-18 High Alpha Research Vehicle [24]. The complex nozzles in the F-15 and F-22 are roughly 50% heavier than other nozzles, which lack their advanced capabilities. The movable external flaps in the X-31 and F-18 HARV reduce the survivability of the aircraft [25]. In addition, the movable parts add to the aircraft maintenance requirements and are undoubtedly expensive in terms of drag penalty and time response. The necessity of high temperature resistant mechanical components also increases the overall system complexity and cost [26]. Further, it is difficult to integrate such a

complex nozzle system into the aircraft.

1.2.2 Introduction to FTV

The FTV technology is investigated to alternative MTV. FTV is to control the thrust direction of primary flow by using of a secondary jet. The advantage and disadvantage of FTV are discussed in detail, and the five types of the FTV are introduced and compared.

1.2.2.1 FTV Overview

Owing to the disadvantage of MTV, researchers want to investigate novel methods to achieve the same TV capabilities without using external moving parts. FTV, as an alternative method, has been investigated since 1990 [27, 28]. Instead of deflecting mechanical parts to create vectored thrust, an FTV nozzle uses a secondary air stream to manipulate the primary jet flow. The FTV nozzles theoretically provide flow deflection also eliminate the problems associated with mechanical parts [29].

FTV has numerous desirable advantages over MTV, such as lightweight, low noise, simplicity, low maintenance costs, etc. [30]. Fixed-geometry nozzles facilitate easier integration of the mechanical structure, which may result in fast response inherent to fluidic devices [31]. Moreover, FTV nozzles also have better stealth characteristics for simple wings and tail structures than their MTV counterparts. In addition, they also have the characteristics of post-stall performance, reduced take-off and landing distances and improved global combat agility. FTV nozzles can alter the direction of thrust by up to 18° and prevent the control surfaces from being directly exposed to the high temperature exhaust gases [32, 33]. Owing to its advantages over conventional means of TV, the FTV technology is a more suitable nozzle candidate for high-performance aircraft operations, such as rockets and hypersonic vehicles [34].

FTV, however, introduces some new problems. The main problem is that FTV also requires a source of secondary flow, and if the amount of secondary air drawn from the primary air supply is large, the thrust of the engine will be reduced. FTV has less capability with respect to directional change as compared to MTV. In addition, the FTV system must be implemented at the beginning of the design process unlike the mechanical system, which can be retrofitted to existing aircraft [35]. Regardless of these apparent imperfect consequences, FTV still seems to have appealing options that help improve the performance. The fact that FTV technology has not been employed in actual air vehicles, which indicates that it is still necessary to do more research and development on its effects and applications.

1.2.2.2 Types of FTV

There are five different FTV methods: co-flow FTV, counter-flow FTV, shock vector control FTV, throat shifting FTV, and combined vectoring methods. All these methods use secondary jet flows for TV. Each method has been investigated both experimentally and numerically with different levels of success.

1. Co-flow FTV

The co-flow FTV method relies on a phenomenon known as the Coanda effect, which was named after the Romanian researcher Henri-Marie Coanda in 1930 who put forward its effect on aircraft applications [36]. The schematic of a co-flow FTV nozzle is shown in Fig. 1.3.

The Coanda effect is the tendency of a flow of fluid or gas to adhere to the convex of a solid surface owing to the low pressure generated at the surface as the flow velocity over it increases [37, 38]. The secondary bleed air injects along the side of the primary jet nozzle outflow. The entrained air accelerates over the Coanda surface producing a local low-pressure region, which causes not only the injected flow but also the primary flow to shift off the normal thrust axis toward the wall.

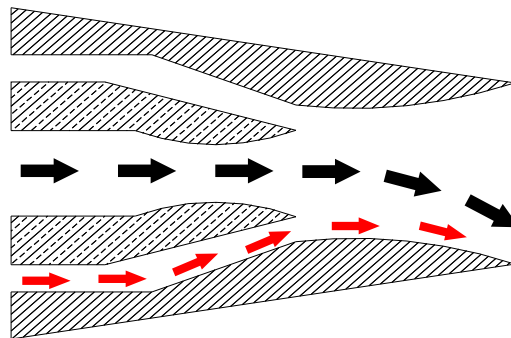


Figure 1.3 Schematic of a co-flow fluidic thrust vectoring nozzle.

Research on co-flow FTV has improved several critical design parameters of the nozzle geometry, which potentially reduces the pressure losses arising from the ducting of the secondary flow [39]. Some parameters such as the resultant thrust vector normal force generated on the Coanda surface and pitching moment have been investigated. A co-flow FTV system has been developed for use on low observable unmanned air vehicles operating in the subsonic flight regime. However, this TV nozzle generates relatively small thrust-vector angles and requires variable geometry for operation.

2. Counter-flow FTV

The counter-flow FTV method is also based on the Coanda effect and first reported by Strykowski and Krothapali. Counter flow induces vacuum in a slot shrouded by a suction collar near the primary

flow. Suction is applied to the plenum chamber in order to vector the primary flow according to the Coanda effect [40-42]. The asymmetric pressure loading generates a secondary reverse flowing stream at the wall of the suction collar and nozzle flow is directed towards the low-pressure region [43]. The schematic of the counter-flow FTV nozzle is shown in Fig. 1.4.

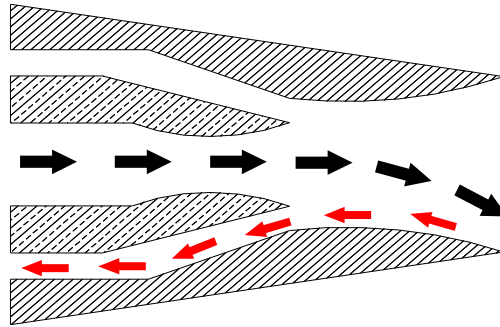


Figure 1.4 Schematic of a counter flow fluidic thrust vectoring nozzle.

The operating characteristics of the counter-flow nozzle for various conditions have been investigated. The pressure data are obtained at on-design conditions with supersonic exhaust flow, or at on-and-off-design conditions on a larger scale nozzle [44]. Further, the effects of suction collar geometry and suction slot height have also been investigated. Theoretically, counter-flow FTV generates large thrust-vector angles with a small secondary flow rate allowing more air to be directed through the engine. The counter flow can also cool the primary jet outflow via the interaction of the cool ambient air flow. Counter flow causes higher mixing flow, which can reduce jet noise and emissions from the nozzle. Counter flow does not suffer from bistability problems by implemented correctly [45].

Unfortunately, counter-flow TV has some limitations such as suction supply source, stability with a highly over-expanded nozzle, hysteresis effects, thrust loss, and airframe integration. Instability occurs at certain conditions and with various geometric configurations of the suction collar. The suction collars and slots have to be small-sized to have minimum impact on the aircraft weight and drag [46].

3. Throat shifting FTV

A throat shifting (TS) nozzle uses the injection of secondary flow at or near the throat to shift the sonic line and deflect the flow [47, 48]. The injection of a secondary mass flow at the throat changes the throat from a geometric minimum to an aerodynamic minimum and the asymmetric injection skews the sonic plane, which increases vectoring performance. The schematic of TS nozzle is shown in Fig. 1.5.

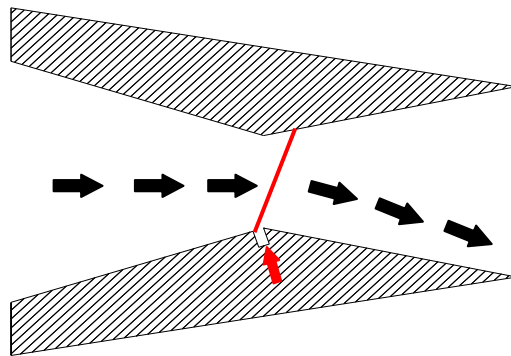


Figure 1.5 Schematic of a throat shifting nozzle.

A combination of the TS method with variable recessed cavities has also been investigated. Variable recessed cavities enable TV through the establishment of vortices in the cavities. The dual throat nozzle (DTN) achieves higher TV efficiencies by maximizing the pressure differentials of the separated and attaching flows in a recessed cavity; this has been researched at the NASA Langley Research Center (LaRC) [49]. A schematic of TS nozzle with recessed cavity is shown in Fig. 1.6.

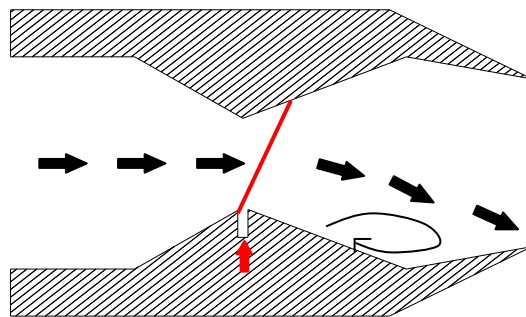


Figure 1.6 Schematic of a throat shifting nozzle with recessed cavity.

Subsonic shifting of the sonic plane causes lower loss of pressure and velocity of the primary flow by slowing the vectored flow as it travels over the sonic line. Fluidic sonic-plane skewing typically generates higher thrust ratios in the range of 0.94 to 0.98 and vectors efficiencies up to 2.15°/% injection [50]. The TS method is one of the most promising forms of FTV because of high thrust efficiency of up to 3°/% injection, which is achieved using an aft deck configuration at certain conditions [51].

Although the TS technology is currently improving, thrust vector technology has smaller angles compared to the shock vector control FTV method. Moreover, decoupling the simultaneous vectoring and jet area control is a challenge.

4. Shock vector control FTV

Shock vector control (SVC) uses a secondary air injection downstream of the throat in the diverging section of the nozzle [52]. The injected flow behaves like a compression pressure ramp in the supersonic primary flow, which induces an oblique shock wave at some angle. The primary flow interacts with the oblique shock wave and turns away from the longitudinal axis of the aircraft, which alters the direction of the force produced. The schematic of a shock vectoring nozzle is shown in Fig. 1.7.

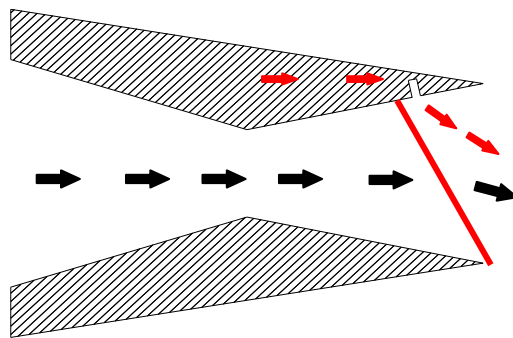


Figure 1.7 Schematic of a shock vectoring nozzle.

This approach achieves TV without any variation in the primary nozzle throat area and is effective in vectoring the nozzle stream. A nozzle with SVC technology is most effective at off-design flight conditions. Larger vector angles and more effective nozzle pressure ratios can be achieved. However, the fluidic SVC method achieves substantial thrust-vector angles at the expense of thrust ratio. In general, TV efficiencies up to 3.3%/ injection and thrust ratios in the range of 0.86 to 0.94 are typical. The oblique shock also causes a loss when the shock impinges on the opposite nozzle flap [53].

5. Combined vectoring methods

Some attempts for FTV have been made using a combination of techniques in order to obtain the greatest performance. It is possible to accentuate and complement one method by incorporating another method. Experimental and computational studies on a combination of fluidic TS and SVC for gas turbine engines have been undertaken [54]. The asymmetric secondary injection slots are located at the throat and nozzle flap on both the opposite interior sides of the nozzle. The asymmetric injection at the throat skews the sonic plane, which turns the flow subsonically, and the injection ports on the nozzle flap are used to deflect the primary flow further. However, it is difficult to control the distribution of the injected flow between the throat and flap simultaneously and complete the decoupling of the vectoring and jet area control [55]. The schematic of a combined vectoring nozzle is

shown in Fig. 1.8.

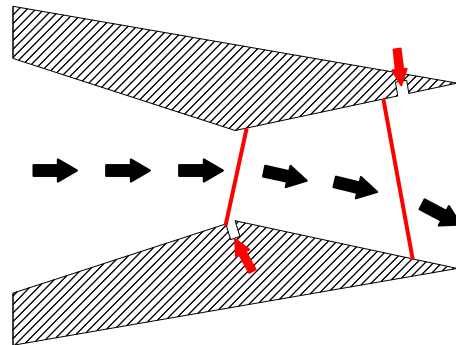


Figure 1.8 Schematic of a combined vectoring nozzle.

1.2.2.3 Comparison of FTV Methods

It is worthwhile to discuss the advantages and disadvantages of each different method to evaluate the most appropriate method for practical applications.

Although co-flow and counter-flow methods are considered the most suitable for practical use, the methods based on the Coanda effect cause instability in certain ranges of FTV. It is difficult to incorporate into the surrounding structure with the physical complexity of nozzles. Hysteresis effect and the attendant losses also occur when the primary jet outflow attaches to the nozzle collar. Moreover, an adequate supply of suction, which may add both complexity and weight to the system, is also a significant problem.

In comparison, the shock vector control and throat shifting methods are more reliable, for they provide more efficient. The TS method has high thrust efficiency and a relatively simple structure. However, the small vectoring angle makes it limit to adequate maneuver adjustments [55].

The SVC method also has a simple geometry and can achieve large deflection angle; however, this comes at the cost of the thrust ratio. The shock impingement problem is also one of the difficulties.

The inefficiency and drawbacks of the combined methods have not been widely investigated even though they are expected to achieve remarkable results [55].

Based on what has been described above, there are still many technical issues that must be addressed before the FTV mechanisms are practically used. Essentially, it is worthwhile to study the FTV mechanisms. Among the five FTV methods introduced above, both numerical and experimental studies have been carried out specifically on the SVC method. One of the problems while performing the present study was the method of determining the deflection angle of the exhaust gases from the axial direction.

We have introduced a method using force-moment balance to evaluate the FTV effect, and a

common procedure for utilizing the ratio of the radial to the axial momentums of exhaust gas. The relation between the two methods is discussed in the thesis.

1.3 Thesis Outline

The FTV effects and interaction of a secondary jet with the primary flow in a converging-diverging nozzle are investigated. The structure of the thesis is as follows.

The introduction and the background of the thesis have been presented in Chapter 1 (this chapter).

Chapter 2 presents the fundamental theories of numerical studies. Based on the computational fluid dynamics (CFD) method, the governing equations, the Godunov's method, the Riemann solvers, and the parallel computing method are introduced.

The experimental and numerical studies of a preliminary nozzle are described in Chapter 3. The FTV mechanism with respect to the unbalanced pressure distributions on the upper and the lower nozzle surfaces has been introduced and discussed in this chapter. Some technical problems with the test nozzle became obvious during the experiments.

The studies using the new nozzle model have been carried out, and the results are discussed in Chapter 4. The FTV mechanism with respect to the oblique shock has been introduced and discussed in this chapter. Interactions of the secondary jet with the primary nozzle flow under different conditions are also discussed.

The results obtained in Chapters 3 and 4 are discussed in Chapter 5. The thrust pitching moment and the thrust pitching angle are chosen to evaluate the FTV performance. The FTV parameters, such as NPR, SPR, secondary jet location and inclination are discussed. The relation between thrust pitching moment and exhaust gas deflection angle is also investigated in this chapter.

A summary and proposed future works based on the study are presented in Chapter 6.

Reference

- [1] J.Y. Lim, Numerical Investigation of Throat Shifting Method for Fluidic Thrust Vectoring - Initial Thesis Report, Initial Thesis Report, 2009.
- [2] Rickey J. Shyne, A Survey of Challenges in Aerodynamic Exhaust Nozzle Technology for Aerospace Propulsion Applications, NASA/TM-2002-211977.
- [3] Scott C. Asbury, Francis J. Capone, Multiaxis Thrust-Vectoring Characteristics of a Model Representative of the F-18 High-Alpha Research Vehicle at Angles of Attack From 0° to 70° , NASA TP-3531, December 1995.
- [4] B. A. Blake, Numerical Investigation of Fluidic Injection as a Means of Thrust Modulation, Final Thesis Report , University of New South Wales, Australian, 2009.
- [5] P. C. Murphy and J. B. Davidson, Control Design for Future Agile Fighters, AIAA Paper No. 91-2882, Atmospheric Flight Mechanics Conference, New Orleans, Louisiana, 1991.
- [6] John S. Orme, Ross Hathaway, Initial Flight Test Evaluation of the F-15 ACTIVE Axisymmetric Vectoring Nozzle Performance, NASA/TM-1998-206558.
- [7] S. C. Asbury, Internal Performance of a Fixed-Shroud Nonaxisymmetric Nozzle Equipped with an Aft-Hood Exhaust Deflector, NASA/TM-97-206255.
- [8] A. J. Neely , F. N. Gesto and J. Young, Performance Studies of Shock Vector Control Fluidic Thrust Vectoring, AIAA-2007-5086, 43rd AIAA/ASME/SAE/ASEE Joint Propulsion Conference & Exhibit, Cincinnati, OH, 2007.
- [9] M. Corcoran and T. Matthewson, Thrust Vectoring, Aeronautical Engineering I, 2006.
- [10] R. Burse and R. Dickinson, Flight Test Results of the F-15 SMTD Thrust Vectoring/Thrust Reversing Exhaust Nozzle, AIAA-90-1906.
- [11] John S. Orme, Robert L. Sims, Selected Performance Measurements of the F-15 ACTIVE Axisymmetric Thrust-Vectoring Nozzle, Paper No. IS 166, 14th ISABE Annual Symposium, Florence, Italy, September 1999.
- [12] V. Regenie, D. Gatlin and N. Matheny, The F-18 High Alpha Research Vehicle: A High Angle-of -Attack Testbet Aircraft, NASA TM-104253, 1992.
- [13] David F. Fisher and Daniel G. Murri, Forebody Aerodynamics of the F-18 High Alpha Research Vehicle with Actuated Forebody Strakes, Paper presented at the RTO AVT Symposium, Norway, RTO-MP-069(I), 2001.
- [14] K. W. Iliff and K. C. Wang, Flight-Determined Subsonic Longitudinal Stability and Control Derivatives of the F-18 High Angle of Attack Research Vehicle (HARV) With Thrust Vectoring, NASA /TP -97-206539, 1997.
- [15] C. Bolkcom, F-22A Raptor, CRS Report for Congress, 2006.

- [16] B. L. Berrier, and M. L. Mason, Static Performance of an Axisymmetric Nozzle with Post-Exit Vanes for Multiaxis Thrust Vectoring, NASA TP-2800, 1988.
- [17] B. L. Berrier, Internal Performance of Two Nozzles Utilizing Gimbal Concepts for Thrust Vectoring, NASA TP-2991, 1990.
- [18] Gal-Or B., Fundamental Concepts of Vectored Propulsion, Journal of Propulsion v6 No. 6, 1990.
- [19] J. D. Flamm and K. A. Deere, Experimental Study of an Axisymmetric Dual Throat Fluidic Thrust Vectoring Nozzle for Supersonic Aircraft Application, American Institute of Aeronautics and Astronautics, 2007.
- [20] A. E. Bare and D. E. Reubush, Static Internal Performance Including of a Two-Dimensional Convergent-Divergent Nozzle with Thrust Vectoring, NASA TP-2721, 1987.
- [21] F. W. Burcham, Jr., R. J. Ray, Propulsion Flight Research at NASA Dryden from 1967 to 1997, NASA/TP-1998-206554.
- [22] J. G. Taylor, A Static Investigation of a Simultaneous Pitch and Yaw Thrust Vectoring 2-D C-D Nozzle, AIAA 88-2998.
- [23] B. L. Berrier, Results from NASA Langley Experimental Studies of Multiaxis Thrust Vectoring Nozzles, SAE TP-881481, 1988.
- [24] A. H. Bowers, J. W. Pahle, An Overview of the NASA F-18 High Alpha Research Vehicle, NASA Technical Memorandum 4772, 1996.
- [25] Jeffrey D. Flamm, Experimental Study of a Nozzle Using Fluidic Counterflow for Thrust Vectoring, AIAA 98-3255.
- [26] M. U. Sadiq, Performance Analysis and Flowfield Characterization of Secondary Injection Thrust Vector Control (SITVC) for a 2DCD Nozzle, A Thesis Presented to the Faculty of the Viterbl School of Engineering, University of southend California, 2007.
- [27] C. Chiarelli, R. K. Johnsen and C. F. Shieh, Fluidic Scale Model Multi-Plane Thrust Vector Control Test Results. AIAA 93-2433.
- [28] K. A. Deere, PAB Simulations of a Nozzle with Fluidic Injection for Yaw Thrust-Vector Control, AIAA 98-3254.
- [29] Karen A. Deere, Bobby L. Berrier, Computational Study of Fluidic Thrust Vectoring Using Separation Control in a Nozzle, 21st AIAA Applied Aerodynamics Conference AIAA-2003-3803, Orlando, FL.
- [30] J. Federspiel and L. L. Bangert, Fluidic Control of Nozzle Flow-Some Performance Measurements. AIAA 95-2605.
- [31] E. G. Collins, Feedback Control for Counterflow Thrust Vectoring, proceeding of the 2004 American Control Conference Boston, Massachusetts, 2004.
- [32] D. J. Wing, V. J. Giuliano, Fluidic Thrust Vectoring of an Axisymmetric exhaust nozzle at

- static conditions, ASME Fluids Engineering Division Summer Meeting, 1997.
- [33] P. J. Strykowski and A. Krothapalli, An Experimental Investigation of Active Control of Thrust Vectoring Nozzle Flow Fields, Air Force Office of Scientific Research, Boling Air Force Base, Final Report for the period, 1993.
- [34] E. Gamble and D. Haid, Improving Off-Design Nozzle Performance Using Fluidic Injection, AIAA-2004-1206.
- [35] J. W. Smolka, F-15 ACTIVE Flight Research Program, Society of Experimental Test Pilots, 40th Symposium Proceedings, 1996.
- [36] F. Saghafi, A. Banazadeh, In-Trim Flight Investigations of a Conceptual Fluidic Thrust-Vectored Unmanned Tail-Sitter Aircraft, JAST, Vol.3, No.3, pp125-133, 2006.
- [37] A. Banazadeh and F. Saghafi, Experimental and Computational Investigation into the Use of Co-flow Fluidic Thrust Vectoring on a Small Gas Turbine, the Aeronautical Journal, p17-25, 2008.
- [38] D. Allen and B. L. Smith, Axisymmetric Coanda-assisted vectoring, Exp Fluids (2009) 46: 55–64, 2009.
- [39] A. Sobester, A. J. Keane, Multi-objective Optimal Design of a Fluidic Thrust Vectoring Nozzle, AIAA Paper, 6916, 2006.
- [40] Hunter, C. A., Deere, K. A., Computational Investigation of Fluidic Counterflow Thrust Vectoring, AIAA 99-2669.
- [41] G. F. Schmid and P. J. Strykowski, Jet Attachment Behavior Using Counterflow Thrust Vectoring, Proceedings of 13th ONR Propulsion Conference, Minneapolis, MN, 2000.
- [42] Van der Veer M., Strykowski P. J., Counterflow Thrust Vector Control of Subsonic Jets: Continuous and Bistable Regimes, Journal of Propulsion and Power v13 No.3, 1997.
- [43] V. J. Giuliano, D. J. Wing, Static Investigation of a Fixed-Aperture Exhaust Nozzle Employing Fluidic Injection for Multiaxis Thrust Vector Control, AIAA 97-3149.
- [44] P. J. Strykowski and D. J. Forliti, Flow Control Applications using Countercurrent Shear, International Symposium on Recent Advances in Experimental Fluid Mechanics , India, 2000.
- [45] D. M. Washington, F. S. Alvil, Multiaxis Fluidic Thrust Vector Control of a Supersonic Jet Using Counterflow, AIAA JOURNAL Vol. 34, No. 8, August 1996.
- [46] A. Krothapalli, D. J. Forliti, Thrust Vector Control of Rectangular Jets Using Counter Flow, FMRL-TR95-1.
- [47] David J. Wing, Static Performance Investigation of a Skewed-Throat Multiaxis Thrust-Vectoring Nozzle Concept, NASA Technical Paper 3411, 1994.
- [48] David J. Wing, Charles T. L. Mills, Static Investigation of a Multiaxis Thrust-Vectoring Nozzle with Variable Internal Contouring Ability, NASA Technical Paper 3628, 1997.
- [49] Karen A. Deere, Bobby L. Berrier, A Computational Study of a New Dual Throat Fluidic Thrust Vectoring Nozzle Concept, American Institute of Aeronautics and Astronautics Shock Vector

Control, 2005.

[50] Miller, D. N., Yagle, P. J., and Hamstra, J. W., Fluidic Throat Skewing for Thrust Vectoring in Fixed Geometry Nozzles, AIAA 99-0365.

[51] K. A. Deere, Summary of Fluidic Thrust Vectoring Research Conducted at NASA Langley Research Center, AIAA-2003-3800.

[52] Gridley, M. C., Walker, S. H., Inlet and Nozzle Tech. for 21st Century Aircraft, ASME 96-GT-244.

[53] Andrew J. Neely, Fernando N. Gesto, Performance Studies of Shock Vector Control Fluidic Thrust Vectoring, 43rd AIAA/ASME/SAE/ASEE Joint Propulsion Conference & Exhibit, Cincinnati, OH, AIAA 2007-5086.

[54] W. K. Lord, D. G. MacMartin, Flow Control Opportunities in Gas Turbine Engines, AIAA 2000-2234.

[55] P. J. Yagle, D. N. Miller, Demonstration of Fluidic Throat Skewing for Thrust Vectoring in Structurally Fixed Nozzles, ASME Vol. 123, 2001.

Chapter 2 Fundamental Theory of Numerical Studies

As a branch of fluid mechanics, computational fluid dynamics (CFD) is a method that uses numerical methods and algorithms to solve flow problems and to analyze fluid phenomenon. Based on high-performance supercomputers, the simulations of liquids and gases flows can be obtained well. CFD constitutes a new third approach to the philosophical study and development of the whole discipline of fluid dynamics except experimental and theoretical fluid dynamics. CFD today is an equal partner with pure theory and pure experiment in the analysis and solution of fluid dynamic problems [1].

2.1 The Governing Equations

The fundamental bases of all CFD problems are governed by three fundamental principles:

1. Mass is conserved.
2. Newton's second law (force=mass \times acceleration).
3. Energy is conserved.

These fundamental equations are totally corresponded with the governing equations of fluid dynamics in Appendix A. The governing equations of conservation laws (2D) for inviscid flows (Euler equations) are expressed as

$$U_t + F_x + G_y = 0, \quad (2-1)$$

$$U = \begin{bmatrix} \rho \\ \rho u \\ \rho v \\ E \end{bmatrix}, \quad (2-2)$$

$$F = \begin{bmatrix} \rho u \\ \rho u^2 + p \\ \rho uv \\ u(E + p) \end{bmatrix}, \quad G = \begin{bmatrix} \rho v \\ \rho uv \\ \rho v^2 + p \\ v(E + p) \end{bmatrix}, \quad (2-3)$$

where ρ and p are the density and pressure and u and v are the x and y components of velocity, respectively; E is the total energy per unit volume. Vector U represents conserved variables, and F and G are the fluxes in the x and y directions, respectively. When viscosity and heat conduction are added to the basic equations, F and G are modified to a Navier-Stokes conservation form such as

$$F = F^a - F^d, \quad G = G^a - G^d, \quad (2-4)$$

where the flux vectors F^a and G^a are the inviscid fluxes for the Euler equations, as given by (2-3). The flux vectors F^d and G^d attributed to the viscosity and heat conduction are shown as

$$F^d = \begin{bmatrix} 0 \\ \tau_{xx} \\ \tau_{xy} \\ u\tau_{xx} + v\tau_{xy} + kT_x \end{bmatrix}, \quad G^d = \begin{bmatrix} 0 \\ \tau_{yx} \\ \tau_{yy} \\ u\tau_{yx} + v\tau_{yy} + kT_y \end{bmatrix}, \quad (2-5)$$

where

$$\tau_{xx} = \frac{2}{3}\mu(2u_x - v_y), \quad \tau_{yy} = \frac{2}{3}\mu(2v_y - u_x), \quad \tau_{xy} = \tau_{yx} = \mu(u_y + v_x). \quad (2-6)$$

The components of stress tensor τ are expressed as functions of velocity gradients u_x , u_y , v_x , v_y and the coefficient of viscosity μ . Symbol k is the thermal conductivity, and T_x and T_y are the x and y derivatives of temperature, respectively.

The Sutherland's law give the relationship between the dynamic viscosity μ , and the absolute temperature T_0 for the perfect gas. The equation can be expressed as

$$\mu = \mu_{ref} \left(\frac{T_0}{T_{ref}} \right)^{3/2} \frac{T_{ref} + S}{T_0 + S}, \quad (2-7)$$

where T_{ref} is a reference temperature, μ_{ref} is the viscosity at the T_{ref} , and S is the Sutherland temperature. When $T_0 = 288.15K$, the $\mu = 1.17894 \times 10^{-5} N \cdot s / m^2$, and the constant $S = 110.4K$.

2.2 The Finite Volume Method and the Riemann Problem

The finite volume method (FVM) is a method for representing and evaluating partial differential equations (PDEs) in the form of algebraic equations. The method divides space into volumes surrounding nodes point and computes the change within each volume by considering the flux (flow rate) across the surfaces of the volume. Since the flux entering a given volume is identical to that leaving the adjacent volume, the method is conservative.

The Riemann problems appear in FVM for the solution of equation of conservation laws with piecewise constant data in the grid. Since the shocks, rarefaction waves, and contact discontinuity appear as characteristics in the Riemann solution, the Riemann problem can provide exact solution to complex, nonlinear equations. The Riemann problem also can help understand hyperbolic partial differential equations such as Euler equations and assess the performance of numerical methods [2].

The initial value problem (IVP) for a hyperbolic of system of one-dimensional time-dependent Euler equations mentioned in 2.1 is considered. Figure 2.1 illustrates the initial data for the Riemann problem. The initial condition (IC) consists of two constant states separated by a discontinuity at

$x = 0$ [3].

$$U(x,0) = U^{(0)}(x) = \begin{cases} U_L, & x < 0, \\ U_R, & x > 0. \end{cases} \quad (2-8)$$

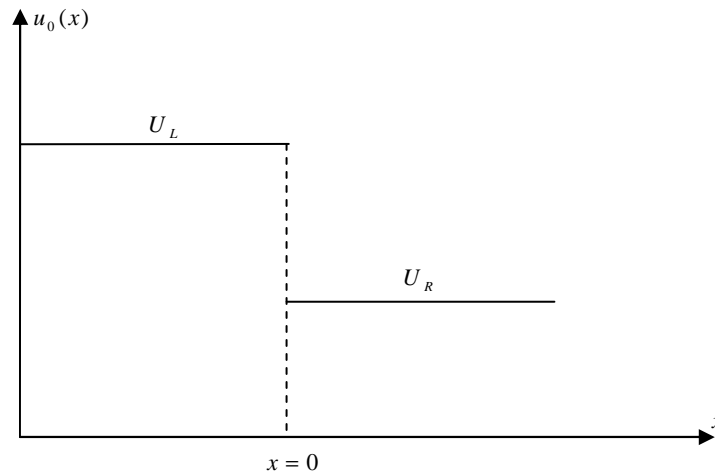


Figure 2.1 Illustration of the initial data for the Riemann problem.

2.3 Godunov's Method

The flow solution of Godunov method is represented by a series of piecewise constant states. The method can self-operate treatment of weak and strong shock waves and can closely approximate the solution near discontinuities. The discretized flow solutions are evolved by considering the nonlinear interactions and the Riemann problems can be advanced by the averaged solutions. The Godunov's method can get a well-behaved treatment of shock waves based on the relevant physics.

The disadvantage of Godunov's method is difficult to get the exact solution to the Riemann problem, especially for complex flows. The exact solutions require complex and time-consuming iterative procedure which restrict the extensive applications of Godunov-type method. In order to overcome the drawback, several approximations for the purpose of computing the Godunov flux have been developed [4].

2.4 Riemann Solvers

The Riemann solvers are shock capturing methods and are widely used for high speed flows. Harten, Lax, and van Leer presented a direct approximation of the numerical flux to compute Godunov flux. The resulting Riemann solver is known as HLL Riemann solves. It can satisfy entropy property, and resolve isolated shock efficiently. The central idea is that the wave configuration for the solution that

consists of two waves separating three constant states. The right and left waves are shock or rarefaction waves. The main drawback of the HLL scheme is that it ignores the existence of the discontinuity. In view of the shortcoming of the HLL approach, a modification called the HLLC Riemann solver (C stand for contact), wherein the missing contacts are restored, was presented by Toro, Spruce, and Speares [5-6].

2.4.1 The Original HLL-Riemann Solver

The single constant is assumed between two nonlinear waves (shock or rarefaction). In the following Riemann solver

$$U(x,t) = \begin{cases} U_L, & x/t \leq S_L, \\ U^{hll}, & S_L \leq x/t \leq S_R, \\ U_R, & x/t \geq S_R, \end{cases} \quad (2-9)$$

where U^{hll} is the constant state vector and S_L and S_R are the fastest signal velocities perturbing the initial data state U_L and U_R

$$U^{hll} = \frac{S_R U_R - S_L U_L + F_L - F_R}{S_R - S_L}. \quad (2-10)$$

The corresponding intercell flux is given by

$$F_{i+1/2}^{hll} = \begin{cases} F_L, & 0 \leq S_L \\ \frac{S_R F_L - S_L F_R + S_L S_R (U_R - U_L)}{S_R - S_L}, & S_L \leq 0 \leq S_R \\ F_R, & 0 \geq S_R \end{cases} \quad (2-11)$$

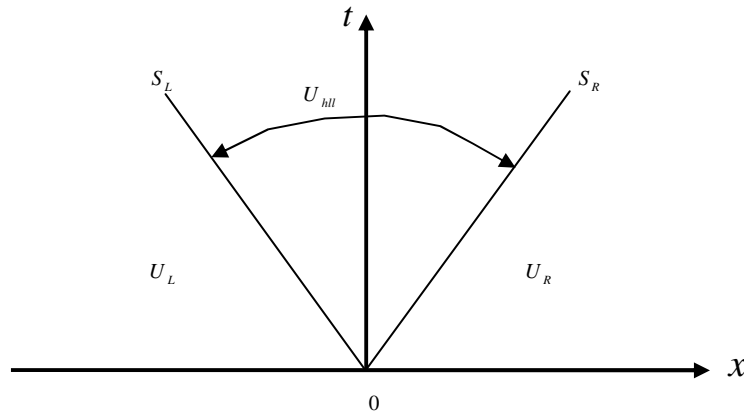


Figure 2.2 HLL Riemann solver.

Figure 2.2 shows the HLL approximate Riemann solver. Solution in the star region consists of a

single state separated from data states by two waves of speed S_L and S_R .

2.4.2 The HLLC-Riemann Solver

Figure 2.3 shows the HLLC approximate Riemann solver. Solution in the Star Region consists of two constant states separated from each other by a middle wave of speed S_* .

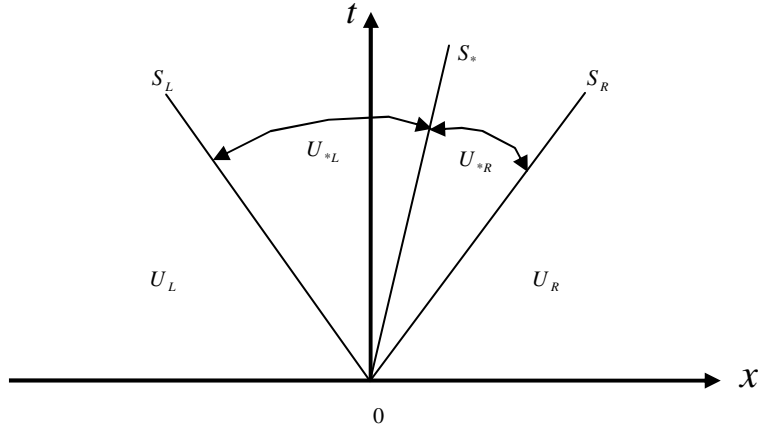


Figure 2.3 HLLC Riemann solver.

The HLLC intercell flux is written as

$$F_{i+1/2}^{hllc} = \begin{cases} F_L, 0 \leq S_L \\ F_{*L} = F_L + S_L(U_{*L} - U_L), S_L \leq 0 \leq S_* \\ F_{*R} = F_R + S_R(U_{*R} - U_R), S_* \leq 0 \leq S_R \\ F_R, 0 \geq S_R \end{cases}, \quad (2-12)$$

U_{*L} and U_{*R} are the conserved variable vectors in the star region separated by the contact discontinuity. F_{*L} and F_{*R} are obtained by applying Rankine-Hugoniot conditions across each wave. Variables of states in the star region are obtained with jump conditions across each wave

$$U_{*K} = \rho_K \begin{pmatrix} 1 \\ S_* \\ v_K \\ w_K \\ \frac{E_K}{\rho_K} + (S_* - u_K) \left[S_* + \frac{p_K}{\rho_K(S_K - u_K)} \right] \end{pmatrix}, \quad (2-13)$$

for $K = L$ and $K = R$.

2.4.3 Wave Speed Estimates

To compute wave speeds S_L , S_R and S_* , the pressure-velocity based wave estimations are used to estimate the shock and the rarefaction waves.

$$S_L = u_L - a_L q_L, \quad (2-14)$$

$$S_* = u_*, \quad (2-15)$$

$$S_R = u_R - a_R q_R, \quad (2-16)$$

where

$$q_K = \begin{cases} 1, & p_* \leq p_K \\ \left[1 + \frac{\gamma+1}{2\gamma} \times \frac{p_*}{p_K-1} \right]^{1/2}, & p_* > p_K \end{cases}. \quad (2-17)$$

The following solutions for pressure in the star region,

$$p_{*L} = p_L + \rho_L (S_L - u_L)(S_* - u_L), \quad (2-18)$$

$$p_{*R} = p_R + \rho_R (S_R - u_R)(S_* - u_R), \quad (2-19)$$

$$p_{*L} = p_{*R} = p_*. \quad (2-20)$$

The S_* is gotten as follows

$$S_* = \frac{p_R - p_L + \rho_L u_L (S_L - u_L) - \rho_R u_R (S_R - u_R)}{\rho_L (S_L - u_L) - \rho_R (S_R - u_R)}. \quad (2-21)$$

2.5 Weighted Average Flux

The weighted average flux (WAF) approach is the high order extension of the Godunov scheme and is second-order accurate both in space and time [7]. The WAF approach is deterministic and leads to fully discrete, explicit second order accurate schemes.

Consider the model hyperbolic conservation law

$$U_t + F(U)_x = 0. \quad (2-22)$$

The conservative time marching schemes of the form

$$U_i^{n+1} = U_i^n + \frac{\Delta t}{\Delta x} [F_{i-1/2} - F_{i+1/2}], \quad (2-23)$$

where U_i^n is variable piecewise constant cell averages, Δt and Δx are the time step size and computing cell length, respectively, and $F_{i-1/2}$ and $F_{i+1/2}$ are intercell numerical fluxes.

The intercell flux was defined as an integral average of the flux function, namely

$$F_{i+1/2}^{waf} = \frac{1}{\Delta x} \int_{\frac{1}{2}\Delta x}^{\frac{3}{2}\Delta x} F \left[U_{i+1/2} \left(x, \frac{1}{2} \Delta t \right) \right] dx, \quad (2-24)$$

The integration domain is subdivided into two segments

$$F_{i+1/2}^{waf} = \frac{1}{2} (1+c)(aU_i^n) + \frac{1}{2} (1-c)(aU_{i+1}^n), \quad (2-25)$$

$$c = \frac{a\Delta t}{\Delta x}, 0 \leq c \leq 1, \quad (2-26)$$

The upwind flux $F_i = aU_i^n$ with weight $\beta_1 = 1/2(1+c)$ and the downwind flux $F_i = aU_{i+1}^n$ with weight $\beta_2 = 1/2(1-c)$. Here c is the Courant number. The upwind weight is always larger than the downwind weight and thus the WAF method is upwind biased. Figure 2.4 shows the evaluation of the WAF flux for the linear advection equation at $a > 0$.

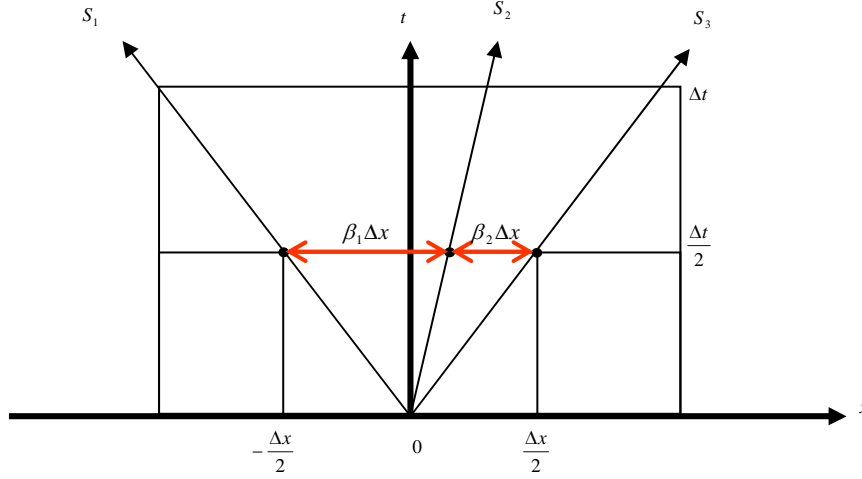


Figure 2.4 Evaluation of the WAF flux for the linear advection equation.

2.6 Splitting Schemes for Two-dimensional Systems

Consider the two-Dimensional initial value problem

$$\begin{cases} U_t + F(U)_x + G(U)_y = 0, \\ U(x, y, t^n) = U^n \end{cases}, \quad (2-27)$$

The initial data is given by U^n of discrete cell average values.

By a pair of one dimensional initial value problems, the (2-27) is replaced as

$$\begin{cases} U_t + F(U)_x = 0 \\ U^n \end{cases} \Rightarrow U^{n+1/2}, \quad (2-28)$$

$$\begin{cases} U_t + G(U)_y = 0 \\ U^{n+1/2} \end{cases} \Rightarrow U^{n+1}. \quad (2-29)$$

Index i refers to the x-coordinate direction and index j refers to the y-coordinate direction. Firstly, the problem is solved in the x-direction for a time step Δt . This is x sweep and the solution is $U^{n+1/2}$ for each strip labeled j . Next, the problem is solved in the y-direction for the time step Δt . This is y sweep and the $U^{n+1/2}$ solution is the initial condition for the second initial value problem for each strip labeled i . Figure 2.5 shows the discretisation of two-dimensional Cartesian domain

into finite volumes I_{ij} of area $\Delta x \times \Delta y$ [8].

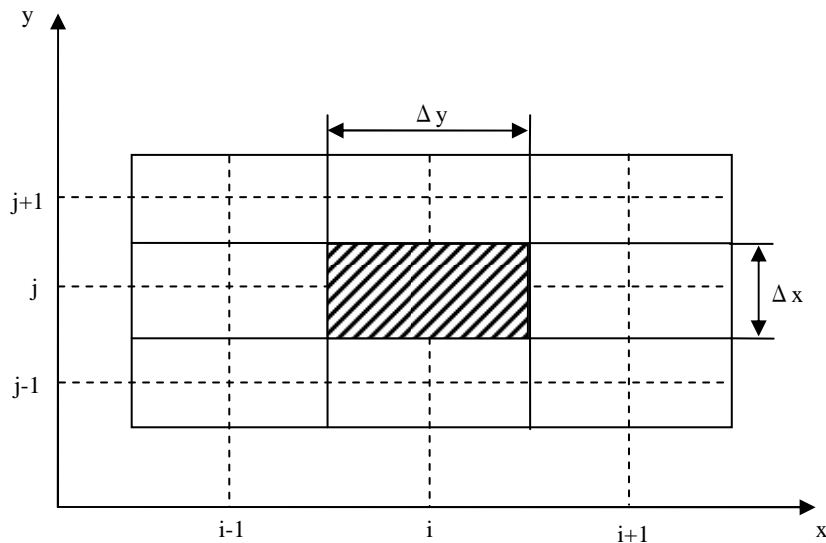


Figure 2.5 Discretisation of two-dimensional Cartesian domain into finite volumes.

2.7 Parallel Computing Method

Parallel computing is a form of computation which uses multiple processing elements simultaneously to solve enormous problems. This is achieved by dividing the large problems into small ones so that each processing element can execute part of the algorithm simultaneously. The processing elements can be diverse such as a single computer with multiple processors, several networked computers, specialized hardware ect. [9].

Concurrent programming languages have been created for programming parallel computers. Those are divided by memory architecture: shared memory, distributed memory, and shared distributed memory. Shared memory programming languages, such as OpenMP and Pthread, communicate by manipulating shared memory variables, whereas distributed memory uses message passing, such as MPI (Message Passing Interface) and PVM (Parallel Virtual Machine). The program used in this study is accomplished by Cray XD1, which is based on MPI.

MPI is a language independent communications protocol used to program parallel computer and support point to point and collective communication. MPI is the dominant model used in high-performance computing for its high performance, scalability, and portability.

2.7.1 Parallelization Method of Two-Dimensional Code

In this study, the computational domain is distributed evenly to the number of processors. Figure 2.6

shows how to divide the computational domain in two dimensions to three parts when three processors are chosen. The number of the first processor is set to 0. The distribution is done in the direction j , the number of cells in the direction j is divided by three processors. The number of cells throughout the computational domain is $itotal \times jtotal$. If the number of cells in the divided region is $icells \times jcells$, the $icells = itotal$ and $jcells = jtotal/3$ for distribution in j direction.

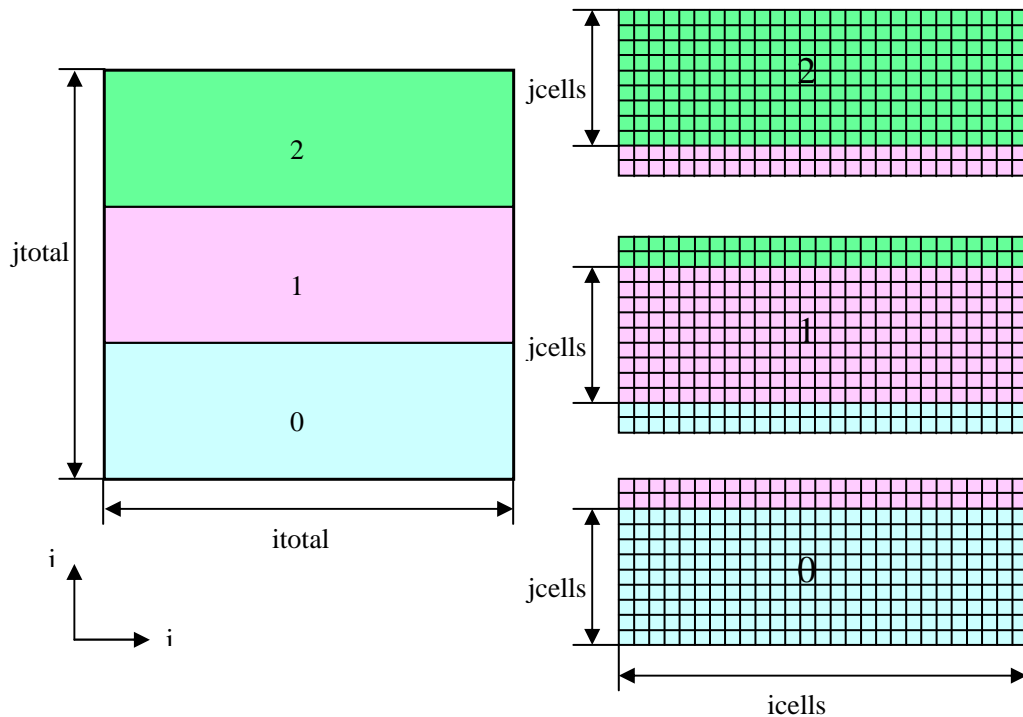


Figure 2.6 Computational domain distribution.

The name of part computational domain is set to 'me'. So, $me = 0$ means the 0 domain controlled by processor 0; $me = 1$ means the 1 domain controlled by processor 1; $me = 2$ means the 2 domain controlled by processor 2. So for 0 domain, the information of $j = -1$ (imaginary cell), 0 of the 1 domain lower boundary is necessary; for 2 domain, the information of $j = jcells+1, jcells+2$ (imaginary cell) of the 1 domain upper boundary is necessary, and for 1 domain, the information of $j = jcells+1, jcells+2$ of the 0 domain and $j = -1, 0$ of the 2 domain lower boundary is necessary. It means that it is necessary for the exchange information of the boundary region between the adjacent areas each computation step.

For Navier-Stokes calculation, the density, pressure, velocity in x, y directions, velocity derivative, and temperature derivatives are needed to be exchange in the adjacent boundary.

Reference

- [1] John D. Anderson, Jr. Computational Fluid Dynamics, Tsinghua University Press, 2002.
- [2] E. F. Toro, V. A. Titarev, Solution of the Generalized Riemann Problem for Advection–Reaction equations, Proceedings of the Royal Society, 2002.
- [3] Bernd Einfeldt, On Godunov-Type Methods for Gas Dynamics, Society for Industrial and Applied Mathematics, Vol. 25, No. 2, 1988.
- [4] James J. Quirk, A Contribution to the Great Riemann Solver Debate, NASA Contractor Report 191409 ICASE Report No. 92-64, 1992.
- [5] Sung Don Kim, Bok Jik Lee, Robust HLLC Riemann Solver with Weighted Average Flux Scheme for Strong Shock, Journal of Computational Physics, 2009.
- [6] E. F. Toro, M. Spruce, Restoration of the Contact Surface in the HLL-Riemann Solver, Shock Waves 4: 25-34, 1994.
- [7] S. J. Billett and E. F. Toro, On WAF-Type Schemes for Multidimensional Hyperbolic conservation Laws, Journal of Computational Physics 130, 1-24, 1997.
- [8] Eleuterio F. Toro, Riemann Solvers and Numerical Methods for Fluid dynamics (2nd Edition), Springer-Verlag Berlin Heidelberg, 1999.
- [9] 都志辉, 李三立, 高性能计算之并行编程技术—MPI 并行程序设计, 清华大学出版社, 2001.

Chapter 3 Preliminary Studies

In this chapter, the experimental and numerical studies of a preliminary shock vector control nozzle are presented. The experiments are performed with a nozzle pressure ratio (NPR) ranging from 4 to 10, a secondary pressure ratio (SPR) of 1 or 2, and two different secondary jet locations. Numerical simulations of the nozzle flow are carried out by solving the Navier-Stokes equations, and the input parameters are set to match the experimental conditions. Computations are performed with and without the secondary jet injection for different combinations of NPR, SPR, and jet location [1-3].

3.1 Experimental Setup

In this section, the experimental setup of the nozzle is introduced. The dimensions of the nozzle and the secondary jet cavity are presented, and instrumentations and Schlieren system for flow visualization are also introduced.

3.1.1 Experimental Facilities

The schematic diagram of the experimental facilities for measuring the pressure and for taking Schlieren images are shown in Fig.3.1.

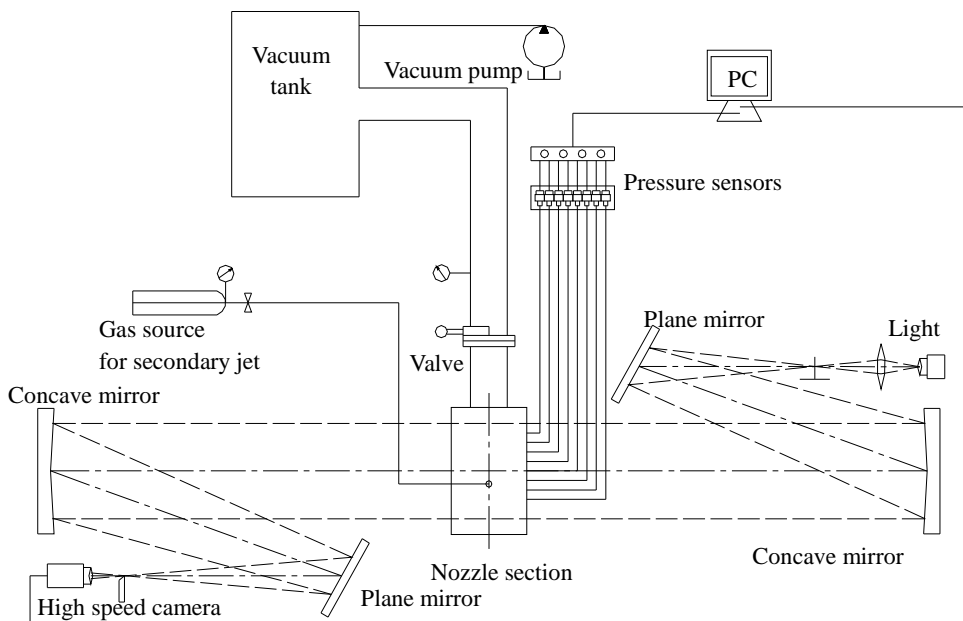


Figure 3.1 Schematic diagram of experimental setup.

The inlet of the nozzle is exposed to the atmosphere, whereas the outlet is connected to a vacuum tank. The vacuum tank has a large volume of 33 m^3 and the back pressure of the nozzle is kept practically constant at 0.1 atm during a typical test time of $5\text{--}10 \text{ s}$. Pressurized dry air is used as the gas source for the secondary jet. The photograph of the Schlieren system and the pressure transducers are shown in Fig.3.2.

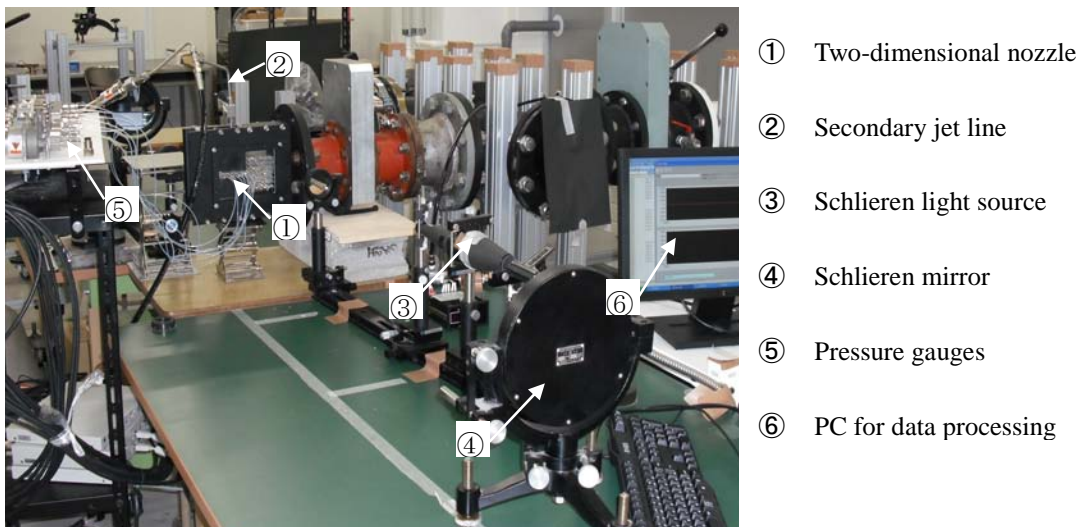


Figure 3.2 Photograph of the Schlieren system and the pressure transducers.

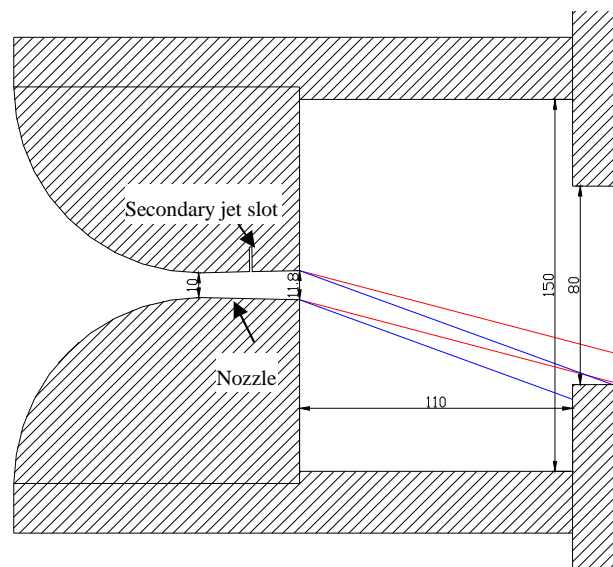


Figure 3.3 Dimensions of two-dimension nozzle and vacuum cavity.

The height of the nozzle throat is 10 mm , and the area ratio of the nozzle exit and the throat is 1.18 .

With this nozzle expansion ratio, the flow Mach number at the nozzle exit is expected to be 1.5 according to the inviscid quasi-one-dimensional analysis. The width of the secondary jet injection slot is 1 mm. Figure 3.3 shows the detailed dimensions of the nozzle and vacuum cavity downstream the nozzle exit. The opening diameter downstream of the nozzle exit is determined in such a way that the exhaust gas does not hit if the deflection angle is less than 15 degree. The flow deviating 15 degrees from the axis is shown with red lines, and the case for 20 degrees is shown with blue lines in the figure.

In this study, the distance between the secondary jet injection slot and the nozzle exit L_j is set either 5 or 10 mm. The dimensions of the nozzle with L_j of 10 mm are shown in Fig. 3.4. A cavity of a certain volume is made in the nozzle block to make the secondary flow stagnate.

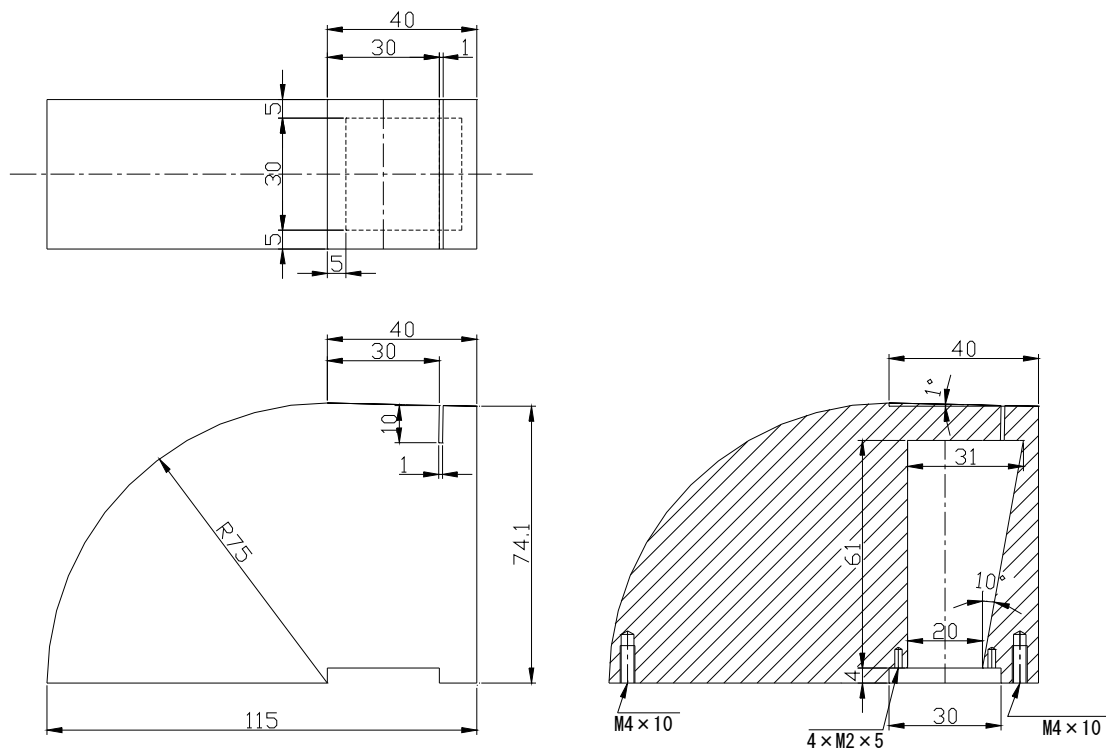


Figure 3.4 Dimensions of nozzle with secondary jet for $L_j = 10$ mm.

3.1.2 Instrumentations

The photograph of the static pressure measurement is shown in Fig. 3.5. The static pressure was measured using strain-type pressure gauges (PG-2KU and PG-20KU of Kyowa Electronic Instruments Co.). The rated capacities of the pressure gauges used in the main flow and secondary jet are 200 kPa and 2 MPa, respectively. The static pressure probes were spaced every 10 mm

starting at 30 mm upstream of the nozzle throat and extending to downstream of the nozzle exit along the centerline of the nozzle. The pressure gauges were calibrated with a GE Sensing DPI610 Calibrator. All pressure data from the test nozzle were recorded simultaneously. Measured pressure data are stored on PC by using the maker supplied interface (PCD 30A).

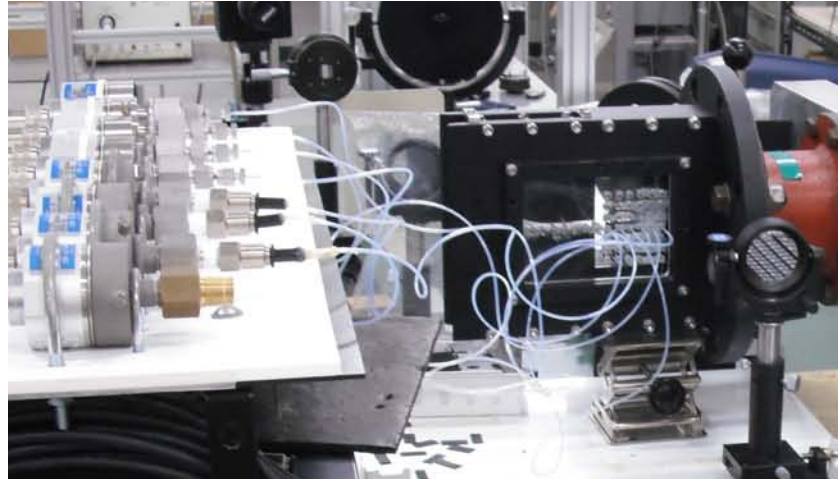


Figure 3.5 Photograph of static pressure measurement.

3.1.3 Flow Visualization

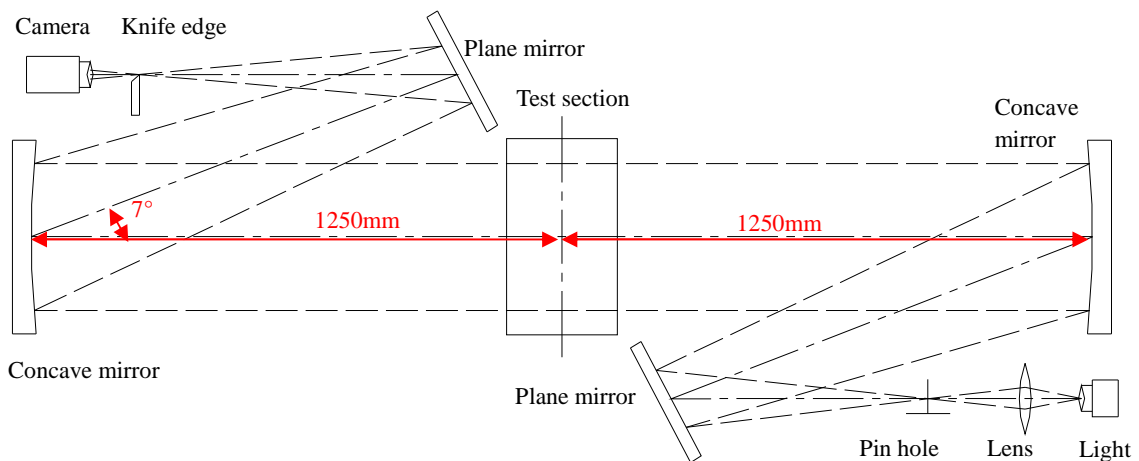


Figure 3.6 Schematic of the Schlieren system.

A standard Schlieren system was used to visualize the flow inside and downstream of the nozzle [4-5]. A light ray from a point light source passed the first plane mirror, two concave mirrors on each side of the nozzle, the second plane mirror, and a knife edge, reaching either a digital camera (Nikon D40X) or a high-speed video camera (Photron Fastcam MAXP01). The schematic of the Schlieren system is

shown in Fig. 3.6. The data collection interface of the high speed camera is shown in Fig. 3.7. The Photron FASTCAM Viewer interface is used for storing the Schlieren images.

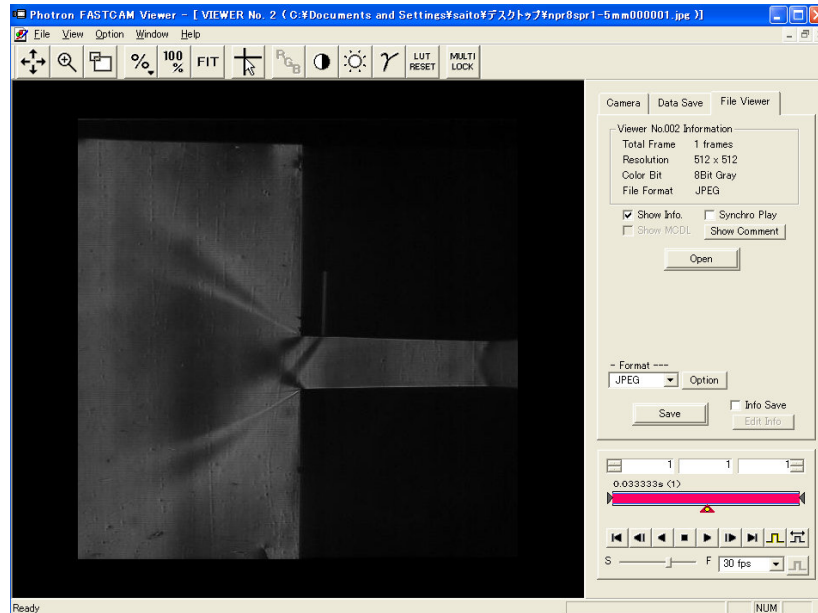


Figure 3.7 Data collection interface.

3.1.4 FTV Parameters for Experiments

The following parameters were used for data reduction. The NPR is the ratio of primary flow total pressure to nozzle back pressure, whereas the SPR is the ratio of secondary jet total pressure to primary flow total pressure. The conditions in the experiments and numerical simulations let the NPR range from 4 to 10 and the SPR was 1 or 2, with L_j set to 5 mm or 10 mm. The mass flow ratio of the secondary jet injection to the main flow is 10 % with $SPR = 1$ by Eq. (A-22), and the mass flow ratio is 20% with $SPR = 2$.

3.2 Numerical Simulations

In this section, the numerical method, initial and boundary conditions and numerical grids are presented. The fundamentals of the numerical studies are introduced in detail in Chapter 2.

3.2.1 Numerical Scheme

In this series of experiments, the Reynolds number of the flow at the nozzle exit is calculated to be 6.2×10^5 , which corresponds to the transition zone from laminar to turbulent flow. The flow at the

inlet, however, is smooth since it is accelerated from the stationary atmosphere and the transition is expected to be suppressed till relatively high Reynolds number. This is visually confirmed with Schlieren images. Therefore, in this study, the flow is assumed to be laminar. The Navier-Stokes equations together with mass, momentum and energy conservation equations are solved numerically. The numerical fluxes are evaluated with the HLLC Riemann solution, and the numerical simulations were carried out with the WAF method. The WAF scheme is one of the higher order extensions of the Godunov scheme with second order accuracy in both space and time.

3.2.2 Initial and Boundary Conditions

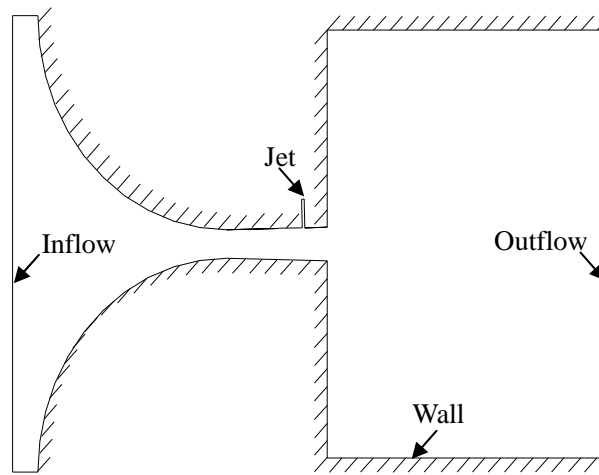


Figure 3.8 Flow domain and the boundary conditions.

Initial and boundary conditions are defined to initialize and constrain the flow properly. The inflow boundary condition is set to atmospheric conditions. The pressure and other flow parameters at the nozzle exit are calculated from the NPR. The conditions are distributed over the flow domain as initial conditions. Figure 3.8 shows the boundary conditions of the entire flow field. In short, the inflow boundary condition means that the inlet is fixed to the atmospheric conditions, while the outflow boundary condition means that the flow is not reflected there. Further, the jet boundary condition is determined by the SPR, and the wall boundary condition means a reflective solid wall. Computations were carried out for combinations of NPR and SPR corresponding to those in experiments.

3.2.3 Numerical Grids

Figure 3.9 shows the structured grids of the flow field that are used in this study. The grid cells

allocated for the entire computational domain were 143,606 for the case of $L_j = 5$ mm and 145,622 for the case of $L_j = 10$ mm. The calculation time was approximately 7 hours to complete one case using 10 processing elements of a Cray XD1. The region downstream of the nozzle exit extends 0.11 m along the x-axis, and the height of the region is approximately 0.15 m. The flow domain is divided into three regions as indicated with different colors. Each region is computed by a different CPU of the parallel computers. A separated CPU is assigned for the computation of the secondary jet path.

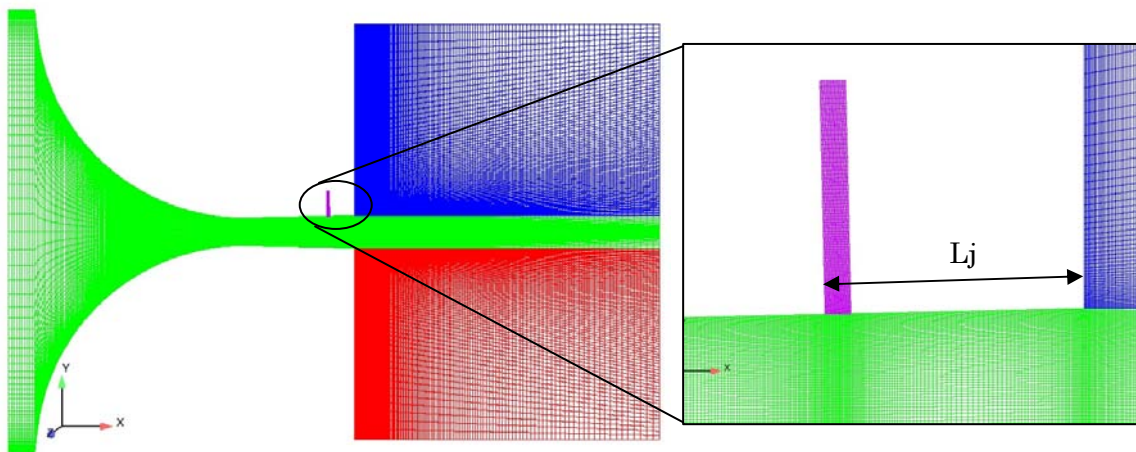


Figure 3.9 Numerical grids of the flow field.

3.2.4 Parameters in Computation

The following conventions were used for data reduction are the same as those of the experiment.

3.3 Results and Discussion

Experimental data were chosen for $L_j = 5$ and 10 mm, with NPR varied from 4 to 10 and SPR set either to 1 or 2. Two cases of typical nozzle flow with and without secondary jet are carried out. Presented and discussed below are the static pressure on the nozzle wall, the thrust pitching moment, and the internal flow features (i.e., static pressure along the nozzle centerline, pressure distribution, Mach number distribution, and flow streamlines).

3.3.1 Nozzle Performance without Secondary Jet

Figure 3.10 shows the flow field with different NPRs.

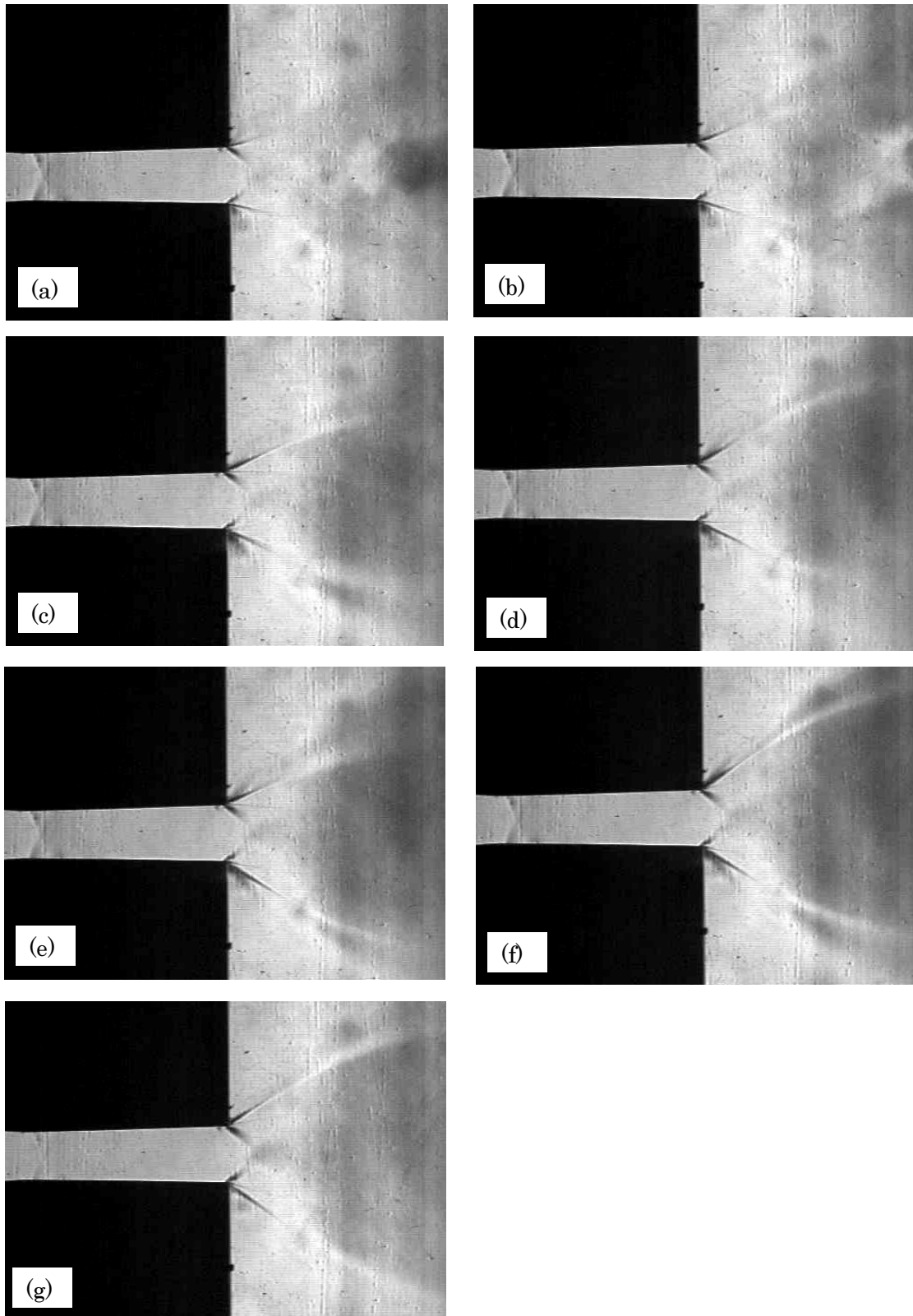


Figure 3.10 Schlieren pictures for different NPRs:

(a) NPR=4, (b) NPR=5, (c) NPR=6, (d) NPR=7, (e) NPR=8 , (f) NPR=9, (g) NPR=10.

Since the back pressure is lower than the designed nozzle pressure (i.e., 0.027 MPa), the flow is under-expanded. It is seen that the extent of the expansion fan at the nozzle exit increases with the NPR. Near the nozzle throat, two oblique shocks are clearly seen. The nozzle shape is circular from the inlet to the throat. It is straight from the throat to the nozzle exit and, though it is very small, there is a kink in the nozzle shape at the throat. This produces compression waves visible with the Schlieren method.

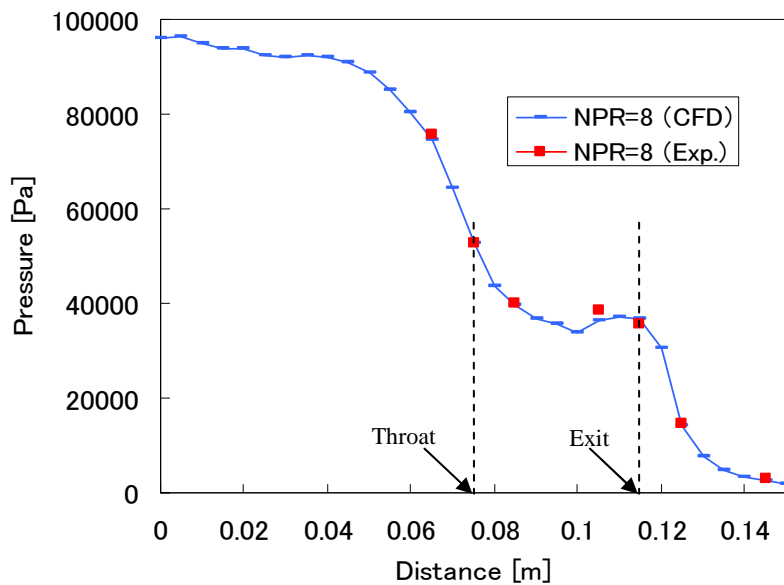


Figure 3.11 Static pressure at nozzle centerline without secondary jet.

Figure 3.11 shows the measured and computed static pressures along the nozzle centerline with $NPR = 8$. The pressure in the nozzle decreases from atmospheric pressure to back pressure. It can be observed that the numerical and the experimental results are in good agreement with each other. The pressure distributions with other values of NPR have similar tendency.

3.3.2 Nozzle Performance with Secondary Jet

The nozzle performance with secondary jet is discussed in detail by analyzing the flows inside the nozzle. The thrust pitching moment is evaluated from the pressure distributions on the nozzle wall. A new method for evaluating the FTV performance using the pitching moment is proposed in this study.

3.3.2.1 Flows Configurations around the Secondary Jet Exit

Figure 3.12 shows the schematics of flow configuration around the secondary jet slot with $SPR = 1$ and $SPR = 2$. It shows the interaction of the secondary jet with the main nozzle flow. The secondary jet works as obstruction and the boundary layer is separated due to the adverse pressure gradient and a lambda-shape shock system is formed. The oblique shock wave generated in this manner will deflect the main flow downwards if the jet is injected from the upper wall as in Fig.3.12. This is the mechanism that is normally expected for the FTV using oblique shock wave.

It is noted that when SPR is small, as shown in Fig. 3.12(a), the secondary jet is turned back toward the nozzle wall and re-attaches to the wall. However, as in Fig. 3.12(b), when the SPR is relatively large, the secondary jet does not re-attach to the nozzle wall. In the latter case, Fig. 3.12(b), the area behind the secondary jet is connected to the region outside the nozzle exit and the pressure of the nozzle wall in this range is quite low.

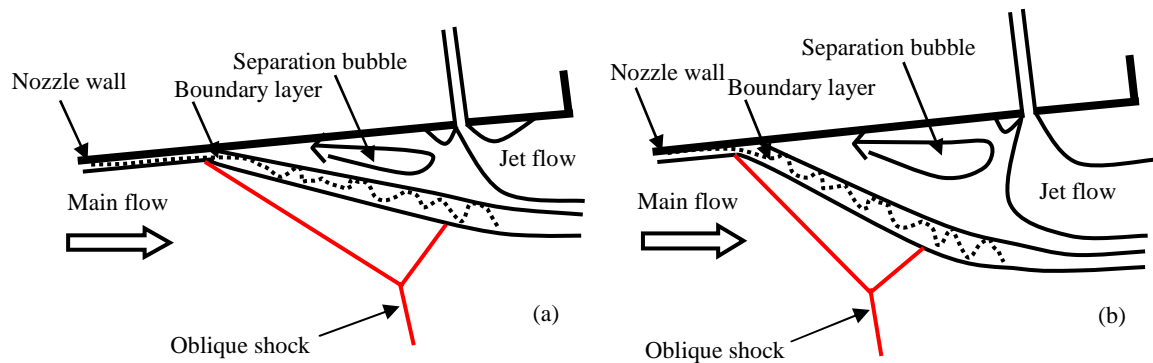


Figure 3.12 Interaction of secondary jet with primary flow at (a) $SPR = 1$ or (b) $SPR = 2$.

Figure 3.13 shows the pressure distributions for $L_j = 5$ mm with $NPR = 8$ and $SPR = 1$ or 2. The pressure upstream of the secondary jet slot increases with the SPR . As shown in Fig. 3.13(a), with a small SPR , not many wave interactions are observed in the nozzle diverging section. With increase in SPR , Fig. 3.13(b), the high-pressure zone extends to the nozzle throat and forms complex wave interactions in the whole region of the nozzle. A noticeably low pressure is observed behind the secondary jet injection point. In the case of $L_j = 10$ mm, the flow pattern in general is similar to that of $L_j = 5$ mm. It is observed, however, that the oblique shock wave produced by the secondary jet reflects at the lower nozzle wall. It is shown later in Figs. 3.15 and 3.16.

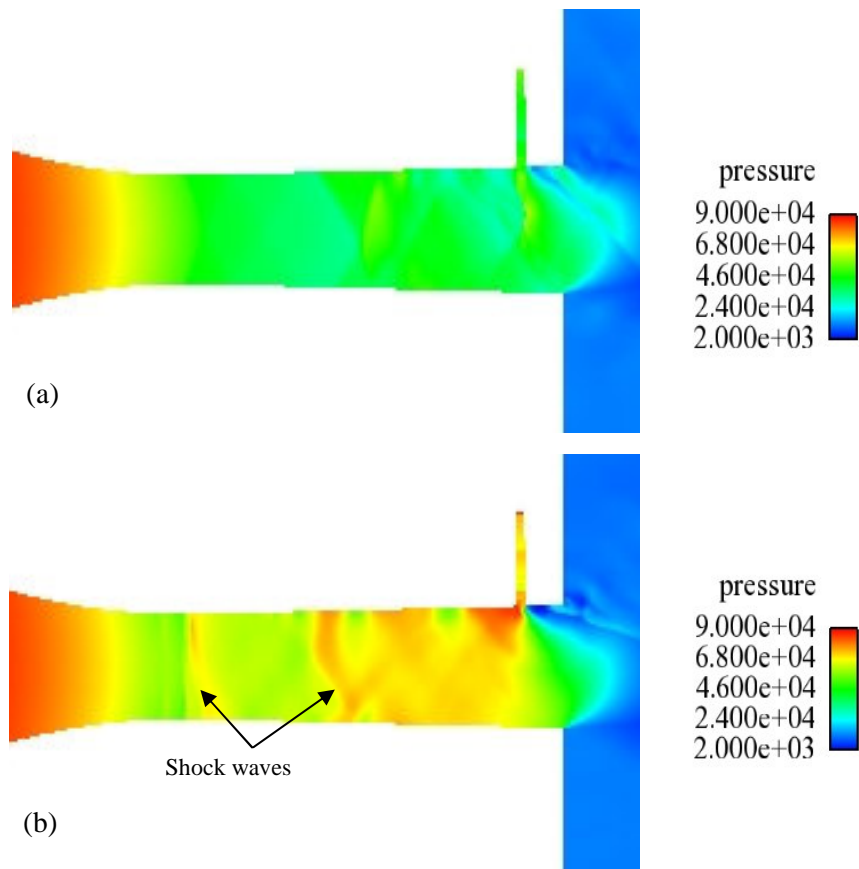


Figure 3.13 Static pressure distribution in diverging nozzle section with NPR = 8 and (a) SPR = 1 or (b) SPR = 2.

Figure 3.14 shows flow Mach number distributions for $L_j = 5$ mm with NPR = 8 and SPR = 1 or 2. The main flow accelerates in the converging section of the nozzle and reaches sonic speed at the throat and then becomes supersonic downstream. When SPR is small, Fig. 3.14(a), some weak wave interactions are observed, and the flow still remains supersonic in most of the nozzle diverging section. As SPR increases, as shown in Fig. 3.14(b), complex wave interaction takes place. The main flow is blocked by the secondary jet and becomes supersonic only for a small region in the nozzle.

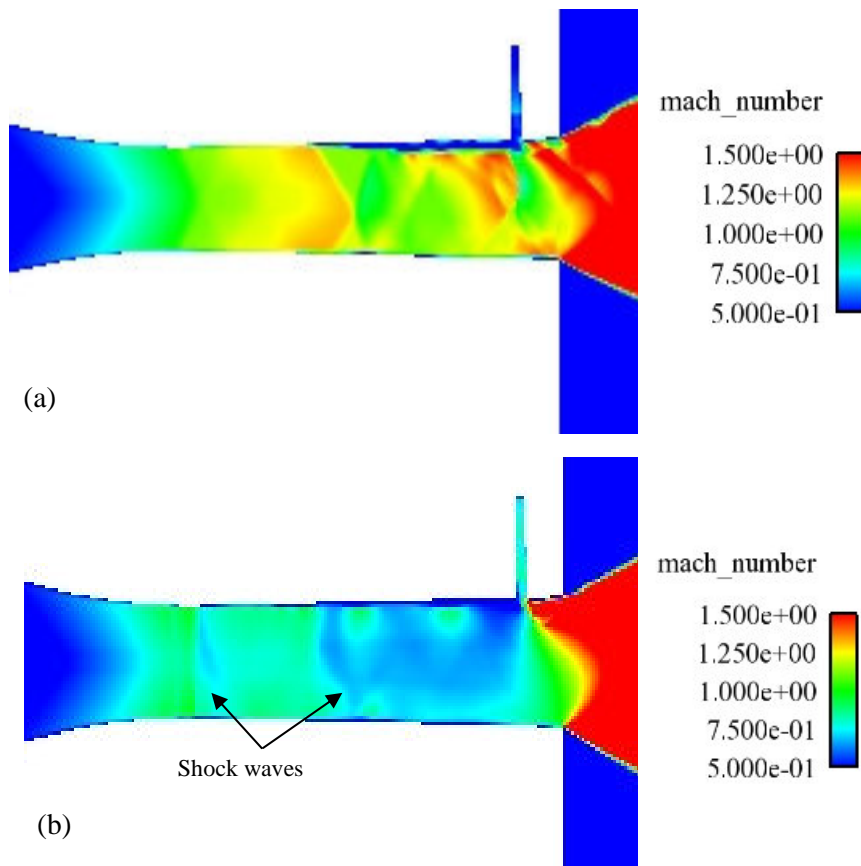


Figure 3.14 Mach number distribution in diverging nozzle section with NPR = 8 and (a) SPR=1 or (b) SPR=2.

Figures 3.15 and 3.16 show the Schlieren images of the cases with NPR=8 and $L_j = 5$ mm and 10 mm, respectively. With $SPR = 1$, the secondary jet is visible as a dark line starting from the secondary jet slot in both cases of $L_j = 5$ mm and 10 mm, Figs. 3.15(a) and 3.16(a). The oblique shock wave is not clearly in Fig. 3.15(a), but it is clearly seen to reflect at the opposite nozzle wall in Fig. 3.16(a) for $L_j = 10$ mm. With $SPR = 2$, the jet spreads extensively, and the flow upstream of the injection slot is affected over a much wider region than the case with $SPR = 1$. The extent of the region is almost the same in Figs. 3.15(b) and 3.16(b); i.e., the region is simply shifted by 5 mm.

Strong wave interactions take place in the diverging nozzle section. However, despite the strong effect of the secondary jet, the deflection of the exhaust gas does not increase with the SPR in the present nozzle. The secondary jet looks just choking the flow. Higher values of SPR not necessarily increase the flow deflection.

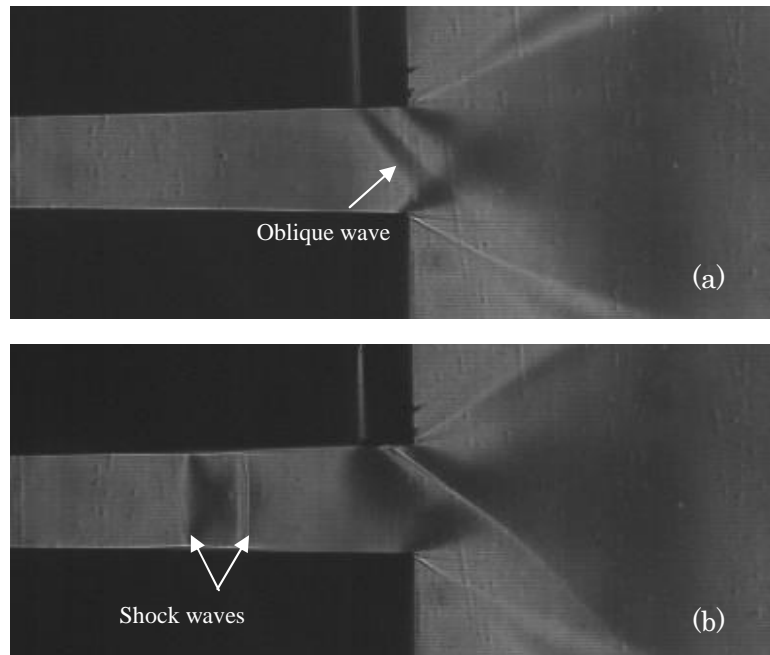


Figure 3.15 Schlieren images for $L_j = 5$ mm with $NPR = 8$ and (a) $SPR = 1$ or (b) $SPR = 2$.

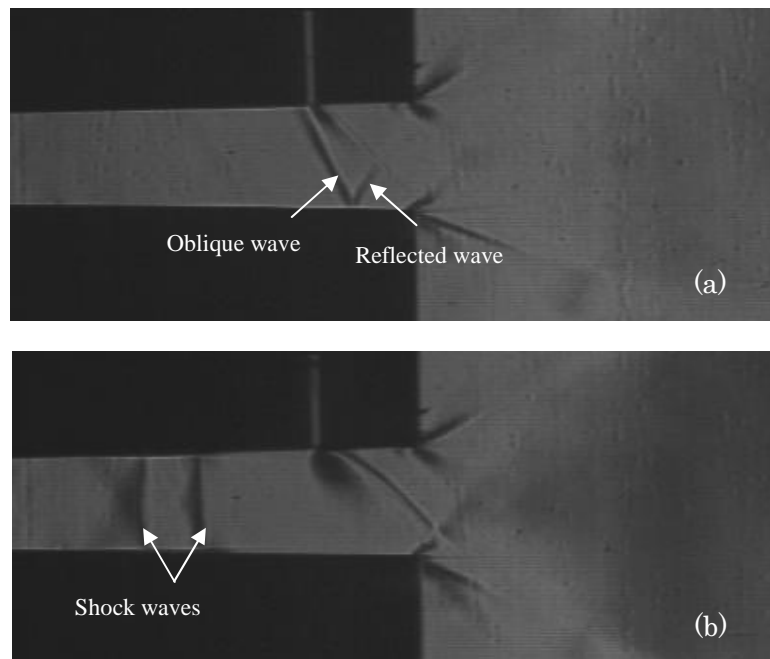


Figure 3.16 Schlieren images for $L_j = 10$ mm with $NPR = 8$ and (a) $SPR = 1$ or (b) $SPR = 2$.

On the basis of this observation, a new FTV nozzle is designed and manufactured. It has a relatively small injection slot so that the secondary jet does not block the main flow even with larger

values of SPR. It is expected that detailed investigations of the secondary jet effect will be possible with this new nozzle.

In order to evaluate the effect of the oblique shock wave on the flow deflection, Fig. 3.17 compares numerically obtained Mach number distributions beyond the nozzle exit for the cases with $L_j = 5$ mm and 10 mm with $SPR = 1$. As expected, the Mach number at the nozzle exit is close to the designed value of 1.5. It is difficult, however, to evaluate the thrust deflection angle from such flow images in the region downstream of the nozzle exit. In this study, therefore, a new method of evaluating flow diffractions by using thrust pitch moment induced from balance of pressure distributions on the nozzle wall.

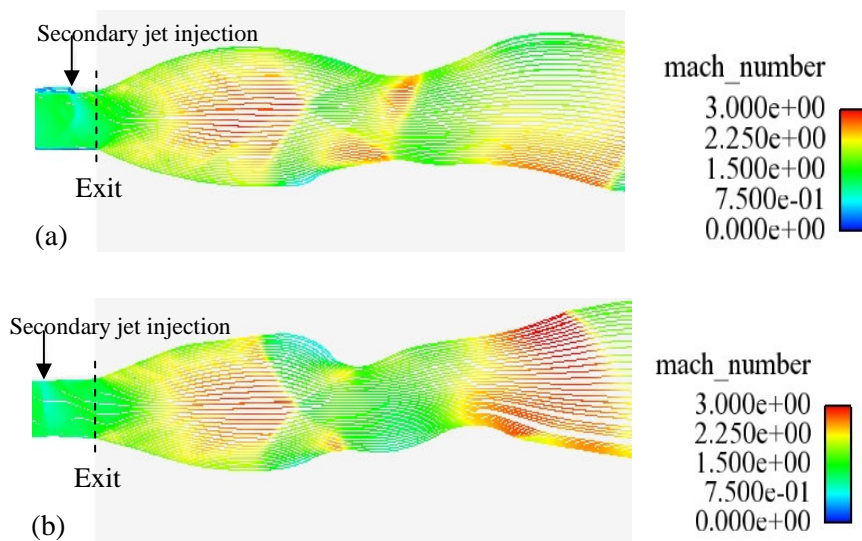


Figure 3.17 Mach number distribution and streamlines with $NPR = 8$ and $SPR = 1$ for (a) $L_j = 5$ mm or (b) $L_j = 10$ mm.

3.3.2.2 Static Pressures on Upper and Lower Nozzle Walls

Figures 3.18 and 3.19 show the numerical results for static pressure along the upper and lower nozzle walls for cases with $L_j = 5$ mm and 10 mm, respectively, with $NPR = 8$. For both $SPR = 1$ and 2, the pressure fluctuations shown in Fig. 3.18 is greater on the upper wall than on the lower wall. Additionally, the overall static pressure shown in Fig. 3.18(b) is higher than that shown in Fig. 3.18(a).

The static pressure on the upper wall is low in the region between the secondary jet slot and the nozzle exit. This is most prominent in Fig. 3.18(b) for $SPR = 2$, the pressure on the upper wall is decreased to 5000 Pa. This is because the gas in the region behind the secondary jet is sucked out to outside of the nozzle, while the main flow is blocked by the secondary jet. Hence, a low-pressure

region is formed near the wall downstream of the jet slot.

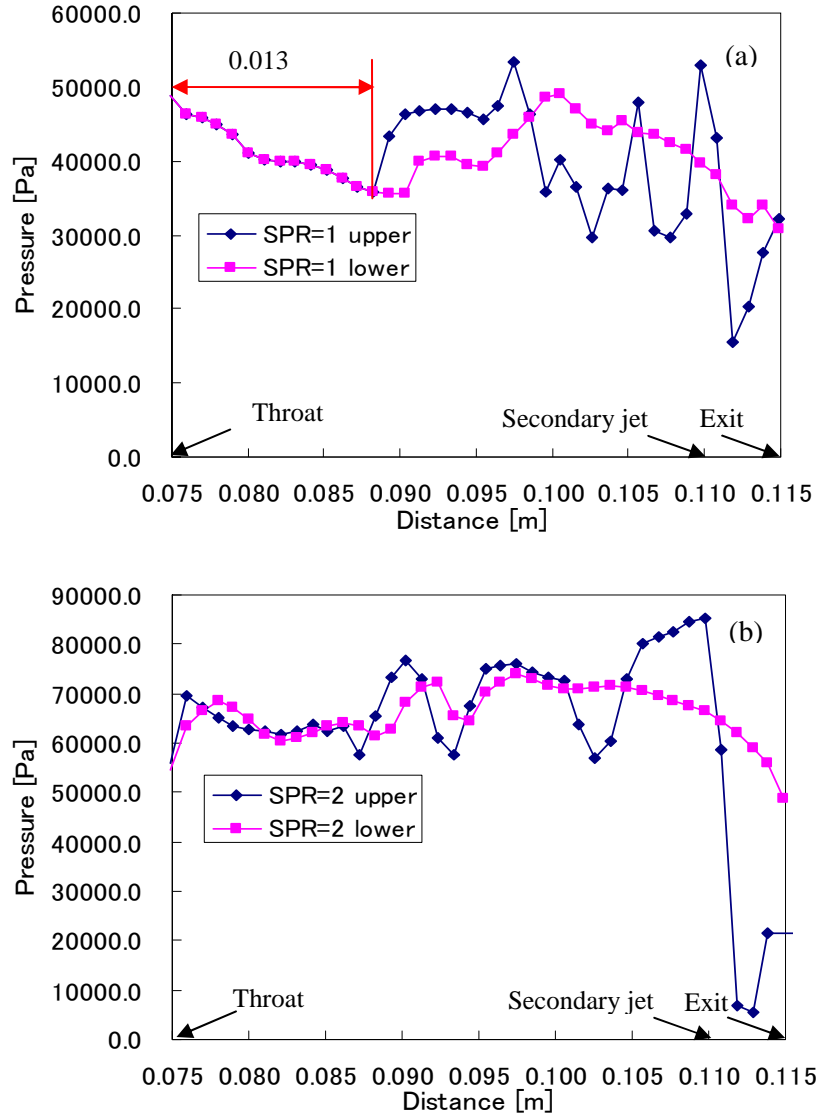


Figure 3.18 Wall pressure for $L_j = 5$ mm with $NPR = 8$ and (a) $SPR = 1$ or (b) $SPR = 2$.

For the cases with $SPR=1$, as seen in Figs. 3.18(a) and 3.19(a), the pressure distribution curves overlap with each other in the region close to the throat and the pressures are balanced between upper and lower walls. These are the supersonic regions that are unaffected by the secondary jet injection. The region extends approximately 13 mm from the throat for the case with $L_j = 5$ mm, as shown in Fig. 3.18(a), and approximately 8 mm from the throat for the case with $L_j = 10$ mm, as shown in Fig. 3.19(a).

As seen in Figs. 3.18(b) and 3.19(b) with $SPR = 2$, the pressure distributions on the upper and

lower nozzle walls are different throughout the entire region downstream of the nozzle throat. For the case of $SPR = 1$, the pressure on the upper and lower walls at the nozzle throat is around 0.05 MPa, which corresponds to the theoretical value of 0.528 times the atmospheric pressure for choking. However, for the case of $SPR = 2$, the pressure on the nozzle wall at the throat is higher than the theoretical value, indicating that the flow is not choked.

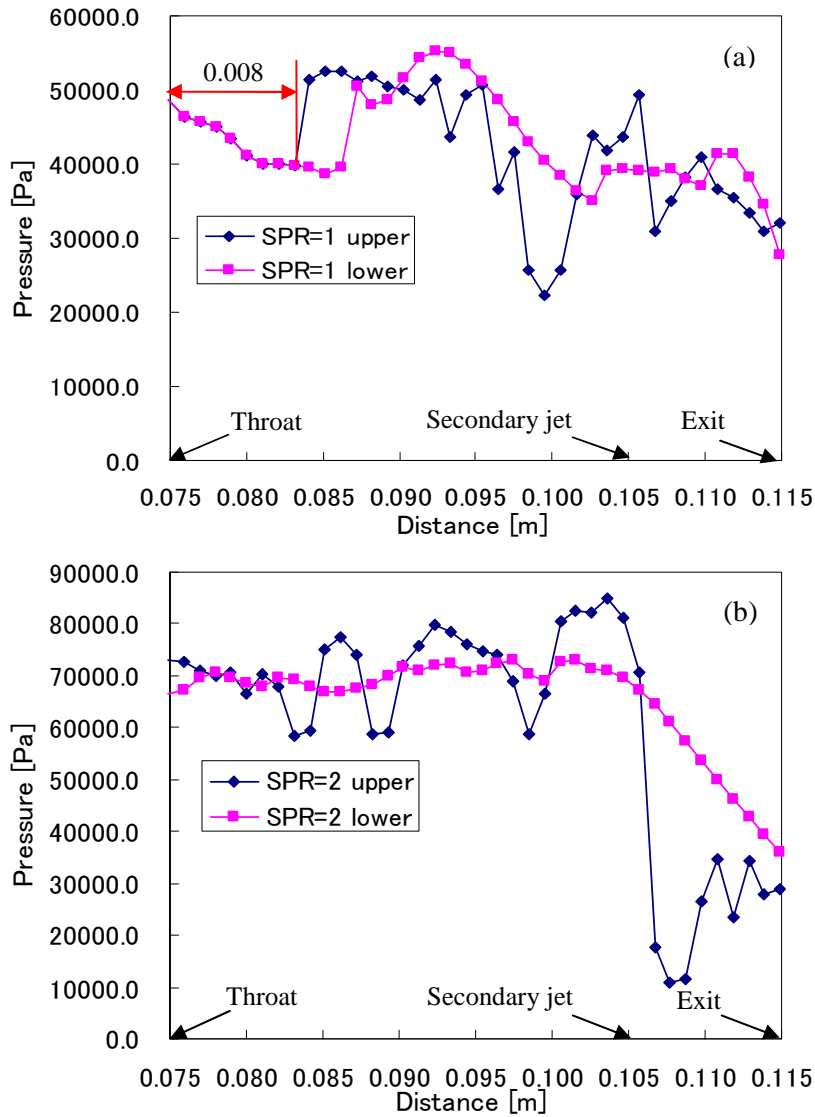


Figure 3.19 Wall pressure for $L_j = 10$ mm with $NPR = 8$ and (a) $SPR = 1$ or (b) $SPR = 2$.

3.3.2.3 Thrust Pitching Moment

The thrust pitching moment M_p of the nozzle is calculated by integrating the product of the pressure on the nozzle walls and the length from a specific pivot point to the pressure working point. The pivot

point was chosen arbitrarily at 0.075 m upstream of the throat, and the moment was plotted for different values of NPR ranging from 4 to 10, as shown in Fig. 3.20. The followings are thus observed:

- i) for a given L_j , M_p increases with the SPR;
- ii) for $SPR = 2$, M_p in $L_j = 10$ mm is greater than that in $L_j = 5$ mm, except at $NPR = 10$;
- iii) for $SPR=1$, the moments in the $L_j = 5$ mm and $L_j = 10$ mm are close, except at $NPR = 5$ and $NPR = 9$.

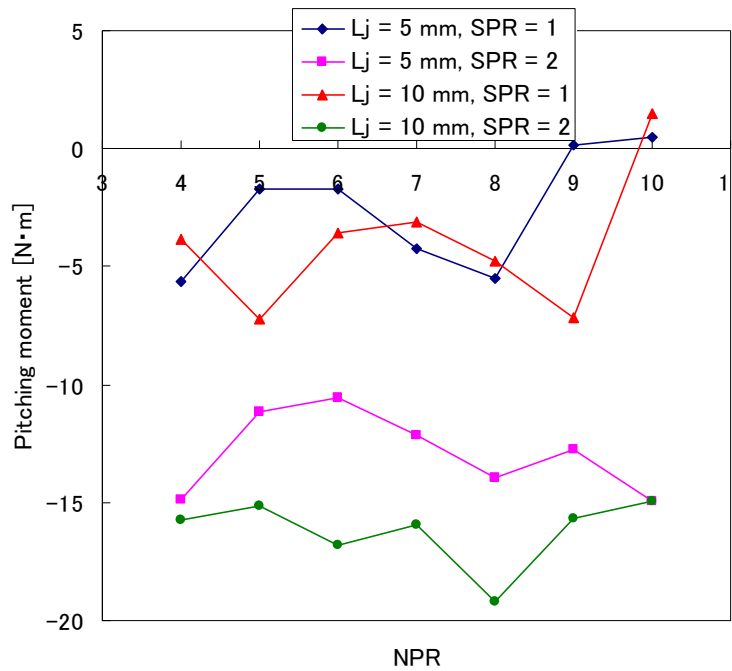


Figure 3.20 Thrust pitching moment.

Note that the moments are negative at most data points. It is positive at only three data points with large NPR values and with $SPR = 1$. In this study, a counterclockwise moment is defined as positive, so the strongly negative pitching moment is attributed to the low pressure on the upper wall between the secondary jet and the nozzle exit. In this area, the air flows outward due to the low back pressure outside the nozzle. At the same time, the gas in this area is entrained by the secondary jet and the pressure becomes noticeably low, as already shown in Fig. 3.20. Close to the nozzle exit, the pressure balance between the upper and lower walls makes the pitching moment to be negative.

With the current experimental setup, if M_p is only induced by the deflection of the exhaust gas, then a positive pitching moment is expected, since the exhaust gas is deflected downward by an oblique shock wave. Based on these findings in the present experiments, thrust vectoring from the effect of pressure balance is much stronger than that from the deflection of exhaust gas by an oblique shock wave. A series of experiments with a new nozzle configuration is now in preparation for an

investigation of the relative performance of the FTV owing to each of the aforementioned mechanisms based on the pitching moment production.

3.4 Summary

Numerical and experimental studies of fluidic thrust vectoring were carried out with a simple two-dimensional nozzle model.

It has been found difficult to evaluate the FTV performance quantitatively on the basis of the appearance of downstream flow patterns. In this study, the performance was instead evaluated from the thrust pitching moment.

In addition to the expected FTV mechanism owing to flow deflection by an oblique shock wave, a mechanism owing to the pressure difference in the vicinity of the nozzle exit was observed. The two mechanisms act in opposite directions, but the latter is much stronger for the nozzle that is used in this chapter.

The slot for the secondary jet injection is too large to the present setup, and the entire flow field downstream of the throat is affected by the jet even with a relatively low secondary jet pressure ratio; i.e., $SPR = 2$. In this study, the FTV mechanism attributed to flow deflection by an oblique shock is concealed by other complex wave interactions that are stronger. A new experimental model with a smaller secondary jet slot is now being constructed to study the details of the FTV mechanism and its performance. The numerical and experimental studies with the new nozzle model are described in the next chapter.

References

- [1] Li Li, HIROTA Mitsutomo and SAITO Tsutomu, Performance Prediction Fluidic Thrust Vectoring by Numerical Analysis, Symposium on Shock Waves, Tokyo, 2010.
- [2] 三輪武史, 李麗, 廣田光智, 齋藤務, 流体推力方向制御におけるノズル主流と二次噴射の干渉に関する研究, 平成21年度衝撃波シンポジウム, 東京, 2010.
- [3] L. Li, T.Saito and M. Hirota, Numerical and Experimental Predictions of Fluidic Thrust Vectoring Performance, the 7th International Conference on Flow Dynamics, Sandai, 2010.
- [4] J. L. Caton, M. E. Franke, Flow Visualization of Transient Phenomena in Wind Tunnels, Instrumentation Society of American Symposium, Denver, CO, May 1990.
- [5] Schlieren photography, <http://www.anfoworld.com/Schliere>.

Chapter 4 Studies with Improved Nozzle

In the preliminary studies described in the previous chapter, it was found difficult to evaluate the FTV performance quantitatively [1-3]. In order to study the details of the FTV mechanism and its performance, a new nozzle with appropriately designed secondary jet injection slot is constructed. In this chapter, the experimental and numerical studies with the improved nozzle will be described in detail. The experiments are performed with a nozzle pressure ratio (NPR) ranging from 3 to 10, the secondary pressure ratio (SPR) of 1, 2 or 3, and two different secondary jet locations. Numerical simulations of the nozzle flow are carried out by solving the Navier-Stokes equations, and the input parameters are set to match the experimental conditions. Computations are performed with and without the secondary jet injection for different combinations of NPR, SPR, and jet location. The influence of inclination angle of the secondary jet injection was also investigated.

4.1 Experimental Setup

The basic configuration of the experimental setup is almost the same shown in the previous chapter. The new nozzle is designed to rotate to adjust the exit spacing so that the flow Mach number at the nozzle exit is changed.

4.1.1 New Nozzle and Test Equipment

A photograph of the new nozzle and the experimental setup is shown in Fig. 4.1. The inlet of the nozzle is exposed to the atmosphere, whereas the outlet is connected to a vacuum tank. Pressure gauges and a Schlieren system are set for data collection.

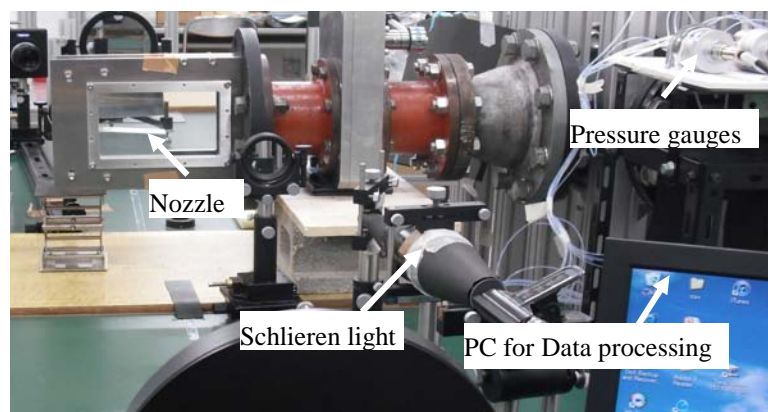


Figure 4.1 Sketch of experimental setup.

4.1.2 Structure of Nozzle

The nozzle is designed to rotate around the rotation shaft to adjust the exit spacing while keeping the throat spacing constant. The rotation shaft is set at 70 mm from of the nozzle throat. The expected flow Mach numbers at the nozzle exit ranges from 1.44 to 2.55. In order to get the flow Mach number of 2, the area ratio of the nozzle exit to the throat area is 1.69 according to an inviscid quasi-one-dimensional analysis.

The secondary jet injection slot on the upper nozzle wall has a width of 1 mm. Figure 4.2 shows the dimensions of nozzle without secondary jet injection slot adjusted to the flow Mach number of 2.

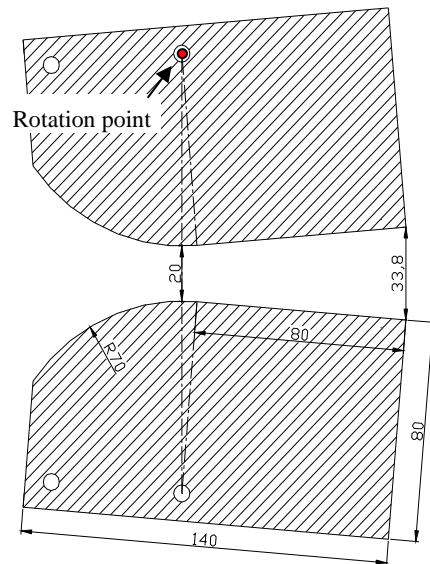


Figure 4.2 Dimensions of nozzle without secondary jet injection at Mach number of 2.

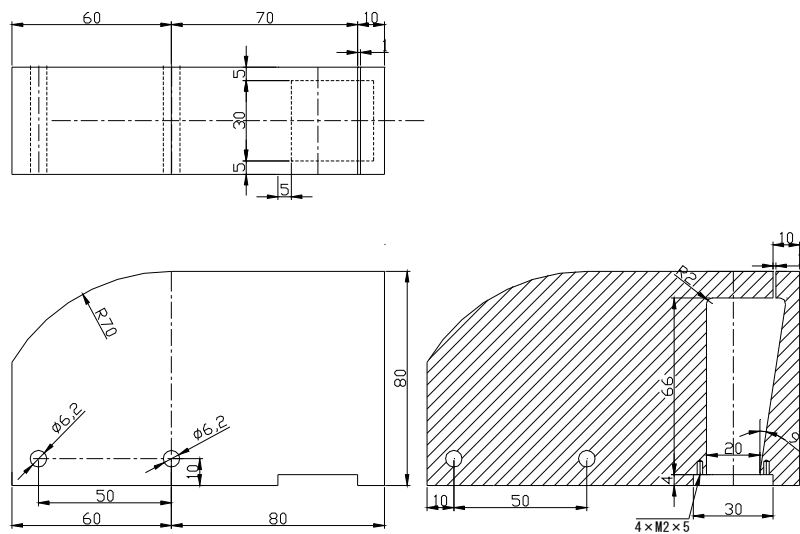


Figure 4.3 Dimensions of nozzle with secondary jet for $L_j = 10$ mm.

In this study, the distance between the secondary jet injection slot and the nozzle exit L_j is set to 5 mm and 10 mm. The dimensions of the nozzle with secondary jet injection for $L_j = 10$ mm are shown in Fig. 4.3.

4.1.3 Instrumentations

The static pressure probes are spaced every 10 mm starting at nozzle throat and extending to downstream of the nozzle exit along the nozzle centerline. The picture of the instrumentation for static pressure measurements is shown in Fig. 4.4.

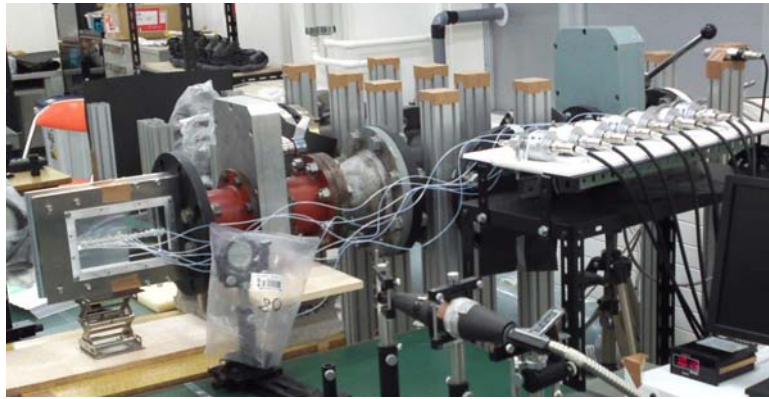


Figure 4.4 Photograph of static pressure measurement.

4.1.4 Flow Visualization

Flow visualization is carried out with the conventional Schlieren method.

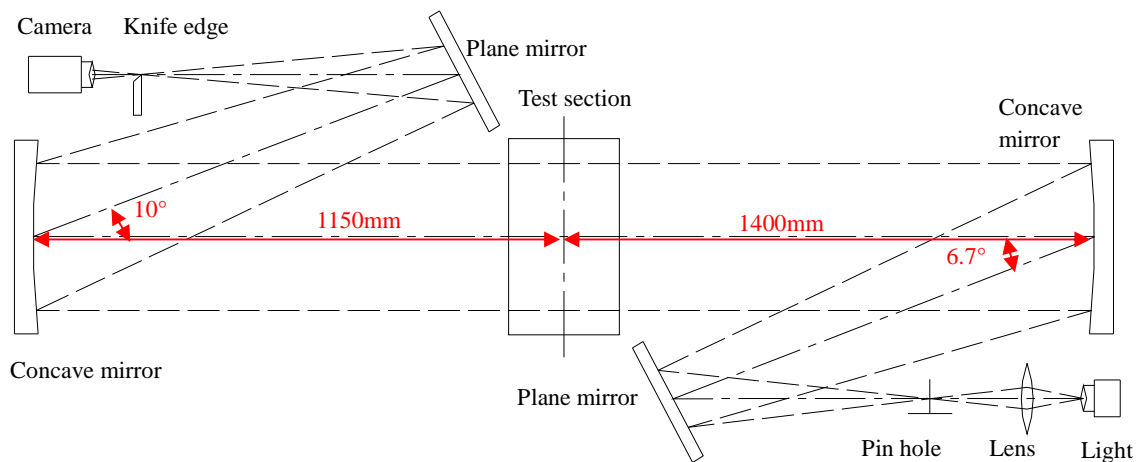


Figure 4.5 Schematic of the Schlieren system.

The distance between the mirrors is changed from the previous optical setup due to change in the nozzle dimensions. The Schlieren system is shown in Fig. 4.5. The distance between the concave mirror and the nozzle section is set to 1150 mm and 1400 mm. The angle of the reflected light by the plane mirror to the axis of the concave mirror is 6.7° , and the angle of reflected light by the concave mirror to the axis of the concave mirror is 10° . Nano-pulse NPL argon light is used for light source.

4.2 Numerical Simulations

The number of the grid cells allocated for the entire computational domain is about 450,000. The calculation time is approximately 12 hours to complete one case using 6 processing elements of Cray XD1. The region downstream of the nozzle exit extends 0.1 m along the x-axis, and the height of the region behind the nozzle exit is 0.16 m. Figure 4.6 shows the numerical grids near the diverging nozzle wall. The smallest grid near the wall is the order of magnitude of $10\ \mu\text{m}$.

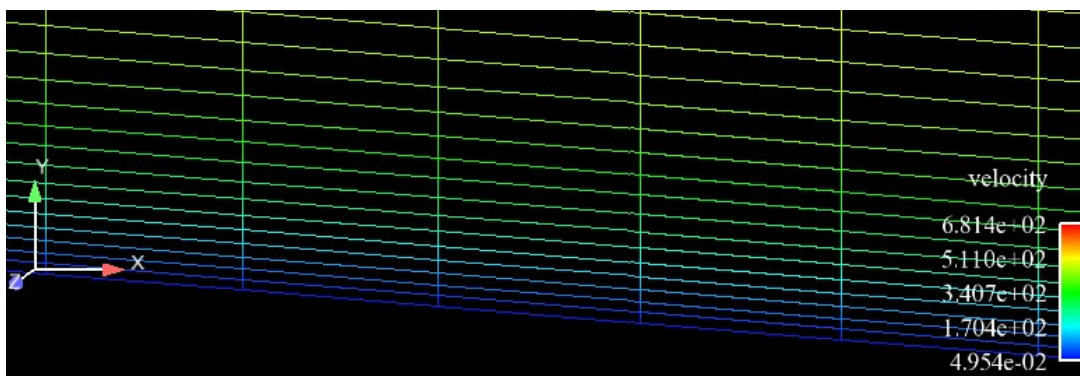


Figure 4.6 Grids near the nozzle wall.

4.3 Results and Discussion

The effects of FTV parameters such as NPR, SPR, L_j , and secondary angular injection β on the FTV performance are discussed. Presented and discussed first are the internal flow features, such as Mach number distribution, density distribution, and velocity vector distribution.

4.3.1 Effect of Different Values of NPR

In order to evaluate the effect of NPR, flows in the nozzle without secondary jet are investigated first. With the nozzle that is setup for the Mach number 2, the flows are over-expanded or under-expanded

depending on if the value of NPR is below or above 7.8. Figure 4.7 shows the flow field with $NPR = 3$ and $NPR = 9$. The flow is over-expanded at $NPR = 3$ with oblique shock waves downstream of the nozzle exits. Whereas, the flow is under-expanded at $NPR = 9$ with oblique expansion waves outside the nozzle exit. Near the nozzle throat, two clear oblique shocks are visible. In the upstream of the throat, wall surfaces are curved, while downstream of the point, the walls are straight. The waves are generated at the throat where the secondary derivatives of the upper and lower nozzle surfaces are discontinuous.

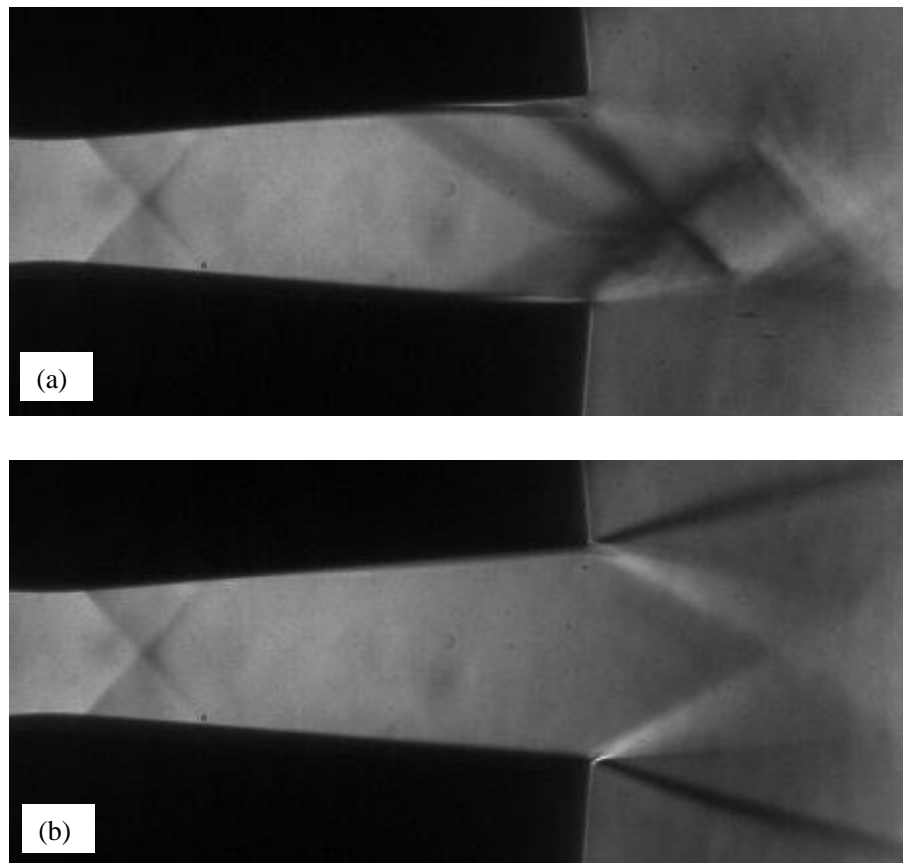


Figure 4.7 Schlieren images of different NPR and (a) $NPR = 3$ or (b) $NPR = 9$.

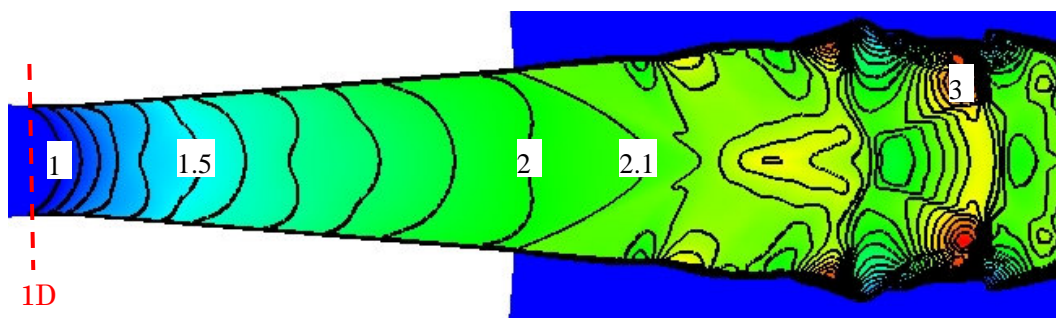


Figure 4.8 Mach number distribution in the nozzle diverging part with $NPR = 9$.

Numerically obtained Mach number distribution with $NPR = 9$ is shown in Fig. 4.8. The Mach number in the nozzle diverging part increases from 1 to 2. The Mach number of two-dimensional (2-D) numerical results at the nozzle throat is not the same as the one-dimensional (1-D) theory. For the 1D theory, the Mach line is a straight line at the throat with Mach number of 1 while for the 2-D numerical method, the Mach line is an arch. In addition, the Mach number of 2-D at the nozzle exit is close to the designed value of 2. It is seen that the Mach number reaches 3 at a small regions downstream of the nozzle exit.

4.3.2 Effect of Different Values of SPR

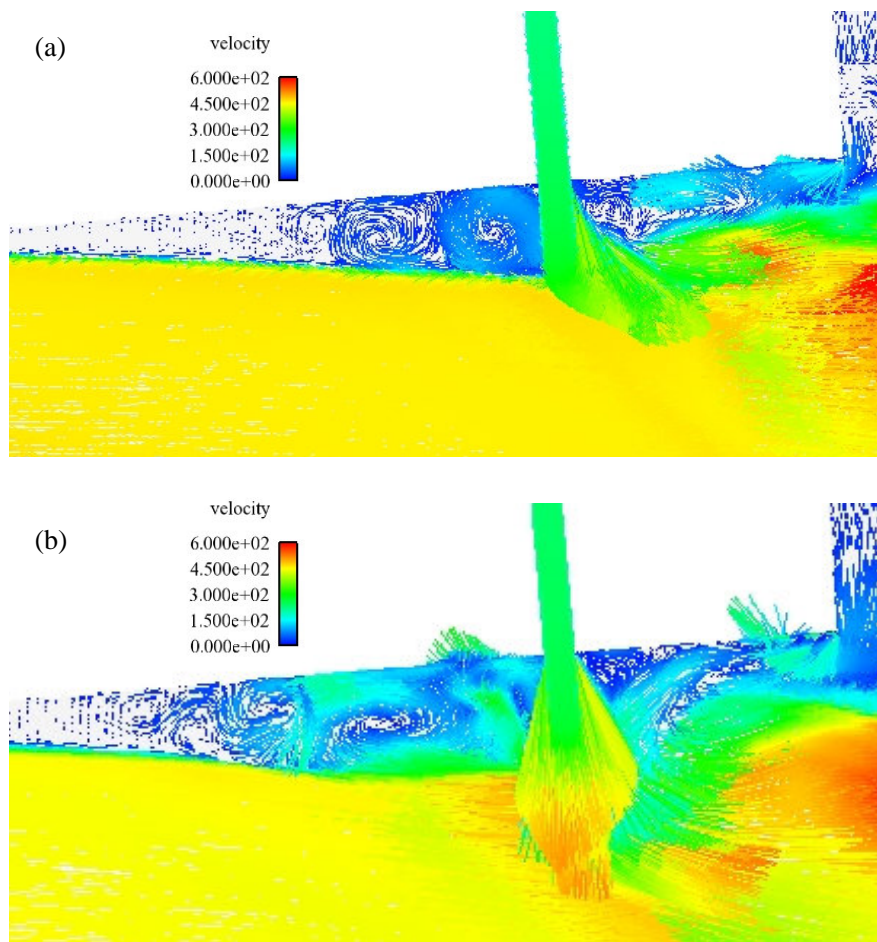


Figure 4.9 Velocity vector distribution near the secondary jet injection with $NPR = 9$ and (a) $SPR = 1$ or (b) $SPR = 2$.

When the SPR is 1, the mass flow ratio of the secondary jet injection to the main flow is 5 %, and

when the SPR is 2 and 3, the mass flow ratio is 10% and 15%, respectively. In the region upstream of the secondary injection, the boundary layer is separated due to the secondary jet injection. Figure 4.9 shows the velocity vectors near the secondary jet in the diverging section of the nozzle with $NPR = 9$ and $SPR = 1$ or $SPR = 2$. As shown in Fig. 4.9(a), with a smaller value of SPR, the velocity of the flow upstream the secondary jet near the wall and domain of vortices are small. As shown in Fig. 4.9(b), as the SPR increases, the vortices are strong and the range of vortices is larger.

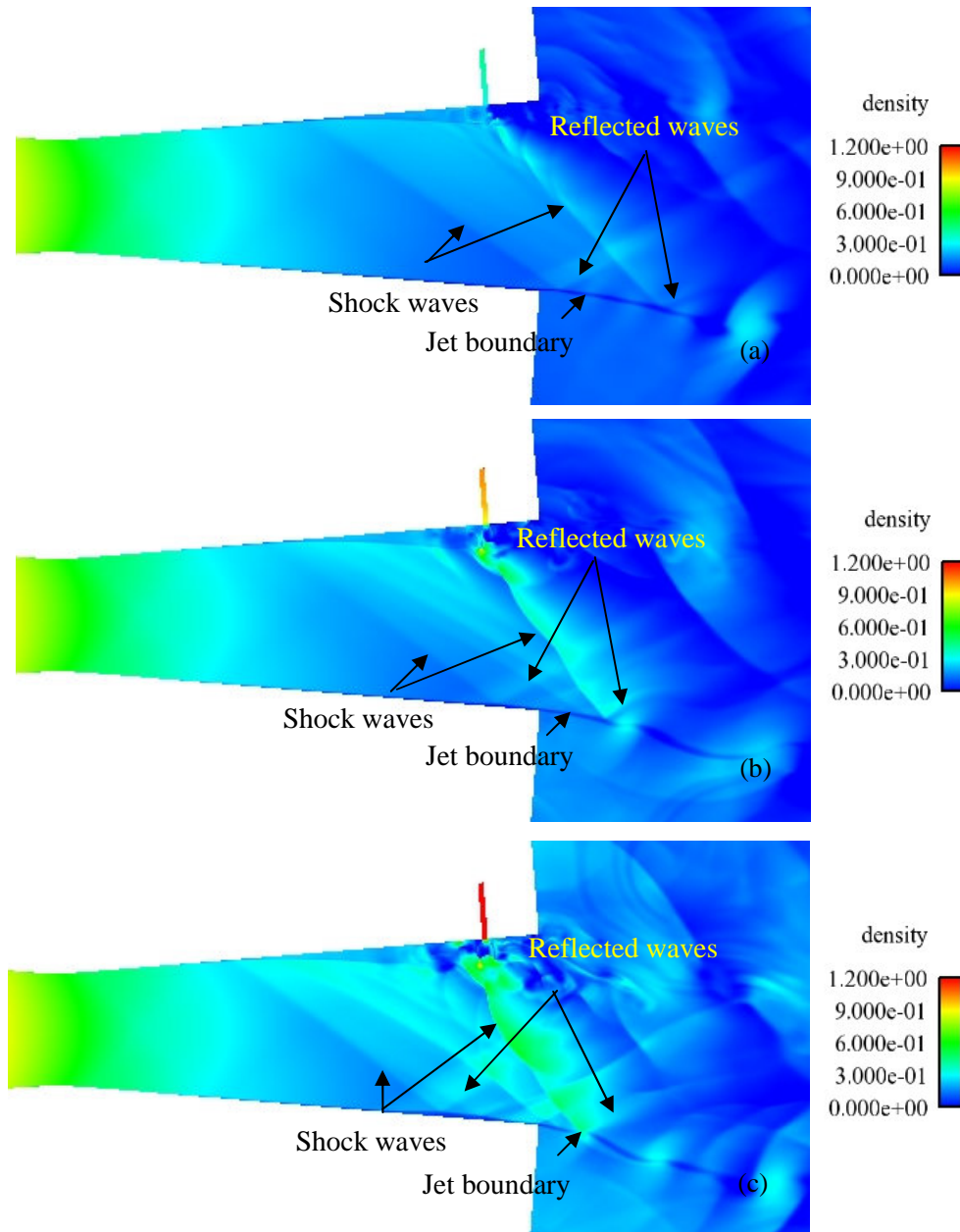


Figure 4.10 Density distribution in the nozzle diverging part with $NPR=9$ and (a) $SPR = 1$ or (b) $SPR = 2$ or (c) $SPR = 3$.

Figure 4.10 shows the density distributions for $L_j = 10$ mm with $NPR = 9$ and $SPR = 1, 2$ or 3 . As shown in the figure, notable shock waves are observed at the upstream of the secondary jet slot and the shock waves are reflected at the jet boundary. The flow separation is also seen upstream of the secondary jet. As shown in Fig. 4.10(a), in the case of $SPR = 1$, a weak shock wave far from the secondary jet and a strong shock wave upstream of the secondary jet are seen. As shown in Fig. 4.10(b), as SPR increases, the shock waves become stronger and, upstream the secondary jet, some weak shock waves also appear. As shown in Fig. 4.10(c), as SPR is increased further, the shock waves become stronger, and the domain of flow separation also becomes bigger due to the strong secondary injection.

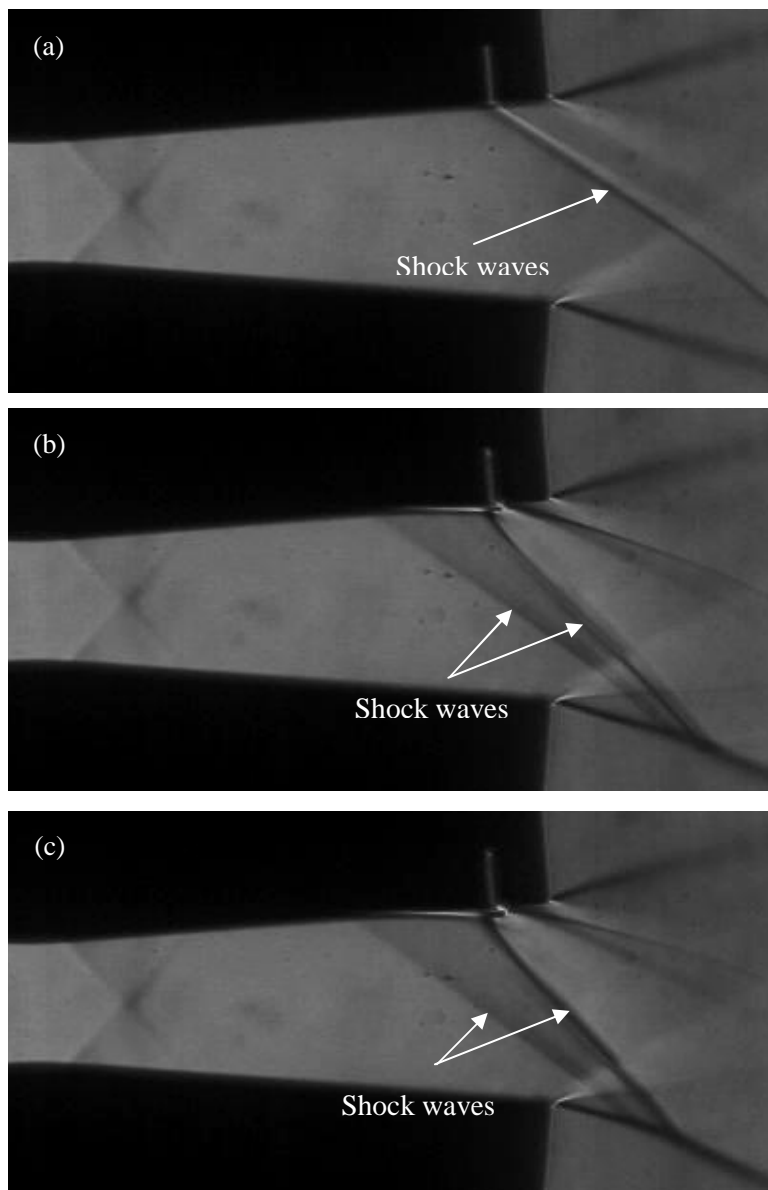
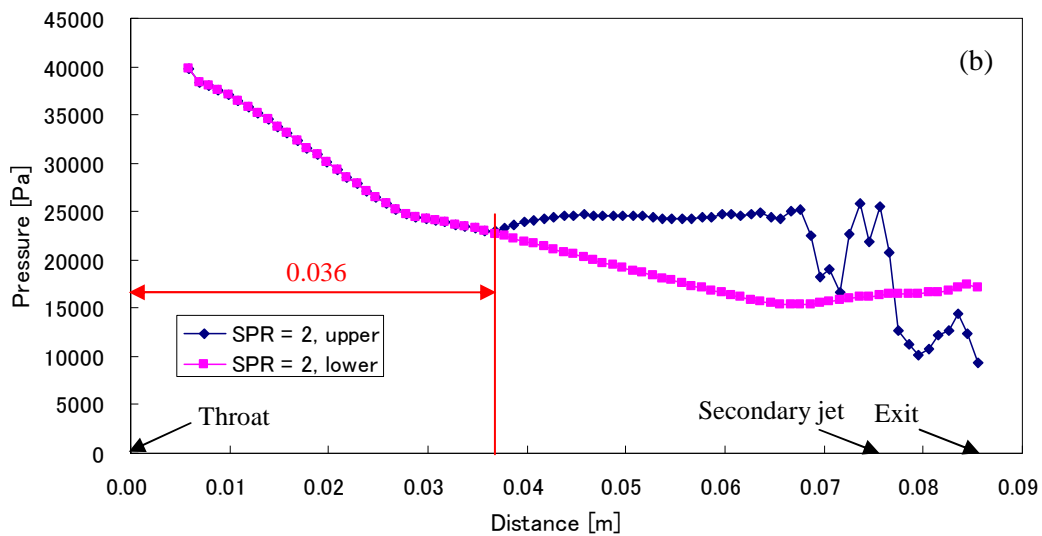
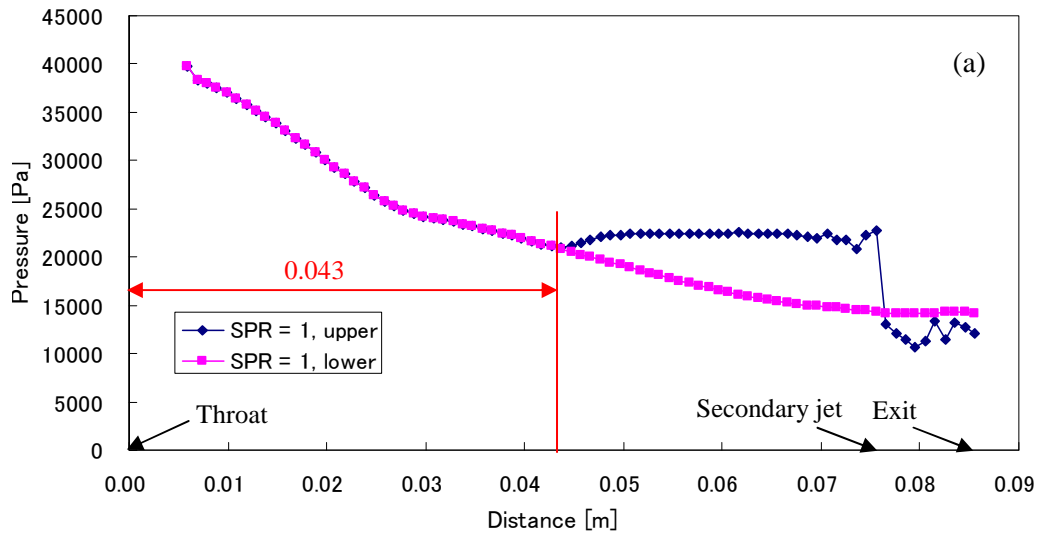


Figure 4.11 Schlieren images for $L_j = 10$ mm with $NPR = 9$ and (a) $SPR = 1$ or (b) $SPR = 2$ (c) $SPR = 3$.

Figure 4.11 shows the Schlieren images for $L_j = 10$ mm with $NPR = 9$ and $SPR = 1, 2$ or 3 . As shown in the figure, notable shock waves are observed at the upstream of the secondary jet slot and the separation domain is also observed upstream of the secondary jet. With $SPR = 1$, the secondary jet is visible as a bright line starting from the secondary jet slot, as seen in Fig. 4.11(a). With $SPR = 2$ as seen in Fig. 4.11(b), the jet spreads extensively and the flow upstream of the injection slot is affected over a much wider region than that with $SPR = 1$. As SPR increases, the jet continues to spread, and the separation domain near the wall upstream the jet also becomes larger as shown in Fig. 4.11(c). Even with $SPR = 3$, the shock wave induced by the secondary jet does not hit the other wall, unlike the cases with large values of SPR with the previous nozzle. It is found that the basic flow patterns are the same with $L_j = 5$ mm.



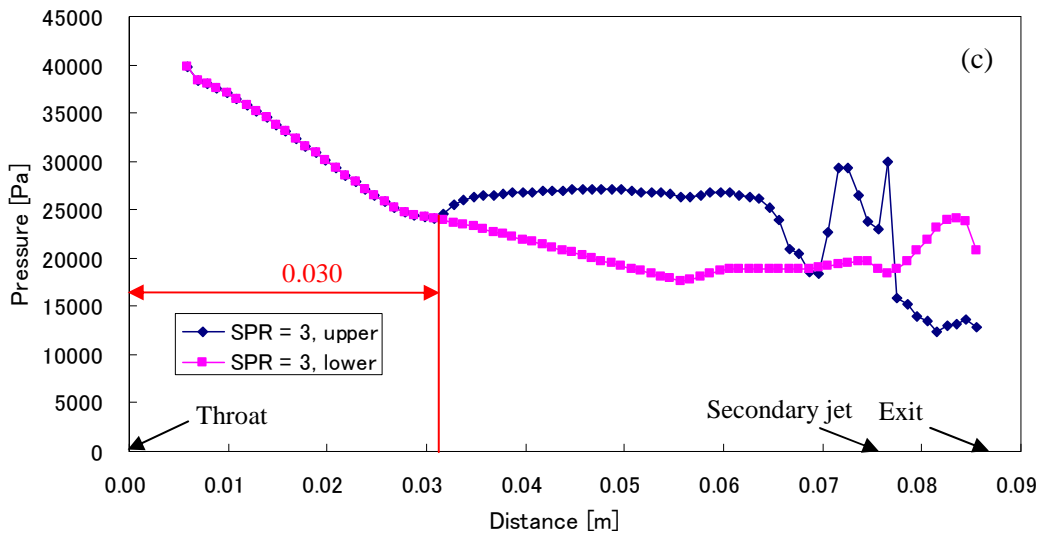


Figure 4.12 Wall pressure for $L_j = 10$ mm with $NPR = 9$ and (a) $SPR = 1$ or (b) $SPR = 2$ or (c) $SPR = 3$.

Figure 4.12 shows the numerical results for static pressure along the upper and lower nozzle diverging walls for $L_j = 10$ mm with $NPR = 9$. In all figures, the pressure fluctuation is greater on the upper wall. The static pressure on the upper wall is low between the secondary jet slot and the nozzle exit. It is also seen that the pressure distribution curves overlap with each other for a region close to the throat where the flow is supersonic and unaffected by the secondary jet injection. Comparing Fig. 4.12(a), (b), and (c), it is also found that, the length of the overlap region is 0.043 m with $SPR = 1$, and is 0.036 m with $SPR = 2$, and then is 0.030 m with $SPR = 3$. That is to say, the overlap region becomes smaller as the SPR increases since the effect of the secondary injection becomes stronger. Even for $SPR = 3$, however, shown in Fig. 4.12(c), the effect of secondary jet injection does not reach the throat. Note that, in the previous nozzle, whole region in the nozzle was affected by the secondary jet injection when $SPR = 2$.

4.3.3 Effect of Different Values of L_j

Figure 4.13 shows the flow Mach number distribution with $NPR = 9$ and $SPR = 1$ for different values of $L_j = 2, 8, 40$ and 80 mm. The boundary layer of the main flow is separated upstream of the secondary jet due to the adverse pressure gradient, and the oblique shock and the range of the separation decreases as the L_j becomes larger. In the case of secondary jet injection being placed at the nozzle throat, there are no obvious interaction between the secondary injection and the primary flow. As the location of the secondary jet injection is moved to the throat, the induced oblique shock wave reflects at the opposite nozzle wall even for $SPR = 1$, as shown in Fig. 4.13(c). It is also seen

that the deflection of the primary flow at the nozzle exit becomes small.

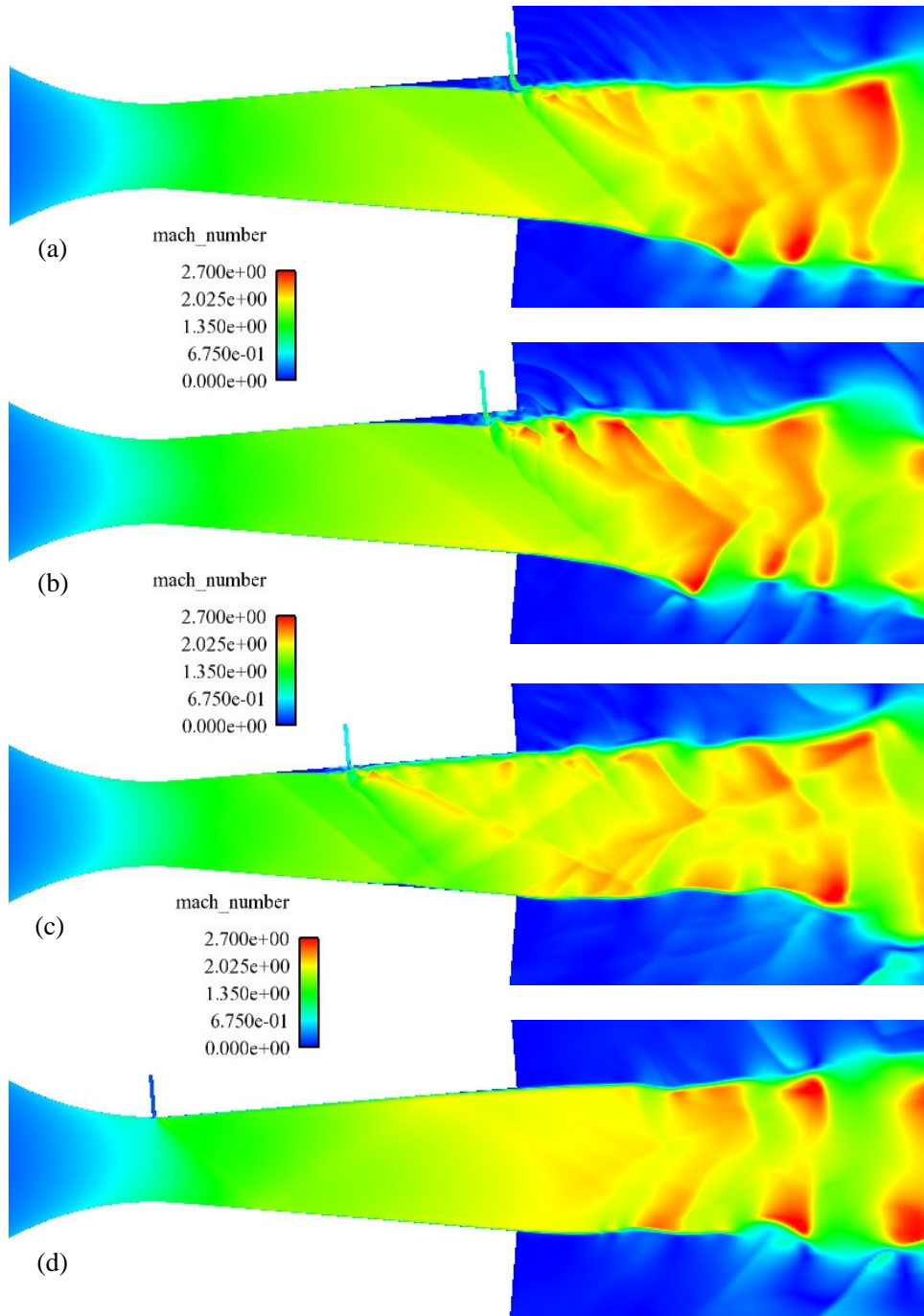


Figure 4.13 Mach number distribution with NPR = 9 and SPR=1 and (a) $L_j = 2$ mm or (b) $L_j = 8$ mm or (c) $L_j = 40$ mm or (c) $L_j = 80$ mm.

4.3.4 Effect of Different Values of β

The effect of secondary jet injection angle is investigated by defining the angular injection angle β as in Figure 4.14. The angle is positive when it is measured counterclockwise from the vertical axis and $\beta = 4.7^\circ$ when the jet is normal to the nozzle wall.

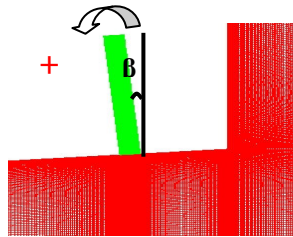


Figure 4.14 Illustration of secondary angular injection.

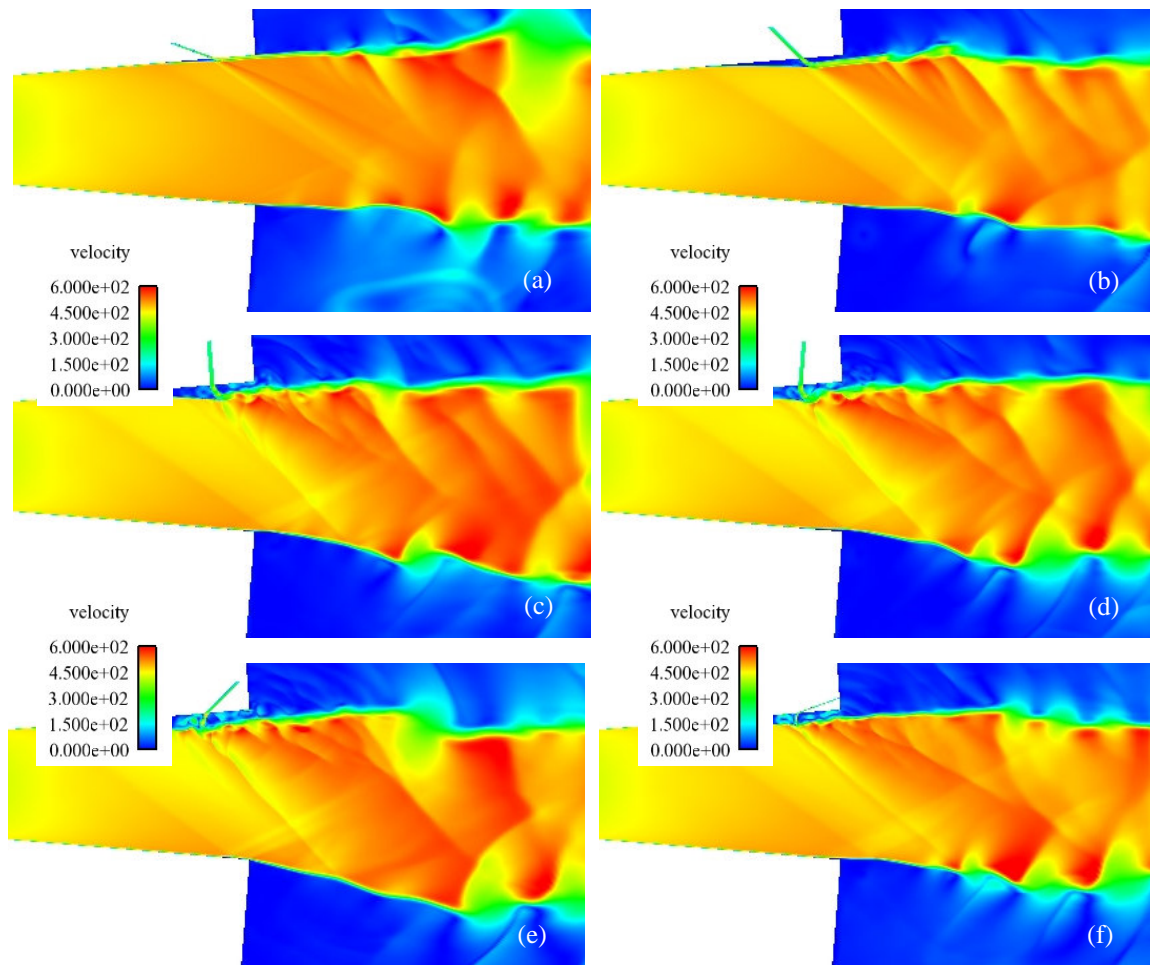


Figure 4.15 Velocity distribution with NPR = 9 and SPR = 1

and (a) $\beta = 70$ or (b) $\beta = 45$ or (c) $\beta = 4.7$ or (d) $\beta = -4.7$ or (e) $\beta = -45$ or (f) $\beta = -70$.

Figure 4.15 shows the velocity distribution with $NPR = 9$ and $SPR = 1$ for different β . There are two shock waves upstream the secondary injection. The shock waves become strong with small β as shown in Figs. 4.15(c) and (d). When β is positive, as β increases, the chance of oblique shock waves impingement on the opposite wall becomes small, shown in Figs. 4.15(a) and 4.15(b). While when β is decreases, the range of separation upstream the secondary jet becomes larger, Figs. 4.15(a), (b) and (c). Comparing Figs. 4.15(a) and 4.15(f), Figs. 4.15(b) and 4.15(e), and Figs. 4.15(c) and 4.15(d), it is found that the range of separation domain caused by the negative β is larger than that caused by positive β .

4.4 Summary

Numerical and experimental studies of fluidic thrust vectoring were carried out with an improved two-dimensional nozzle model with a relative small secondary jet slot.

The effects of FTV parameters such as NPR , SPR , L_j , and secondary angular injection β on the FTV performance are discussed.

The different NPR causes the different flow pattern downstream the nozzle exit with oblique shock waves or oblique expansion waves. The Mach number of 2-D at the nozzle exit is close to the designed value of 2.

With the injection of secondary jet, notable shock waves are observed at the upstream of the secondary jet slot and the shock waves are reflected at the jet boundary. The flow separation is also seen upstream of the secondary jet. As SPR is increased further, the shock waves become stronger, and the domain of flow separation also becomes larger. Even with $SPR = 3$, the shock wave induced by the secondary jet does not hit the other wall, unlike the cases with large values of SPR with the previous nozzle.

As the L_j becomes larger, the oblique shock and the range of the separation decreases, and the boundary layer of the main flow is separated upstream of the secondary jet due to the adverse pressure gradient. As the location of the secondary jet injection is moved to the throat, the induced oblique shock wave reflects at the opposite nozzle wall even with small SPR . It is also seen that the deflection of the primary flow at the nozzle exit becomes small.

The secondary angular injection angle β is positive when it is measured counterclockwise from the vertical axis. The range of separation domain caused by the negative β is larger than that caused by positive β . When β is positive, as β increases, the chance of oblique shock waves impingement on the opposite wall becomes small.

References

- [1] Li Li, Mitsutomo HIROTA and Tsutomu SAITO, Performance Predictions of Fluidic Thrust Vectoring by Numerical and Experimental Studies, Symposium on Shock Waves, Tokyo, 2011.
- [2] L. Li, M. Hirota, and T. Saito, Numerical and Experimental Studies of Fluidic Thrust Vectoring, 28th International Symposium on Shock Waves, UK, 2011.
- [3] Li Li, Tsutomu Saito, Numerical and Experimental Investigations of Fluidic Thrust Vectoring Mechanism, International Journal of Aerospace Innovations, UK, 2011.

Chapter 5 Evaluations of FTV Performance

With the preliminary nozzle, the pitching moment induced from the pressure distributions on the nozzle walls has the opposite effect in the thrust vectoring compared to that of expected oblique-shock FTV mechanism. With the new nozzle, the pitching moment has the same effect with the expected FTV mechanism. The relation between thrust pitching moment and exhaust gas deflection angle is discussed in this chapter.

5.1 The Method for Evaluating FTV Performance

The thrust pitching moment and the thrust pitching angle are chosen to evaluate the FTV performance, and methods for evaluating them are investigated in detail. The effect of pivoting points in the moment evaluation is also discussed.

5.1.1 Thrust Pitching Angle and Thrust Pitching Moment

The FTV performance is evaluated by thrust pitching angle δ_p [1-5].

$$\delta_p = \tan^{-1} \frac{F_N}{F_A}, \quad (5-1)$$

$$F_N = \sum (\rho u v) \cdot \Delta A, \quad (5-2)$$

$$F_A = \sum \{ \rho u^2 + (p - p_\infty) \} \cdot \Delta A, \quad (5-3)$$

where F_A and F_N are the x and y components of momentum, ρ and ΔA are density and cell area, u and v are the x and y components of velocity, and p and p_∞ are the static pressure and back pressure of cells at the x direction.

The thrust pitching moment M_p of the nozzle is calculated by integrating the product of the pressure on the nozzle walls and the length from a specific pivot point to the pressure working point,

$$M_p = \sum (F_w \cdot l), \quad (5-4)$$

where l is the length from the working point to the pivot point and F_w is the working pressure.

5.1.2 Evaluation of Thrust Pitching Angle at the Different Location

Although most of the FTV researches use the thrust pitching angle to evaluate the FTV performance, there is not detailed description of the evaluation method. Table 5.1 shows the thrust pitching angle δ_p at different locations on the centerline downstream the nozzle exit for $L_j = 4$ mm with $NPR = 9$

and $SPR = 2$ of the new nozzle. There are 238 grid points in the computational domain downstream of the nozzle exit. As seen in this table, the angle becomes smaller as the measuring point moves far away from the nozzle exit. There is no standard authority assessment location of the pitching angle and the pitching angle also changes with time. In this study, the pitching angle is evaluated at the nozzle exit and the average value of the stable state is taken.

Table 5.1 Thrust pitching angle at different mesh number.

Mesh number downstream the nozzle exit	0	100	150	220
Thrust pitching angle δ_p	8	7.76	2.97	-1.43

5.1.3 Different Pivot Points Chosen to Evaluate the Thrust Pitching Moment

Figure 5.1 shows the thrust pitching moment M_p with different NPR of the preliminary nozzle. The pivot point is chosen at the nozzle throat, and the average value of the moment with the stable state is taken. Comparing the results with the pivot point at the nozzle inlet shown in Fig. 3.20, it is seen that the tendency is almost the same. Therefore, the pivot point can be chosen arbitrarily without affecting the characteristics of the thrust pitching moment.

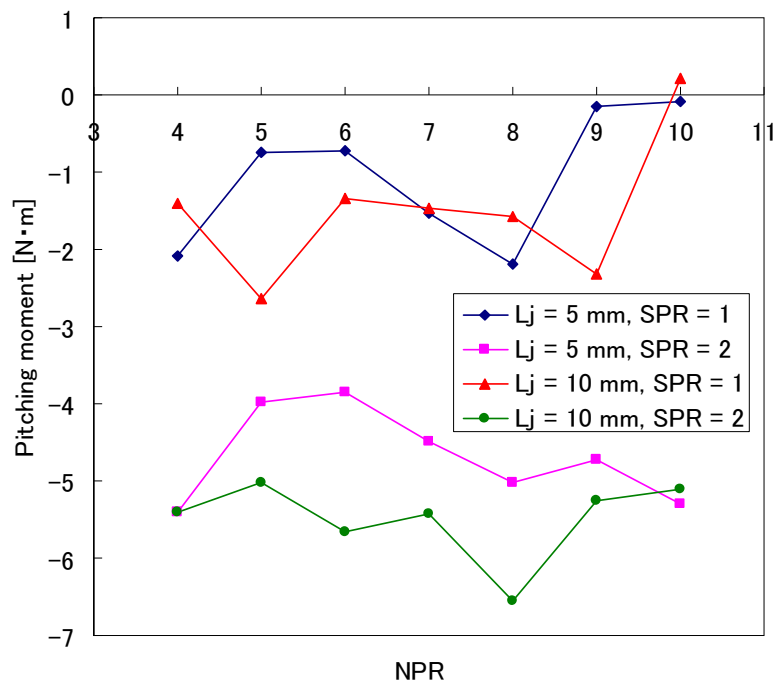


Figure 5.1 Thrust pitching moment with different values of NPR (pivot point is at throat).

5.2 Effects of the FTV Parameters on FTV Performance

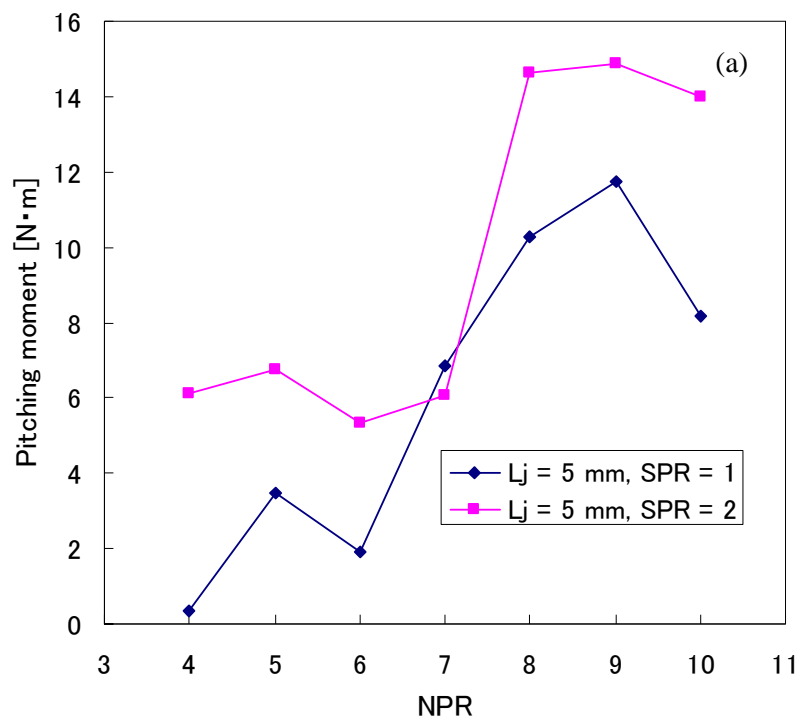
The effects of FTV parameters, which include NPR, SPR, secondary jet location L_j and secondary angular injection β , on FTV performance are discussed.

5.2.1 Effect of NPR

As mentioned in the preliminary experiment, the counterclockwise moment is defined as positive, and the thrust pitching moment is negative. The negative pitching moment is attributed to the effect of pressure balance stronger than that the oblique shock wave, shown in Figs. 3.20 and 5.1.

Based on these findings in the preliminary experiment, the moment of the new experimental nozzle with a smaller secondary jet slot is investigated as follows. The pivot point for evaluating the pitching moment M_p is chosen at the throat. The pitching moment M_p is plotted for different NPR ranging from 4 to 10, as shown in Fig.5.2.

Most of the moments are positive as expected as the effect of the oblique shock wave FTV mechanism expect at $NPR = 5$ and $SPR = 1$ for $L_j = 10$ mm, shown in Fig. 5.2(b). Most of the moments with $SPR = 2$ are bigger than that with $SPR = 1$. For $L_j = 5$ mm, the moments of $SPR = 2$ are bigger than that of $SPR = 1$ except at $NPR = 7$, shown in Fig. 5.2(a). For $L_j = 10$ mm, the moments of $SPR = 2$ are bigger than that of $SPR = 1$ except at $NPR = 8$, shown in Fig. 5.2(b). Comparing the Fig. 5.2(a) with 5.2(b), for $SPR = 1$, the curves have the same tendency with $L_j = 5$ and 10 mm, except at $NPR = 4$ and $NPR = 5$.



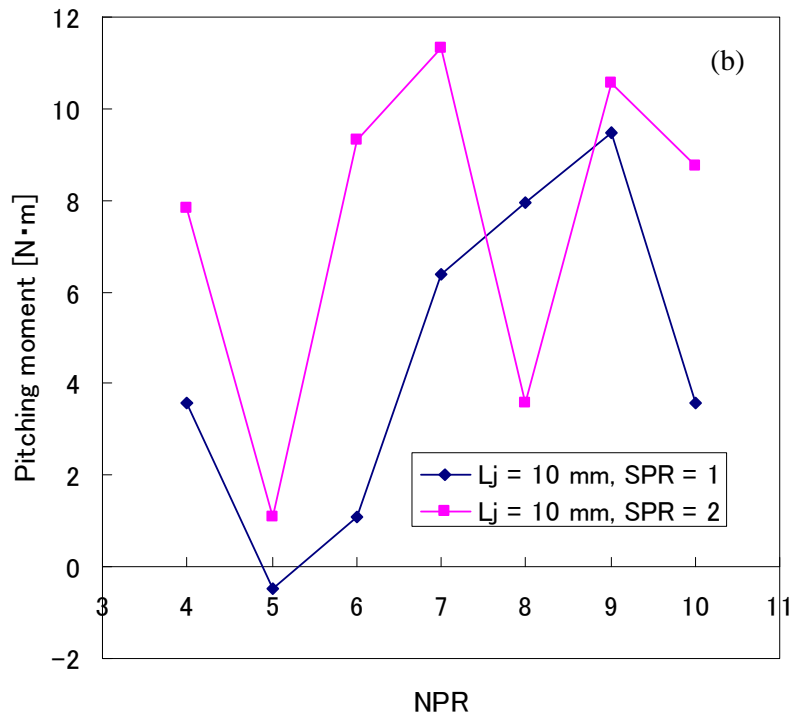
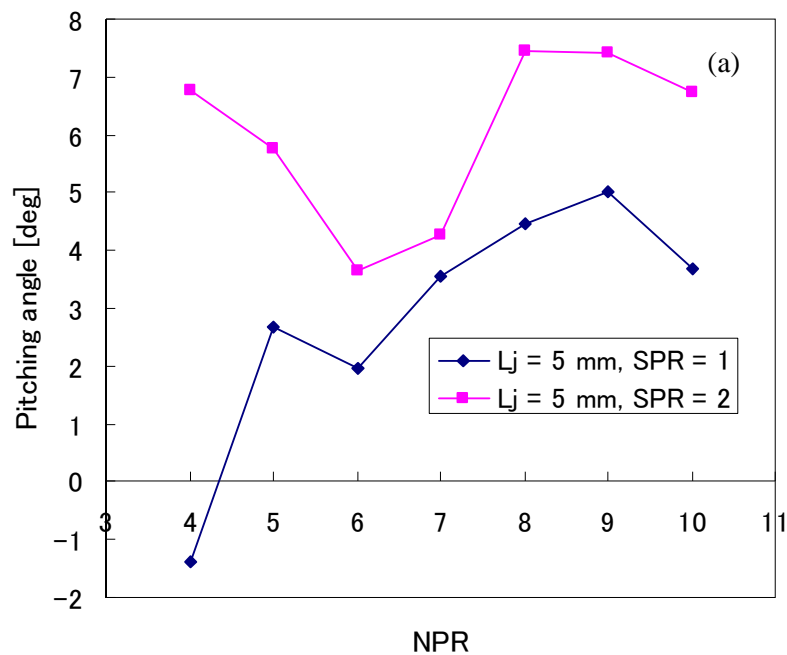


Figure 5.2 Thrust pitching moment with different NPR and (a) $L_j = 5$ mm or (b) $L_j = 10$ mm.

Note that the thrust pitching moment is positive at most data points. The counterclockwise moment is defined as positive and is expected to be positive if it is only deflected downward by an oblique shock wave. This is opposite to the case of negative moment attributed to the low pressure on the upper wall between the secondary jet and the nozzle exit, as mentioned in Section 3.3.2.3.



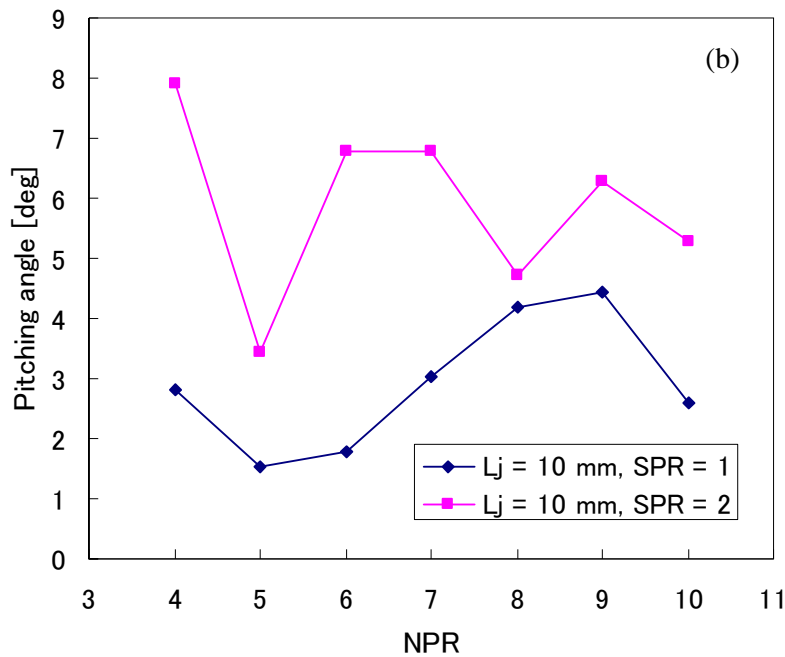


Figure 5.3 Thrust pitching angle with different NPR and (a) $L_j = 5$ mm or (b) $L_j = 10$ mm.

On the basis of the preliminary experiment, the flow downstream of the nozzle vibrates slightly from the horizontal direction, that is to say, the deflection angle of the flow is small and near to zero for the stronger effect of the pressure balance than the oblique shock wave.

Based on these findings in the preliminary experiment, the thrust pitching angle of the new experimental nozzle is discussed as follows.

The thrust pitching angle δ_p is plotted for different NPR ranging from 4 to 10, as shown in Fig.5.3. It is observed that: a) tendency of the angle is the same as the moment, except at NPR = 4 and SPR = 2 for $L_j = 5$ mm, and NPR = 7 and SPR = 2 for $L_j = 10$ mm; b) the deflection angle is larger for the high value of SPR.

A method using force-moment balance to evaluate the FTV effect and a common procedure for utilizing the ratio of the radial to the axial momentums of exhaust gas has been introduced. The relation between the thrust pitching moment and pitching angle is investigated with the linear approximation and shown in Fig.5.4. The regression equation y and coefficient of determination R^2 of the trend line are gotten. The nearer of the R^2 to 1, the fitter is the regression equation. The regression equations show that the larger of the moment, the larger is the deflection angle. The coefficients of determination of $L_j = 5$ mm are higher than that of $L_j = 10$ mm.

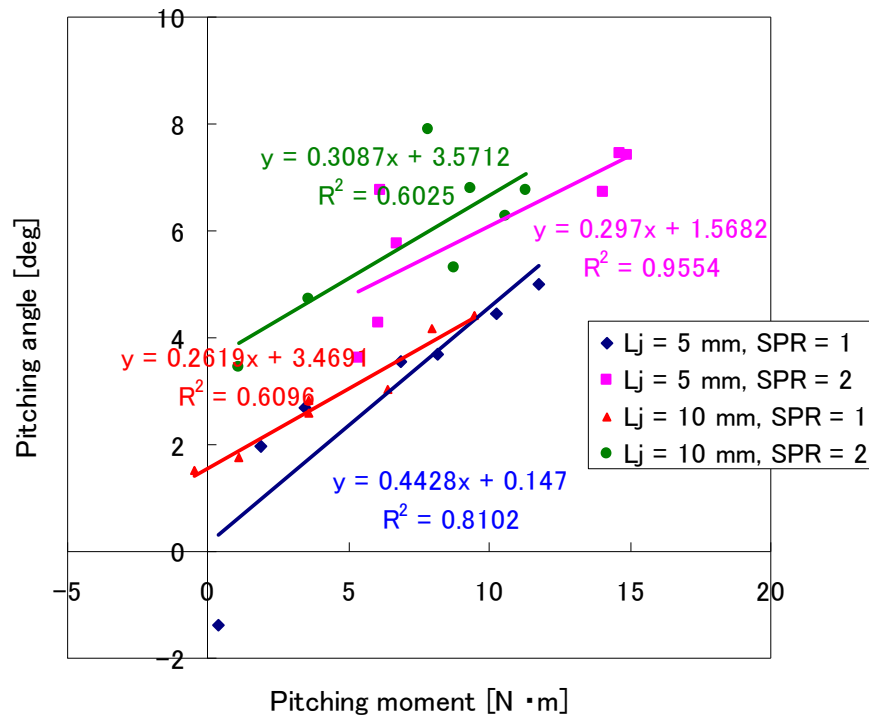


Figure 5.4 Relation between pitching moment and pitching angle.

5.2.2 Effect of SPR

Due to the secondary jet injection, there are notable shock waves at the upstream of the secondary jet slot. In order to investigate the effect of SPR quantitatively, Table 5.2 shows the thrust pitching moment with NPR = 9 at different SPR and Lj. It is observed that the moment of Lj = 10 mm is smaller than that of Lj = 5mm. The moment increases from SPR = 1 to SPR = 2 and then decreases at the SPR = 3 possibly due to shock reflection on the other wall, as shown in Fig. 4.10.

Table 5.2 Thrust pitching moment at different SPR and Lj.

Thrust pitching moment M_p [N · m]	SPR = 1	SPR = 2	SPR = 3
Lj = 5 mm	11.8	14.9	13.8
Lj = 10 mm	9.5	10.6	9.6

Table 5.3 shows the thrust pitching angle δ_p with NPR = 9 at different SPR and Lj. It is observed that deflection angle of Lj = 10 mm is smaller than that of Lj = 5 mm. The angle increases as the SPR increases. The change tendency of deflection angle is not the same as the moment for the

possible tiny reflection has not effect on the deflection angle. The density distribution and Schlieren pictures are shown in Section 4.3.2.

Table 5.3 Thrust pitching angle at different SPR and Lj.

Thrust pitching angle δ_p [deg]	SPR = 1	SPR = 2	SPR = 3
Lj = 5 mm	5.0	7.4	8.6
Lj = 10 mm	4.4	6.3	7.7

5.2.3 Effect of Lj

The Lj increases with the secondary jet slot moving to the nozzle throat, Lj being the distance between the secondary jet slot and the nozzle exit. In order to investigate the effect of Lj quantitatively, Fig. 5.5 shows the thrust pitching moment M_p at different Lj with NPR = 9. It is observed that the moment decreases as the Lj increases to 10 mm, that is to say, as the secondary jet slot moves to the nozzle throat, the effect of the secondary jet on pitching moment becomes weaker. Most of the moments are negative for the Lj from 20 mm to 80 mm for the possible reflections.

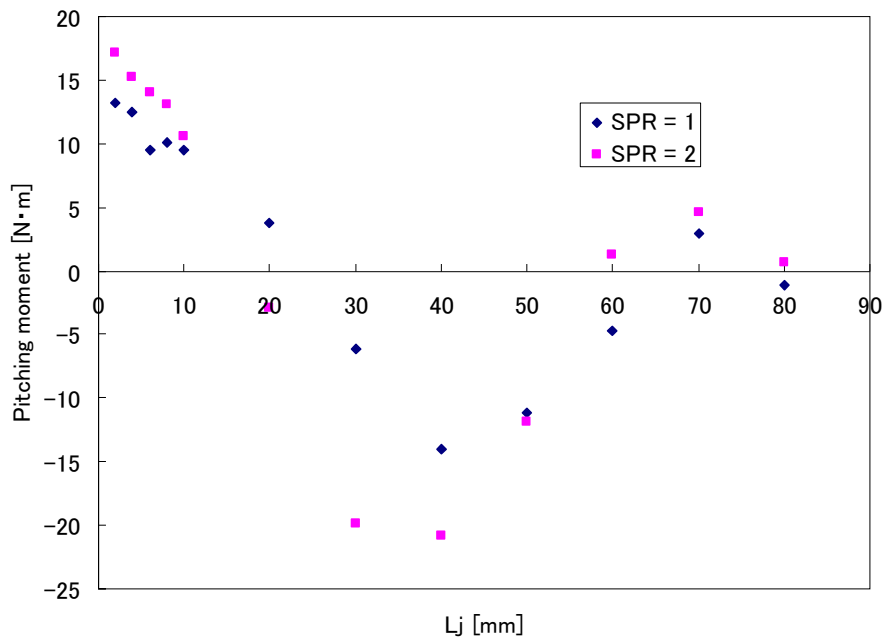


Figure 5.5 Thrust pitching moment at different Lj with NPR = 9.

Figure 5.6 shows the thrust pitching angle δ_p at different Lj with NPR = 9. It is observed the deflection angle decreases as the Lj increases to 10 mm, that is to say, as the secondary jet slot is

near the nozzle throat, the effect of the secondary jet on deflection angles becomes weak. Most of the angles are negative for the L_j from 20 mm to 80 mm due to the possible reflection. The change tendency is the same as the moment. This is also said that larger moment generates the larger deflection angle. The Mach number distributions are shown in Section 4.3.3.

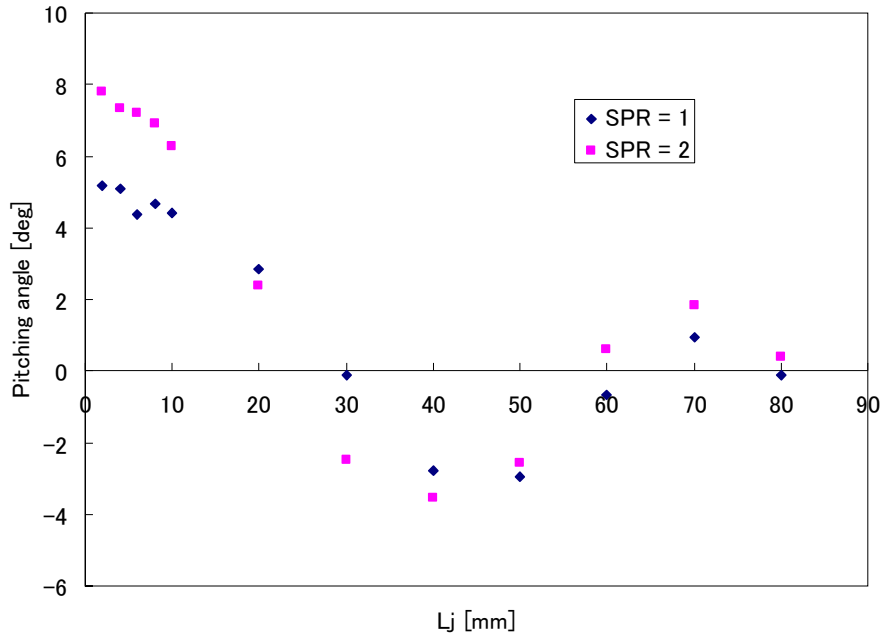


Figure 5.6 Thrust pitching angle at different L_j with NPR = 9.

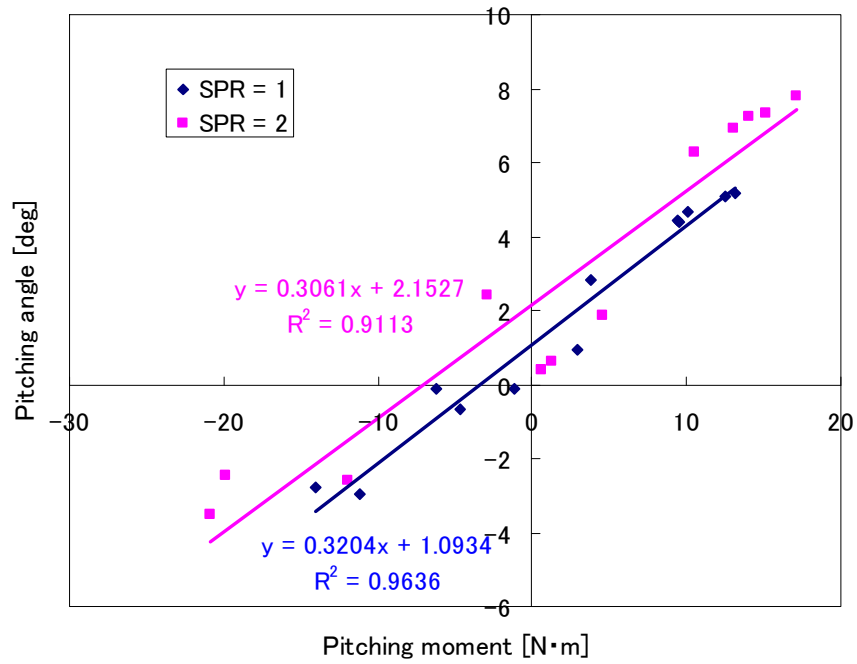


Figure 5.7 Relation between pitching moment and pitching angle.

The relation between the thrust pitching moment and thrust pitching angle is shown in Fig.5.7. For the case of $SPR = 1$, the trend line is plotted based on the blue points together with the regression equation y and coefficient of determination R^2 of the trend line. The regression equation and coefficient of determination of $SPR = 2$ is gotten by the same way. The regression equations show that the larger the moment is, the larger is the deflection angle. The coefficients of determination of two cases are high above 0.9.

5.2.4 Effect of β

The secondary angular injection angle β is defined as positive when it is measured counterclockwise from the vertical axis, and $\beta = 4.7^\circ$ when the jet is normal to the nozzle wall. Figure 5.8 shows the thrust pitching moment M_p at different β with $NPR = 9$. When the β is positive, the moment decreases and the moment for $SPR = 2$ is larger than $SPR = 1$ except $\beta = 70^\circ$. Whereas when the β is negative, the change tendency of the moment with $SPR = 1$ is different from that with $SPR = 2$. The biggest moment of $SPR = 1$ occurs with $\beta = -45^\circ$.

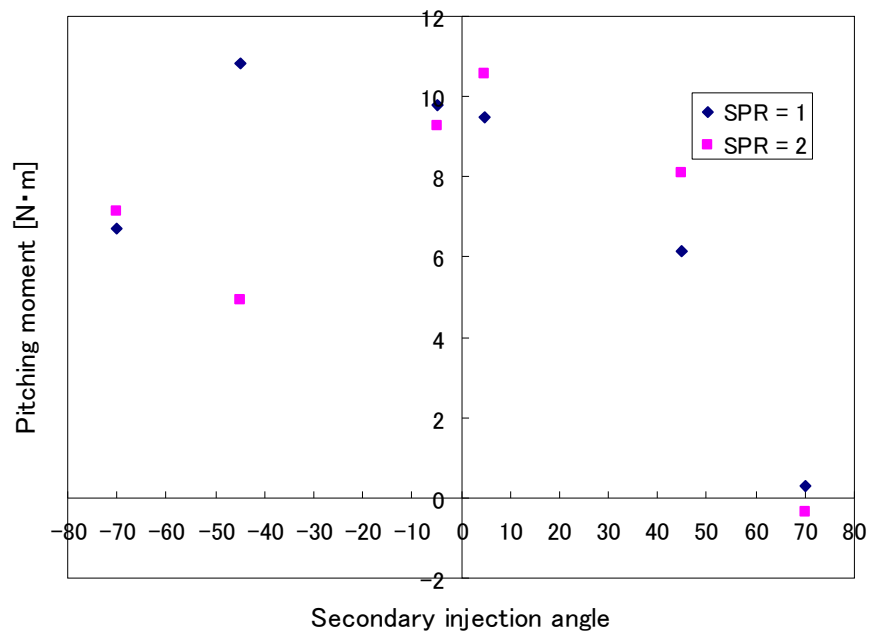


Figure 5.8 Thrust pitching moment at different β with $NPR = 9$.

Figure 5.9 shows the pitching angle δ_p at different β with $NPR = 9$. It is observed the angle change tendency is the same as that of the pitching moment. When β is positive, the largest angle with $SPR = 1$ happens with the largest moment. Whereas for $SPR = 2$, the largest pitching angle equals 6.4° happens with β near 0° .

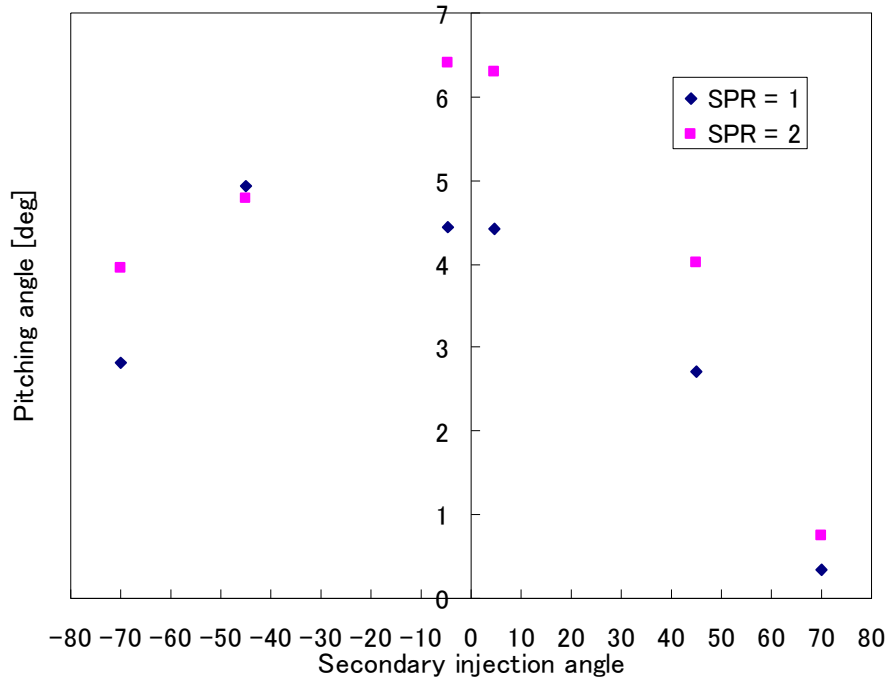


Figure 5.9 Thrust pitch angle at different β with NPR = 9.

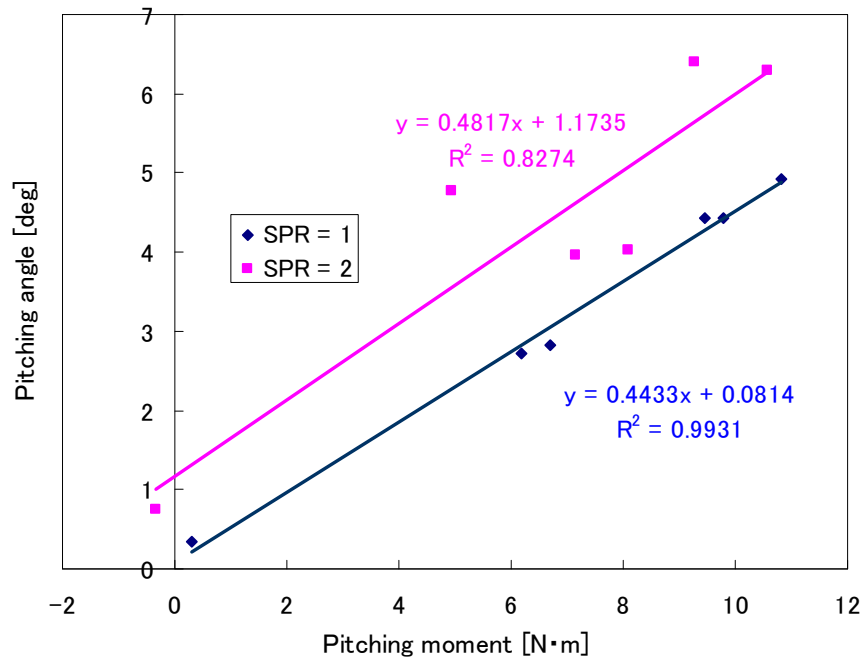


Figure 5.10 Relation between pitching moment and pitching angle.

The relation between the thrust pitching moment and thrust pitching angle is shown in Fig.5.10. The

nearer of the coefficients of determination R^2 to 1, the fitter is the regression equation. The regression equations show that the larger of the moment, the larger is the deflection angle. The coefficients of determination of $SPR = 1$ are higher than that of $SPR = 2$.

5.3 Summary

In the preliminary setup, the slot for the secondary jet injection is so large that the flow deflection by an oblique shock is concealed by complex wave interactions. So it is difficult to evaluate the FTV performance quantitatively.

The improved experimental model with a relative smaller secondary jet slot is constructed to study the details of the FTV mechanism and its performance. Numerical and experimental studies of FTV were carried out with the improved FTV nozzle.

The performance of FTV is evaluated by the thrust pitching moment and the thrust pitching angle, and the thrust pitching moment of the improved nozzle is positive as expected induced by an oblique shock wave.

The bigger SPR causes the decreased moment due to the possible tiny reflection on the opposite nozzle wall, but it has no effect on the deflection angle.

As the secondary jet slot moves to the nozzle throat, the effect of the secondary jet on the pitching moment and the deflection angle becomes weak.

For different secondary angular injection β , the positive and negative cases should be separated to discuss. For positive β , the moment and deflection angle decreases as the β increases, and the moment of higher SPR is larger. For negative β , the change tendency of the moment and the deflection angle is different with different SPR.

The relation between thrust pitching moment and thrust pitching angle shows that the larger of the moment, the larger is the deflection angle.

References

- [1] Mark S. Mason, William J. Crowther, Fluidic Thrust Vectoring of Low Observable Aircraft, CEAS Aerospace Aerodynamic Research Conference, 2002.
- [2] K. A. Waithe and K. A. Deere, Experimental and Computational Investigation of Multiple Injection Ports in a Convergent-divergent Nozzle for Fluidic Thrust Vectoring, the 21st AIAA Applied Aerodynamics Conference, AIAA-2003-3802.
- [3] David J. Wing, Victor J. Giuliano, Fluidic Thrust Vectoring of an Axisymmetric Exhaust Nozzle at Static Conditions, ASME Fluids Engineering Division Summer Meeting, 1997.
- [4] J. D. Flamm, K. A. Deere, Design Enhancements of the Two-Dimensional, Dual Throat Fluidic Thrust Vectoring Nozzle Concept, AIAA 2006-3701, 3rd AIAA Flow Control Conference, San Francisco, California, 2006.
- [5] K. A. Deere, Computational Investigation of the Aerodynamic Effects on Fluidic Thrust Vectoring, 36th AIAA/ASME/SAE/ASEE Joint Propulsion Conference and Exhibit, 2000.

Chapter 6 Conclusions

6.1 Summary

The objective of this paper is to investigate the FTV effects of a secondary jet on the primary flow in a converging-diverging nozzle. The evaluation of the FTV performance with FTV parameters has also been investigated. Numerical and experimental studies of FTV were carried out with a preliminary nozzle model and an improved nozzle model.

In the preliminary studies, it has been found difficult to evaluate the FTV performance quantitatively on the basis of the appearance of downstream flow patterns. The slot for the secondary jet injection is so large that the entire flow field downstream of the throat is affected by the jet even with a relatively low secondary jet pressure ratio SPR. The experiments are performed with a NPR of 4–10, a SPR of 1 or 2, and two different secondary jet locations. Numerical simulations of the nozzle flow are carried out by solving the Navier-Stokes equation, and the input parameters are set to match the experimental conditions. Computations are performed with and without the secondary jet injection for different combinations of NPR, SPR, and jet location.

In order to study the details of the FTV mechanism and its performance, the improved experimental model with a smaller secondary jet slot is constructed. The effects of FTV parameters, such as NPR, SPR, and jet location L_j and secondary angular injection β are discussed. The performance of FTV is evaluated by thrust pitching moment and thrust pitching angle.

The results of this study are summarized as follows:

1. The two FTV mechanisms with opposite signs of thrust pitching moments are investigated. For the expected FTV mechanism, if the secondary jet slot is on the nozzle upper wall, the injected flow forms an oblique wave which makes the primary flow turn downwards from the longitudinal axis when the primary flow interacts with the oblique wave. As a reaction force, the nozzle will turn upwards. So in this study, the counterclockwise is defined as positive which is same the direction with the expected FTV mechanism. The preliminary mechanism owing to the pressure difference in the vicinity of the nozzle exit has the negative moment, whereas, the improved nozzle are positive moment as expected by the oblique shock waves.

2. The thrust pitching moment of the preliminary FTV mechanism is found to be opposite to the expected FTV mechanism, which has no descriptions in the previous FTV researches. It is found there is an opposite nozzle condition which is different from the traditional FTV mechanism, and the results will help rich the research data of FTV studies.

3. The thrust pitching moment and the thrust pitching angle are used to evaluate FTV performance. There is a method using force-moment balance and a common procedure for utilizing the ratio of the

radial to the axial momentums of exhaust gas. It is found that the pitching angle becomes smaller as the measuring point moves far away from the nozzle exit; that is to say, the thrust pitching angle is depending on the measurement position. In this study, the pitching angle is evaluated at the nozzle exit. In this study, we put forward the new evaluation method using thrust pitching moment. The thrust pitching moment of the nozzle is calculated by integrating the product of the pressure on the nozzle walls and the length from a specific pivot point to the pressure working point. The pivot point can be chosen arbitrarily without affecting the characteristics of the thrust pitching moment.

4. The internal flow field in the nozzle with the secondary injection effects is discussed. The nozzle internal parameter distributions are presented, such as the Mach number, density, velocity. The numerical simulations results and the experimental results provide help to analyze the nozzle internal flow field. The different NPR causes the different flow pattern downstream the nozzle exit with oblique shock waves or oblique expansion waves. With the injection of secondary jet, notable shock waves and flow separation are observed at the upstream of the secondary jet slot. As the L_j becomes larger, the oblique shock and the range of the separation decrease. As the location of the secondary jet injection is moved to the throat, the induced oblique shock wave reflects at the opposite nozzle wall even with small SPR. The range of separation domain caused by the negative β is larger than that caused by positive β .

5. The effects of FTV parameters on FTV performance are analyzed. The parameters, such as the NPR, SPR, L_j and β have direct effects on the performance. The bigger SPR causes the decreased moment due to the possible tiny reflection on the opposite nozzle wall, but it has no effect on the deflection angle. As the secondary jet slot moves to the nozzle throat, the effect of the secondary jet on the pitching moment and the deflection angle becomes weak. For different secondary angular injection β , the positive and negative cases should be separated to discuss. For positive β , the moment and deflection angle decreases as the β increases, and the moment of higher SPR is larger. For negative β , the change tendency of the moment and the deflection angle is different with different SPR.

6. The relation between the thrust pitching moment and the thrust pitching angle are discussed. The regression equation y and coefficient of determination R^2 of the trend line are gotten with the linear approximation. The regression equations show that the larger of the moment, the larger is the deflection angle. The positive inter-relation is between them. Therefore, FTV performance can be evaluated by the thrust pitching moment directly.

7. The guidance for optimizing nozzle configuration is provided. Getting large thrust pitching angle is one of purposes to the nozzle design. In this study, two type simple nozzles are designed. For the nozzle used in the preliminary experiment, the thrust pitching angle is near to zero for the stronger effect of the pressure balance than the oblique shock wave. So the nozzle is improved in the next experiment, and the angle reaches 8.6° at the condition of $L_j = 5$ mm, $NPR = 9$ and $SPR = 3$.

6.2 Future Work

Though current research presents the nozzle flow field structure and evaluation methods which help understand the FTV performance, for understand the FTV nozzle well, the following aspects should be further investigated.

1. The applicable mathematical model should be investigated, such as the relation among SPR and L_j , β and thrust pitching angle.

2. The calculation code needs to update to 3D, so it can provide more accurate data to help understand the nozzle study well.

3. In order to get more reference data, such as total pressure in the nozzle and moment at the nozzle wall, the experiment equipment need to be improved.

4. The shock impingement is always as the disadvantage of FTV, but it can be changed to advantage by generating the opposing force. Of course, the opposite force needs rigorous applicable models.

5. The performance of FTV nozzle is evaluated for the steady state. In the practical situation, instabilities may also be present due to various factors, so the FTV nozzle in the unsteady state also needs to be considered.

The conclusions and future work are discussed above. The results of the paper are hoped to provide guidance to the FTV studies.

Acknowledgments

I would like to extend my gratitude to my supervisor, Professor Saito Tsutomu for his patient guidance. Professor's rigorous research attitude and critical thinking express me deeply.

I must acknowledge Lector Hirota Mitsutomo for his support to experiment setup and his inspiration advisement.

The very special thanks go out to Professor Takagi Shohei and Professor Higashino Kazuyuki as the secondary supervisors for the meticulous thesis review.

I owe a debt of gratitude to Professor Sugiyama Hiromu and Professor Xu Li for recommendation and encouragement.

I try to give credit to Fujimoto Tetsuya and Hatanaka Kazuaki for providing the basic computational resources to conduct the numerical work.

I appreciate the group members, Aoyama Shinji, Xue Wei, Ito Seira, Yamada Kouhei, Kato Shunsuke for their cooperation and constructive discussion.

I extend my special gratitude to Ms. Shiozaki Taiko for her always kind concern and help.

I give my thank to associate Professor Kadosawa Kenya, Associate Professor Yamaji naoko, and Ms. Takaku Yuko for their teaching Japanese.

I would like to thank Muroran Institute University and Dalian Jiaotong University for giving me the opportunity to study.

Finally, I am everlastingly gratitude to my friends, my family for their understanding, endless patience and encouragement.

Appendices

A.1 Supersonic Flow and Shock Theory

A.1.1 One-Dimensional Gasdynamics

One dimensional method simplifies the equations of fluid flow and is adequate for the solution of many engineering problems, such as flow in nozzles or ducts [1].

A.1.1.1 The Basic Equations

The fundamental equations of fluid dynamics include the state, continuity, momentum, and energy equations are shown as follows [2]. The sketch of a flow through a tube segment is shown in Fig. A.1.

$$p = \rho RT, \quad (\text{A-1})$$

$$\rho_1 u_1 A_1 = \rho_2 u_2 A_2, \quad (\text{A-2})$$

$$\rho_2 u_2^2 - \rho_1 u_1^2 = p_1 - p_2, \quad (\text{A-3})$$

$$\frac{u_1^2}{2} + h_1 = \frac{u_1^2}{2} + \frac{\gamma}{\gamma-1} \frac{p_1}{\rho_1} = \frac{u_2^2}{2} + \frac{\gamma}{\gamma-1} \frac{p_2}{\rho_2} = \frac{u_2^2}{2} + h_2, \quad (\text{A-4})$$

where p is the pressure, ρ is the density, R is the ideal gas constant, T is the temperature, u is the flow velocity, h is the enthalpy, γ is the heat capacity ratio, and A is the section area.

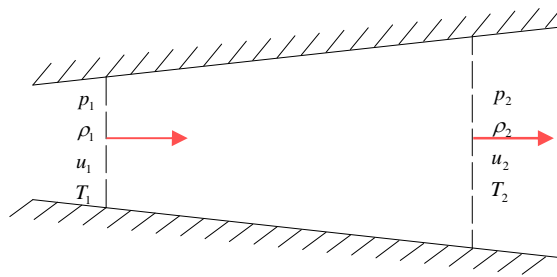


Figure A.1 The flow through a tube segment.

A.1.1.2 Isentropic Conditions

A perfect isentropic gas is in adiabatic and equilibrium state. The relation can be written

$$\frac{p_2}{p_1} = \left(\frac{\rho_2}{\rho_1} \right)^\gamma = \left(\frac{T_2}{T_1} \right)^{\gamma/(\gamma-1)}. \quad (\text{A-5})$$

For a perfect gas this condition may also be written

$$a = \sqrt{\gamma RT} = \sqrt{\gamma \frac{p}{\rho}}. \quad (\text{A-6})$$

A.1.1.3 Stagnation Conditions

The constant in Eq. (A-4) can be conveniently evaluated at $u = 0$ and in equilibrium state

$$h + \frac{1}{2}u^2 = h_0. \quad (\text{A-7})$$

The h_0 is called the stagnation enthalpy and the state at point with $u = 0$ is called stagnation point.

The relations based on M are

$$\frac{p_0}{p} = \left(1 + \frac{\gamma - 1}{2} M^2\right)^{\gamma/(\gamma - 1)}, \quad (\text{A-8})$$

$$\frac{\rho_0}{\rho} = \left(1 + \frac{\gamma - 1}{2} M^2\right)^{1/(\gamma - 1)}, \quad (\text{A-9})$$

$$\frac{T_0}{T} = 1 + \frac{\gamma - 1}{2} M^2. \quad (\text{A-10})$$

The values of a_0 , p_0 , ρ_0 , and T_0 are constant throughout the flow, the subscript 0 is means the parameters are the stagnation values.

A.1.1.4 Critical Conditions

The condition at $M = 1$ is called sonic, and is denoted by the superscript $*$. Then the flow speed and sound speed are u^* and a^* , respectively. Since $M = 1$, u^* equal to a^* . The energy equation (A-4) then can be written

$$\frac{a_0^2}{\gamma - 1} = \frac{u^2}{2} + \frac{a^2}{\gamma - 1} = \frac{u^{*2}}{2} + \frac{a^{*2}}{\gamma - 1} = \frac{1}{2} \frac{\gamma + 1}{\gamma - 1} a^{*2}. \quad (\text{A-11})$$

For the perfect gas

$$\frac{a^*}{a_0} = 0.913, \quad (\text{A-12})$$

$$\frac{T^*}{T_0} = \frac{2}{\gamma + 1} = 0.833, \quad (\text{A-13})$$

$$\frac{p^*}{p_0} = \left(\frac{2}{\gamma + 1}\right)^{\gamma/(\gamma - 1)} = 0.528, \quad (\text{A-14})$$

$$\frac{\rho^*}{\rho_0} = \left(\frac{2}{\gamma + 1}\right)^{1/(\gamma - 1)} = 0.634. \quad (\text{A-15})$$

The relation is also mentioned as

$$M^* = u/a^*, \quad (\text{A-16})$$

the relation between M^* and M is

$$\left(\frac{u}{a^*}\right)^2 = M^{*2} = \frac{\gamma+1}{2/M^2 + \gamma - 1}, \quad (\text{A-17})$$

$$M^2 = \frac{2}{(\gamma+1)/M^{*2} - (\gamma-1)}. \quad (\text{A-18})$$

A.1.2 Flow in Converging-Diverging Nozzle

The converging-diverging nozzle, also called Laval nozzle, is the basic aerodynamic element to obtain prescribed flows. The Laval nozzle has a converging inlet section, a minimum area (throat), and a diverging exit section. The nozzle is supplied with fluid at high pressure p_0 at the inlet and exhausts into a lower pressure p_{back} at the outlet.

A.1.2.1 Flow in Nozzle of Vary Area

To investigate the variation of flow parameters along the nozzle, there is an approximation that the flow is one dimensional; that is to say, conditions across each section are uniform. The sketch of flow in nozzle of vary area is shown in Fig. A.2.

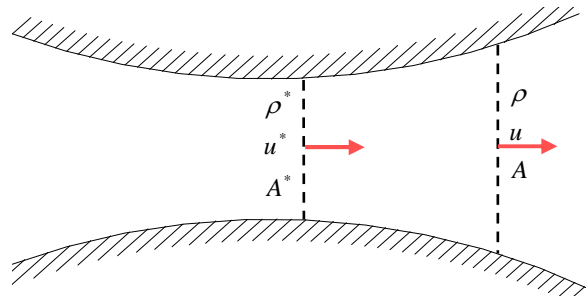


Figure A.2 Flow in nozzle of vary area.

It is convenient to use sonic conditions as reference in continuity equation

$$\rho u A = \rho^* u^* A^*. \quad (\text{A-19})$$

The A^* denotes the throat area, and the relation between nozzle area and Mach number for isentropic flow is written in the form

$$\frac{A}{A^*} = \frac{1}{M} \left[\frac{(\gamma - 1)M^2 + 2}{\gamma + 1} \right]^{\frac{\gamma + 1}{2(\gamma - 1)}} \quad (\text{A-20})$$

The expression for the rate of mass flow \dot{m} of a perfect gas through a nozzle is

$$\dot{m} = \rho Au = \frac{p_0 A}{\sqrt{RT_0}} \sqrt{\frac{2\gamma}{\gamma - 1} \left[\left(\frac{p}{p_0} \right)^{2/\gamma} - \left(\frac{p}{p_0} \right)^{(\gamma + 1)/\gamma} \right]} \quad (\text{A-21})$$

If the flow is subsonic throughout, the maximum velocity occurs at the throat by decreasing the downstream pressure p_{back} . But, once the speed at the throat becomes sonic, it can increase no further, for sonic conditions can exist only at the throat. A further decrease of p_{back} can not cause any more flow to be induced through the nozzle. Under these conditions, the nozzle is said to be choked [3-4].

$$m^* = \frac{p_0 A^*}{\sqrt{RT_0}} \left[\gamma \left(\frac{2}{\gamma + 1} \right)^{\frac{\gamma + 1}{\gamma - 1}} \right]^{1/2} \quad (\text{A-22})$$

A.1.2.2 Nozzle Flow

To understand the flow through the nozzle, it is divided to several cases. The figure shows the form of the theoretical pressure distributions and the wave configurations for several exit pressures p_{back} [5-6]. The nozzle flow can be divided into four regions, as shown in Fig. A.3.

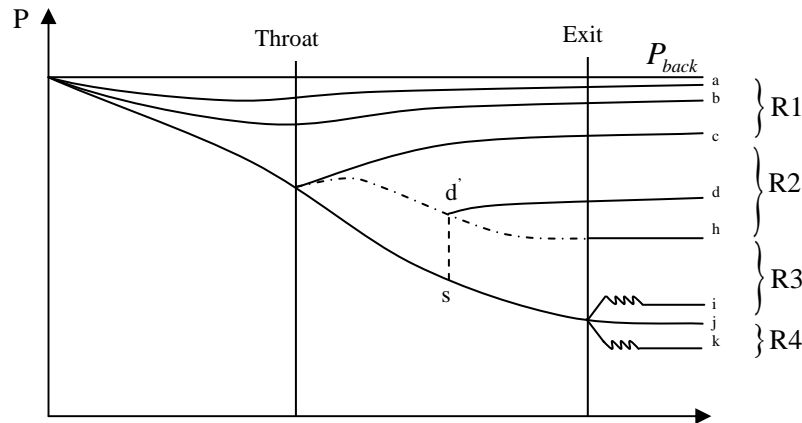


Figure A.3 Pressure distribution in the nozzle with different back pressure.

In region 1 (from a to c), the flow is entirely subsonic and the back pressure controls the flow throughout the nozzle. The limiting flow in this region occurs when the throat Mach number equal 1.

In region 2 (under c to h), supersonic flow first occurs in the divergent part of the nozzle. Because the back pressure is higher than the nozzle exit pressure p_{exit} , a normal shock is established in the nozzle, and the supersonic flow changes abruptly to subsonic flow. As p_{back} is progressively lowered, the shock wave moves downstream progressively until at the nozzle exit. Throughout the region, the p_{exit} continues to adjust to equal to p_{back} , whereas the flow rate remains constant, independent of the p_{back} , because the flow is choked at the throat.

In region 3 (under h to j), supersonic flow is throughout the entire nozzle with $p_{exit} < p_{back}$. The flow is over-expanded with oblique shock waves downstream of the nozzle exit. A compression process is required to balance the pressures and the flow rate continues to be independent of the back pressure.

In region 4 (under j), supersonic flow once more prevails throughout the entire nozzle with $p_{exit} > p_{back}$. The flow is under-expanded with oblique expansion waves outside the nozzle too. The expansion process is required to balance the pressures and the flow rate continues to be independent of p_{back} since the nozzle is choked.

There are three critical p_{back} cases, that is, the first critical p_c , the nozzle is choked but without shock; the second critical p_h , the normal shock at the nozzle exit; the third critical p_j , the nozzle isentropic design without shock

$$\frac{A_e}{A^*} = \sqrt{\left(\frac{\gamma-1}{2}\right)\left(\frac{2}{\gamma+1}\right)^{\frac{\gamma+1}{\gamma-1}} \left[\left(\frac{p_c}{p_0}\right)^{\frac{2}{\gamma}} - \left(\frac{p_c}{p_0}\right)^{\frac{\gamma+1}{\gamma}} \right]}, \quad (\text{A-23})$$

$$\frac{p_h}{p_0} = \frac{2\gamma M_1^2 - (\gamma - 1)}{\gamma + 1} \left(1 + \frac{\gamma - 1}{2} M_1^2\right)^{-\frac{\gamma}{\gamma-1}}, \quad (\text{A-24})$$

$$\frac{p_0}{p_j} = \left(1 + \frac{\gamma - 1}{2} M^2\right)^{\gamma/(\gamma-1)}. \quad (\text{A-25})$$

where M_1 is the mach number upstream the shock wave at the exit.

A.2 Schlieren Methods

The optical methods, which depend on the variation of density throughout the flow field are best developed and most widely used techniques for the investigation of compressible flows. The conventional methods are schlieren, shadowgraph and interferometer methods. These methods, which depend on the light speed varies with the density of the medium through which it is passing can observe the flow phenomena without disturbance or any superfluous object in the flow [7-8].

Of the three optical methods, the interferometer gives a direct indication of density, unlike the Schlieren or shadowgraph. It is the most precise, delicate, yet also most costly, and difficult to set up. The shadowgraph is simpler, cheaper and easier to operate than Schlieren but not precise. The shadowgraph indicating the second derivative of density is more suitable for observe flows with large, sudden changes in density. For flows with slowly varying density, the Schlieren system should be used. In this study, the schlieren method is employed, so the optical system is introduced in detail as follows. The basic schlieren system is shown in Fig. A.4.

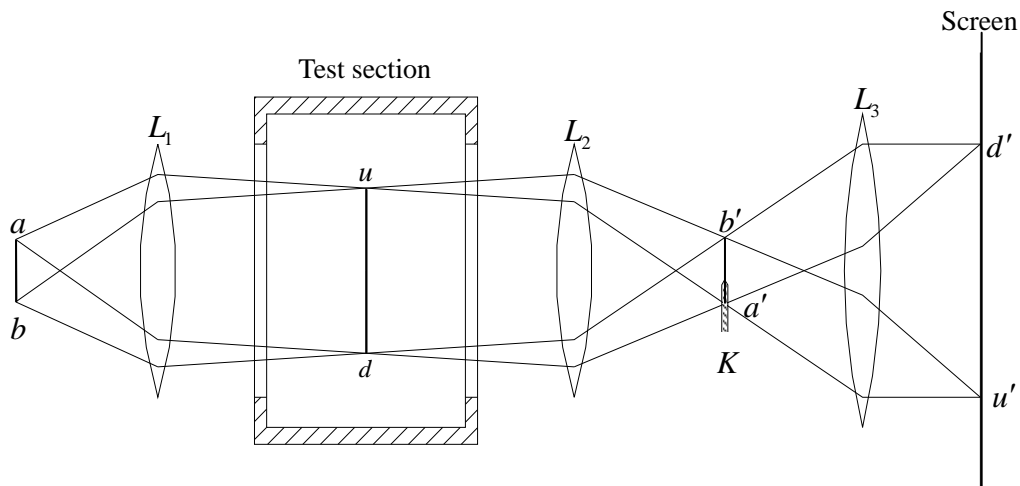


Figure A.4 Schlieren system.

Light from a source ab is collimated by lens L_1 , providing a parallel light beam through the test section. The two extreme light rays from a and b passing parallel through the test section are shown in figure. After passing through the test section, the light rays are focused by a second lens L_2 . If a screen is placed in the focal plane of L_2 , an inverted image of the source $a'b'$ is obtained. Otherwise, the light is then focused on the screen of photographic plate by an objective lens L_3 , providing an inverted image of the test section.

Now, intercept part of light by placing a knife edge K at $a'b'$. In this case, the image of the test section on the screen will be darker than before, and the image point would appear darker or brighter

than the rest of the field, depending on how the light is intercepted.

The contrast is defined by

$$c = \frac{\Delta h}{h_1} = \frac{f_2 \varepsilon}{h_1} = \frac{f_2 L \beta}{h_1 \rho_s} \left(\frac{d\rho}{dy} \right)_1, \quad (\text{B-1})$$

where Δh is the displacement length of the source image, h_1 is the uncovered length of the source image, f_2 is the focal length of the second lens, ε is the angular displacement, L is the width of test section, β is refractivity of the fluid, ρ_s is the reference density taken at standard conditions,

and $\left(\frac{d\rho}{dy} \right)_1$ is the density gradient.

Thus, it is possible to use a schlieren system to visualize a shock wave by observing the light or dark areas on the screen.

A.3 Instrument

1 Vacuum tank (Taihei Kogyo co., Ltd.)

Diameter: 2.5 m

Length: 6.0 m

Volume: 33 m³

Maximum allowable stress: 5kgf/cm²

2 Valve

Quick closing valve (ULVAC)

Format: VAH-U100

3 Nano-pulse light (Sugawara Laboratories)

Format: NPL argon discharge tube-2

Flash duration : 75ns

4 Digital SLR camera (NIKON)

Format : Digital reflex camera type interchangeable lens SLR D40X

Effective pixel : 10.2 Mpixel

5 Pressure sensor (KYOWA)

Format: PG-2KU

Rated capacity: -98.07-200 [KPa] (gauge pressure)

Natural frequency: approximately 2 [KHz]

Rated output: 2 [mV/V] ($4000 \times 10^{-6} \epsilon \pm 1[\%]$)

Input Resistance: 350Ω±1%

Output Resistance: 350Ω±1%

6 Sensor interface (KYOWA)

Format: PCD-300A

Number of Channels: 4

Gauge resistance: 120[Ω]~1[kΩ]

Gauge factor: 2.00

Conversion unit AD: 12 resolution [bit]

Range: 200, 500, 1000, 2000, 5000, $10000 \times 10^{-6} \epsilon \pm 0.5[\%]$, 7 stages and OFF

Sampling frequency: 1, 2, 5, 10, 20, 50, 100, 200, 500[Hz], 1, 2, 5[kHz]

References

- [1] Alan J. Chapman and William F. Walker, *Introductory Gas Dynamics*, Holt, Rinehart and Winston, Inc., 1971.
- [2] Robert P. Benedict, *Fundamentals of Gas Dynamics*, John Wiley & sons, Inc., 1983.
- [3] Jerzy A. Owczarek, *Fundamentals of Gas Dynamics*, International Textbook Company, 1968.
- [4] 生井武文, 松尾一泰, *圧縮性流体の力学*, 東京 : 理工学社, 1977.
- [5] 鈴木宏二郎, *圧縮性流れの理論*, 東京: 丸善, 2008.
- [6] 杉山弘, 遠藤剛, *流体力学*, 東京: 森北出版, 1995.
- [7] James E. A. John, *Gas Dynamics*, Allyn and Bacon, Inc., 1978.
- [8] H.W. Liepmann and A. Roshko, *Elements of Gasdynamics*, John Wiley & Sons, Inc., 1967.